ABSTRACT

PROPERTIES OF SHELL-MODEL WAVEFUNCTIONS AT HIGH EXCITATION ENERGIES

By

Njema Jioni Frazier

Within the framework of the nuclear shell model with a realistic residual hamiltonian one can obtain the exact solution of the many-body problem. This makes it possible to study the interrelation between regular and chaotic features of dynamics in a generic many-body system with strong interaction. As an important application, we analyse the fragmentation of simple configurations as a function of excitation energy and interaction strength and examine the transition strengths induced by simple operators as a function of excitation energy. The analysis is performed for two systems; that of 12 valence particles in the *sd*-shell, or ^{28}Si, and that of 8 valence particles in the *sd*-shell, or ^{24}Mg. For the system of 12 valence particles in the *sd*-shell, we examine the fragmentation of shell-model basis states. For the system of 8 valence nucleons in the *sd*-shell, we examine the fragmentation associated with single-nucleon transfer and Gamow-Teller transitions.

For the fragmentation of basis states, we use our statistics to establish the generic shape of the strength function distribution in the region of strong mixing. For the realistic interaction, the strength function distribution is close to Gaussian in the central part of the energy spectra. The width of the distribution is larger than predicted by Fermi's golden rule [4].

We then take this one step further and examine the strength distributions associ-

ated with the one-nucleon transfer operator, $a^\dagger_\lambda$, and the Gamow-Teller (GT) operator, $\sum_{\lambda\lambda'}(\sigma_\mu\tau_\pm)_{\lambda\lambda'}a^\dagger_\lambda a_{\lambda'}$. The spectroscopic factor, which is proportional to the square of the matrix element for the $a^\dagger_\lambda$ operator, is the simplest quantity used in predicting experimental observables. In our discussion of Gamow-Teller transitions, we examine both the GT strength function distribution and the values of total strength $B(GT)$.

For all the cases we examine, we take advantage of the reliability of our model for low-lying levels and our statistics to explore the behavior of total strengths and strength distributions for high-lying states.

To God, my family, my friends, and especially to my parents, Philip and Aufait Frazier, who taught me to accept nothing less than the best.

ACKNOWLEDGMENTS

I would like to thank Alex Brown and Vladimir Zelevinsky for their friendship and support over the past three years. I always felt that they had faith in my abilities and my best interests at heart. I could not have asked for better advisors. I want to be them when I grow up.

I also need to say a special thank-you to Dan Stump. Without Dan I would not have stayed here at Michigan State. I'd have gotten my degree, but I wouldn't have gotten it here at MSU. I doubt that he knows how important it was to me that someone actually **saw** me. Thank you, Dan.

In that spirit, I have to thank Stephanie Holland and Shari Conroy who always had welcoming smiles **and** answers to all of my questions.

Next, I have to thank my family. If you know me, then you know that I am a family person. I cannot imagine being where I am today without them and I am blessed to have had their unconditional love and support throughout my academic career and my life. So, thank you to the Fraziers, the Williamses, the Adamses, the Keiths, the Wilsons, the Harps, the Bryans, the Woods, the Byrds, and the Caggianos.

Now, I have to get specific and thank some people who helped me keep my sanity.

- To, Jac Caggiano, who kept picking me up and dusting me off, even when I wanted to stay down.

- To my extended family: Collette, Jamara, Althea, Tracie, Debbie, Joe, Jim, Jameel, Rob, Keith, Troy, and Curt - I love y'all.

- To, Sally Gaff, who got all of my jokes and still agreed to be my roommate.

- To, Jon Kruse and Chris Powell, who gave me a reason to take a break Friday's at 11:30 (oh, who am I trying to kid, 11:10!).

- To Mathias, who taught me that there is one side, and one side only, to every story. Thanks for coming for me when I was stranded in Dundee, even if you did drive the 'deathtrap'.

- To Fauerbach, whose ready smile and optimism made the time pass that much faster. Thanks for studying with me the 2nd time around.

- To Konrad, whose silent strength helped me through the worst of times.

- To Scott, whose sense of tact and decorum should be a lesson to us all, and finally

- to all the thoughtful souls who knew that to shun a person, is to make that person stronger. Thank you, truly, I mean that.

Contents

List of Tables

List of Figures

Chapter 1

Introduction

1.1 Overview

To gain insight into the dynamics of complex nuclear systems we have two primary tools: (1) experimental data and (2) the theoretical solution of the many-body problem within the framework of the nuclear shell model. With these tools we can study the characteristics of a quantum many-body system by examining nuclear wavefunctions and nuclear matrix elements.

Because of the nuclear shell model's ability to predict various experimental observables and its broad range of applicability to different nuclear transitions from low-lying states, we are encouraged to extend its use into the region of high-lying states, where we have no experimental data from which to draw. Going beyond the lowest energy region we rely on the shell-model predictions in the analysis of highly-excited states whose individual properties are inaccessible by current experimental tools of nuclear spectroscopy. Ideally, we would like to reach some conclusions about statistical features of these more complicated high-lying states.

The properties of shell-model wavefunctions at high excitation energy are interesting physically for a number of reasons. First, they aid in our understanding of nuclear reactions, for which we need to know the statistical properties of highly-excited states.

Secondly, transitions from excited states are important for our understanding of astrophysical processes. And while astrophysical reactions of this nature are not addressed directly in this work, the results of our studies should provide guidance for future investigation. And lastly, the systems we have chosen are two of the best examples of quantum many-body systems where we have a good, although approximate, solution of the many-body problem. From these systems we try to study general properties of quantum chaos; insomuch as the same approach we apply here may be used in atomic and solid state physics.

The main objectives of this work are (1) to study the fragmentation of simple shell-model configurations, or the splitting of the strength of simple shell-model states over more complicated excited states, as a function of excitation energy and interaction strength, (2) to determine the effect that basis-state mixing has on the distribution of the strengths associated with simple one-body operators, $a^\dagger_\lambda$ and $[(\sigma_\mu\tau_\pm)_{\lambda\lambda'}a^\dagger_\lambda a_{\lambda'}]$, and (3) to analyse the behavior of the total Gamow-Teller strength as a function of excitation energy. This work is intended to give theoretical information about excited states of the nucleus and transitions from those excited states.

The rest of chapter 1 will touch upon the organization of the paper, the motivation for this work, and a brief introduction of our main topics: the spreading of basis states, single-nucleon transfer, and Gamow-Teller transitions.

The reliability of the shell model with realistic residual interactions is widely accepted [1, 2]. Calculations of nuclear energy spectra and various other observables show good agreement with the growing body of data. In chapter 2 we will review the basis of shell-model theory, explain how the calculations are carried out, and demonstrate the surety of the technique for various nuclei in the $0d-1s$ shell-model space.

As excitation energy and level density increase, incoherent mixing converts independent particle configurations into complex eigenstate configurations. The basis states associated with the independent particle configurations then become spread over many eigenstates. We begin chapter 3 with a review of the basic definitions and the standard model for the spreading width of the strength function (sect. 3.1). We will define the limits of "strong" versus "weak" coupling and use these limits to analyze the results for the strength function shown in section 3.2. At the realistic interaction strength, the generic shape of the strength function is close to a Gaussian in the central part of the energy distribution. Up to high accuracy, the wings of the distribution display exponential behavior. The spreading width considerably exceeds the Fermi golden rule value. In our calculations, we approach the weak coupling limit by artificially suppressing the interaction. The strength function evolves as the interaction strength changes. In the limit of "weak" coupling, we return to the domain of validity of the standard model for spreading widths where the shape of the strength function is usually assumed to be of Breit-Wigner type. The spreading width dependence on the interaction strength changes from linear to quadratic as one proceeds from strong to weak coupling.

Nuclear spectroscopy provides some of the most reliable and abundant data available. The spectroscopic factors in single-nucleon transfer provide us with important information on the fragmentation of single-particle configurations. However, the abundance of data is concentrated in the low-energy region. Chapter 4 deals with the effect that mixing has on the width of the one-nucleon transfer distribution $|\langle f|a^\dagger|i\rangle|^2$. The creation operator $a^\dagger$ creates a particle in the initial state, and the resultant wavefunction is then overlapped with the final state eigenfunction. By examining the width of the distribution we gain insight into excited-state single-nucleon transfer. We relate the widths of single-particle transfer distributions to the widths

for basis state strength functions and Gamow-Teller strength functions. The width of the distribution for single-nucleon transfer is considerably smaller than that for the fragmentation of basis states.

Chapter 5 addresses the characteristics of the Gamow-Teller strength function distribution and the total Gamow-Teller strength. The matrix elements for the GT operator for low-lying states are measured against the experimental results for beta decay. This allows us to test the accuracy of and provide us with important information about nuclear structure. The Gamow-Teller (GT) operator $\sum_{\lambda\lambda'}(\sigma_\mu\tau_\pm)_{\lambda\lambda'}a^\dagger_\lambda a_{\lambda'}$ is another simple operator that we can use to examine the behavior of shell-model wavefunctions. Here, one nucleon is created by the $a^\dagger$ operator and one is destroyed by the a operator. The spin and isospin operators, σ_μ and $\tau_\pm$, then act on the intermediate state and the that wavefunction is then overlapped with the final eigenstate wavefunction. We are especially interested in the question of GT transitions from excited states since these results cannot be studied experimentally. It is well known that the GT strength present in experimental data is consistently smaller than theoretical predictions. Within the $0d-1s$ shell-model space, the main factor contribution to the suppression is the mixing of the basis-state wavefunctions. The GT strength is highly sensitive to spin-isospin correlations. The residual interaction strongly mixes the orbital and spin components of angular momentum, but in general, the energetically lowest states prefer spatial symmetry and, accordingly, spin-isospin asymmetry of the many-body wave functions. Relative to the single-particle estimate, model calculations for Gamow-Teller strengths in transitions from the ground state are reduced. This is seen consistently when compared with experimental data. Contrary to that, at high excitation energy the GT strength increases. This shows the regular change of dominating orbital symmetry in coexistence with chaotic features of dynamics.

Since the pioneering work by Wigner 60 years ago [3], spin-isospin symmetry and

the properties of the nuclear interaction related to the GT strength have been studied in detail [4]. Although considerable work has been done for low-lying states, see for example [5], shell-model calculations examining GT transitions from excited states remain virtually non-existent. Such calculations give us important information about the behavior of a simple excitation mode in a realistic environment of incoherent nuclear interactions.

Finally, in chapter 6, I will summarize our findings for the spreading of basis states, the transfer of a single-nucleon, and Gamow-Teller transitions. We will also summarize our overall results for the spreading width for simple operators and our analysis of GT quenching. Finally, we will suggest interesting avenues that have yet to be explored.

1.2 Motivation

The two *sd*-shell nuclei we focus on, ^{28}Si and ^{24}Mg, are thoroughly studied nuclei, both experimentally and theoretically. Supported by the previous success of the shell model, we are confident in our ability to reproduce numerous observables for these nuclei in transitions from low-lying states. As far as the calculations are concerned, the space dimensions are of the order of 10^3 and are easy to handle computationally.

In addition to supplementing the information given by certain models for this mass region, our studies of these light nuclei are meant to serve as prototypes of general nuclear properties, including those for heavier nuclei. Certain observables for heavier nuclei remain beyond the scope of shell-model calculations due to the increase in the dimensionality of shell-model space. For example, ^{54}Fe has a model space with dimension of $\approx 10^5$ for 0^+0 states alone, which is too large to be handled by standard laboratory computers. In cases such as these, there are alternative methods, such as

the Shell-Model Monte Carlo (SMMC) method [7], however these methods have their own limitations.

One can compare results of shell-model calculations for GT transitions from excited states to the rates of certain astrophysical reactions, especially for those reactions involved in the late stages of supernovae. In fact, the β-decay strength function averaged over the final states of the daughter nucleus , and the level densities available for β-decay to excited states of the final nucleus are questions relevant to the r-process in stars.

For the most part, we are limited to $A \leq 50$ for exact calculations. This being the case, we choose to use two systems with which we are very familiar, to get an indication of the behavior of heavier nuclei. The exploration of basis-state mixing and spreading width, distributions for single-nucleon transfer, and total strength for Gamow-Teller transitions for excited states is extremely important for heavier nuclei. Our hope is that these studies will prove useful in understanding the general features of many-body quantum systems with strong interactions between constituents.

1.3 Background

One of the most important characteristics of the highly-excited states is given by the strength function of simple modes. An external field, for example of electromagnetic nature, acts by a simple one-body operator and excites, in the independent particle shell model, one particle – one hole ($1p - 1h$) states. In reality, such an excited state is a wave packet of many close stationary states. Each component carries a fraction of the strength of the original simple mode. An experiment with a resolution insufficient for the analysis of the dense fine structure spectrum displays a strength function related to the envelope of the strength distribution. Using the language of

time evolution, this is interpreted as damping of the simple mode [8]. With reasonable statistical assumptions about the nearest level-spacing distribution and the strength distribution among the invisible fine structure states, it is possible [9] to reconstruct their level densities and to recover the strength missing in the experiment with poor resolution.

The transitions that we are concerned with are those that can be described by the simple operators: $a^\dagger_\lambda$ and $[(\sigma_\mu \tau_\pm)_{\lambda\lambda'} a^\dagger_\lambda a_{\lambda'}]$. By looking at the shape of the strength function and measuring the spreading width for basis states, one-nucleon transfer distributions, and GT strengths, we hope to reach some general conclusions as to the effect the mixing of basis states has on transitions.

1.3.1 Basis State Spreading Widths

The most elementary aspect of the strength distribution is the relationship between the basis states and the eigenstates. One of the most widely accepted models, the standard model for the spreading width, predicts a Breit-Wigner strength distribution. However, he assumptions of the standard model for the spreading width break down when the width Γ_s obtained by Fermi's golden rule grows larger than the energy interval over which the background level density and/or the coupling matrix elements can be considered as approximately constant. The existence of this limit of "strong coupling" was recognized long ago by Wigner [10] and discussed in the banded random matrix models [11]. The deviations from the standard model are responsible [12, 13] for the narrow width of the double giant resonances [14]. The formulation of the general approach, which contains the standard model and strong coupling as particular limiting cases, was presented in [16].

As we stated earlier, each stationary state, or eigenstate, carries a fraction of the strength of the original simple mode. The strength function is then, a representation

of the strength distribution. Our analysis is of the shape of the strength distribution and the factors which contribute to the shape of the distribution; level density, weight, and interaction strength.

1.3.2 Spectroscopic Factors

The simplest type of transition is associated with the transfer of a single nucleon. The characteristics are given by the spectroscopic factor, S_j,

$$S_j = \frac{1}{2J_f + 1} |\langle f | a^\dagger_{j,t} | i \rangle|^2. \tag{1.1}$$

As we have already stated, the creation operator $a^\dagger$ creates a particle in the initial state, and the resultant wavefunction is then overlapped with the final state eigenfunction. In contrast to basis-state wavefunctions being overlapped with the eigenstate wavefunctions, in single-nucleon transfer we are considering initial and final states which are both eigenstates of their respective nuclei. Since the residual interaction has already been accounted for in the initial and final eigenstate wavefunctions, we suspect that the spreading width, which is an indication of the effect of mixing, will be smaller than that for basis state strength functions. The effect of one nucleon interacting with a well-defined many-body system, is smaller than the effect of A_v nucleons interacting in a system defined by indeprendent nucleons in a central field. If there were no mixing and the nucleons did not interact, then the initial state with a single nucleon added would be equivalent to a single final eigenstate and the width of the distribution would be zero.

In single-nucleon transfer reactions, the projectile either gains (pickup) or loses (stripping) a single nucleon as a consequence of interaction with the target nucleus. These transfer reactions are the focus of many experiments and their results form the large body of spectroscopic data available. What the data cannot tell us, due to the

short lifetimes and dense spectrum of excited states, are the amplitudes and cross-sections for these highly-excited states. Since this cannot be done experimentally, it is useful to use theoretical calculations for this as well. In chapter 4 we study the distributions resulting from one-nucleon transfer.

1.3.3 Gamow-Teller Strengths

One of the most useful methods for testing the scope of nuclear shell models, comes through the study of Gamow-Teller (GT) transitions. Experimentally, it is fortunate for us that there is a large pool of data for Gamow-Teller β-decay. Theoretically, it is to our benefit that the $\sigma\tau$ operator is "simple" enough to allow for detailed calculations.

There are a number of reasons to study GT transitions from excited states. One of the most well known being its obvious application to nuclear astrophysics. In high temperature astrophysical environments, nuclei exist in excited states in accordance with the Maxwell-Boltzmann distribution. Hence, one needs to understand the reaction rates and decay properties of these excited states. In nuclear reactions, the Hauser-Feshbach calculations give acceptable results for reaction cross sections for $N \approx Z$ nuclei in stars [6]. But one must try to achieve better accuracy in determining abundances in supernovae. These abundances are directly dependent on binding energies, statistics, and β-decay rates. For $A \leq 30$, where transition rates may be determined by a single state, the statistical Hauser-Feshbach formalism breaks down. Therefore, the results of shell model calculations for GT transitions from excited states are particularly important.

Although considerable work has been done for low-lying states, work done using shell-model calculations to examine Gamow-Teller transitions from excited states remains virtually non-existent. Here we do not account for the configurations outside

of the $0d - 1s$ shell model space and Δ-particle admixtures. My work concentrates instead on the dependence of the Gamow-Teller strength on the configuration mixing within the $0d - 1s$ shell-model space and its evolution as a function of excitation energy.

Chapter 2

Shell Model Calculations

2.1 The Shell Model

The shell model with semi-empirical residual interactions is currently the most reliable approach to microscopic calculations of nuclear properties. It is especially successful in relatively light nuclei. The matrix elements of the two-body interactions are fit by the known spectroscopic data for low-lying levels (see table A). With these matrix elements it is possible to reproduce numerous observable quantities for nuclei in the region of the *sd*-shell (^{16}O $\rightarrow$^{40}Ca). Because of this success, the nuclear shell model appears to be one of the most promising candidates for theoretical probing of the structure of complicated wave functions.

Shell-model basis states are related to the motion of independent nucleons in a static potential well. Assuming spherical symmetry of the potential, each nucleon moves in an "orbit" characterized by a definite energy and angular momentum. The shell model successfully reproduces the magic numbers. These numbers - 2, 8, 20, 50, 80, and 126 - are nucleon numbers that produce particularly stable nuclei. The shape of the ground states for these "closed shell" nuclei is indeed spherical. The correct

order and spacing is achieved by (1) using the Woods-Saxon (WS) potential

$$V(r) = -\frac{V_o}{[1 + exp\{(r - R)/a\}]} \tag{2.1}$$

and (2) incorporating a strong spin-orbit(SO) interaction

$$V_{SO} = \xi(r)(\mathbf{l} \cdot \mathbf{s}). \tag{2.2}$$

Each single-particle state is characterized by a specific (n, l, j, m) set. The single-particle wavefunction is can be written in the following form,

$$\Psi_a = R_{n,l}(r)Y_{l,m}(\theta, \phi). \tag{2.3}$$

The angular dependence of the wavefunction is given by the spherical harmonics $Y_{l,m}(\theta, \phi)$. The quantum number n, which corresponds to the number of nodes in the radial wavefunction $R_{n,l}(r)$ has values of $n = 1, 2, 3, \ldots$. In spectroscopic notation, the orbital angular momentum l is denoted with a single letter s, p, d, f, g, h and so on for $l = 0, 1, 2, 3, 4, 5, \ldots$. The total angular momentum j is a conserved quantity in the presence of the SO interaction and couples the spin and orbital angular momentum - $\vec{j} = \vec{l} + \vec{s}$. Each nucleon with orbital angular momentum l can have total angular momentum values of $j = (l \pm \frac{1}{2})$ as permitted by the triangle relation and magnetic projection values of $m_j = (-j, -j+1, \ldots, j-1, j)$. The strong spin-orbit interaction produces large level splittings between $j = l + \frac{1}{2}$ and $j = l - \frac{1}{2}$ orbits. The projection values m of the single-particle orbits allow a maximum occupancy of $\Omega = (2j + 1)$.

Figure 2.1 is a schematic diagram of single-particle energy level positions for the spherical shell model. As an example, we take the lowest single-particle orbit $1s_{1/2}$. This orbit has $(n, l, j) = (1, 0, 1/2)$, possible m values of $\pm 1/2$, and therefore a maximum occupancy of $\Omega = 2$. From left to right figure 2.1 shows (1) the harmonic oscillator major shell quantum number N where

$$E = \hbar\omega(N + \frac{3}{2}) \quad and \ N = 2n + l - 2, \tag{2.4}$$

(2) the Woods-Saxon levels without SO interaction, nl, (3) the Woods-Saxon levels with SO interaction, nl_j, and (4) to the far right, the maximum occupation, $\Omega = (2j+1)$. The circled numbers denote the sum $\sum\Omega$ with and without SO interaction.

Shell model calculations are comprised of three main components: (1) a choice of single-particle basis, (2) an active model space that depends on the nearest closed shell, and (3), an "effective" two-body interaction between nucleons. The three regions that must be determined are the inert, or "core", model space, that is fully occupied, the active model space, in which the valence nucleons above the core interact, and the empty model space which is never occupied by nucleons. This cutoff, or truncation, of the active shell-model space, means that the residual interaction must be renormalized in such a way that the effect of the space excluded due to the truncation is approximately included in the "effective" interaction.

The effective shell-model hamiltonian can be written in the form,

$$H = H_o + H' \tag{2.5}$$

where H_o is the independent-particle one-body term due to the inert core of ^{16}O, in the case of the *sd*-shell model space, plus the single-particle energies of the valence nucleons and H' is the two-body term due to the two-body antisymmetrized interaction of the valence nucleons.

The independent hamiltonian H_0 describes noninteracting fermions in the mean field of the appropriate spherical core. The single-particle orbitals $|\lambda)$ have quantum numbers $\lambda = (ljm\tau)$ of orbital (l) and total (j) angular momentum, projection $j_z = m$ and isospin projection τ. The eigenvalues ϵ_k of H_0,

$$H_0|k) = \epsilon_k|k), \tag{2.6}$$

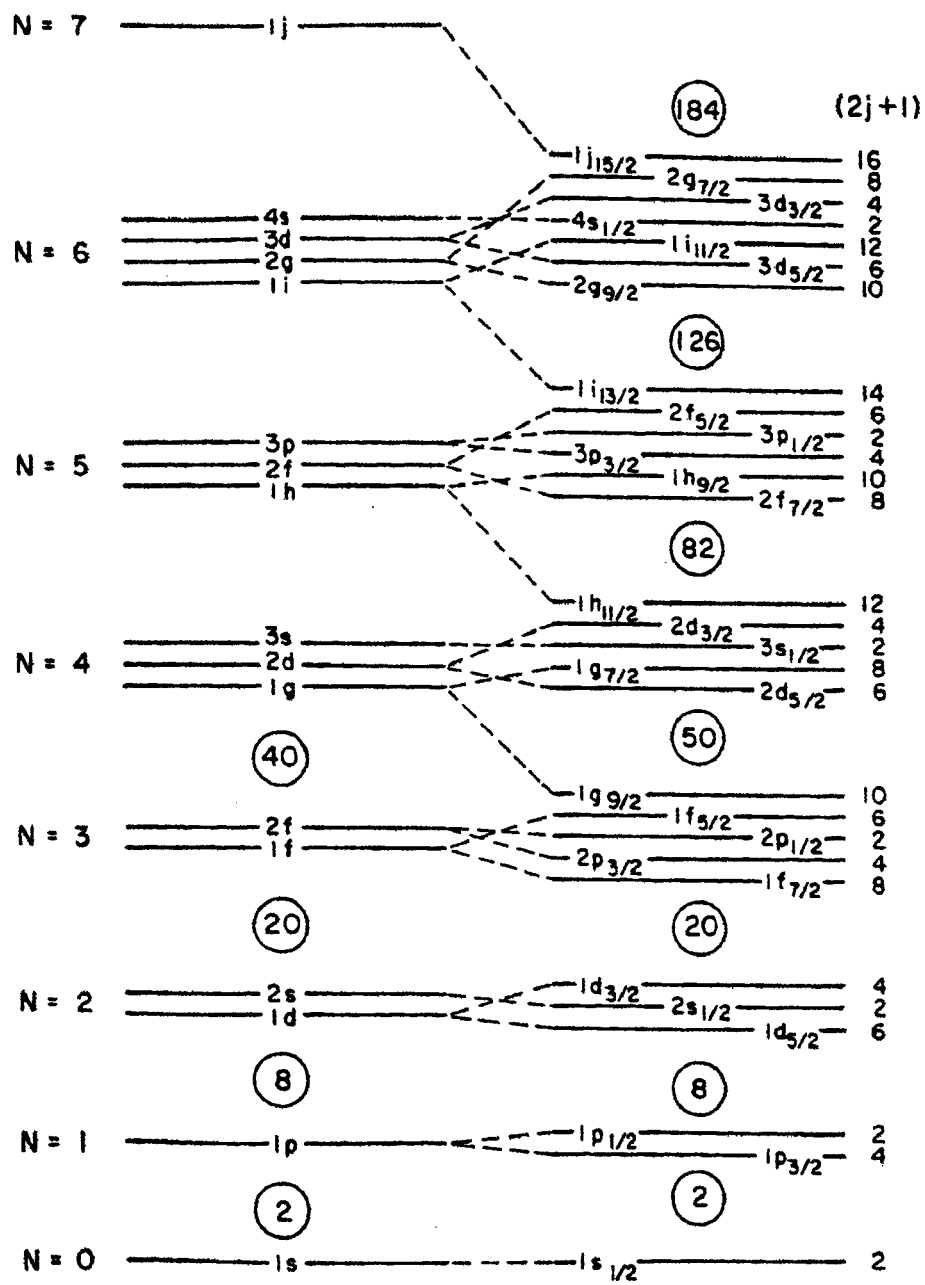

Figure 2.1: Schematic diagram of single-particle energy level positions for the spherical shell model (taken from [17]).

are highly degenerate. They are the sums

$$\epsilon_k = \sum_\lambda e_\lambda n_\lambda(k) \tag{2.7}$$

of energies e_λ of all orbits $|\lambda)$ occupied in a many-body configuration $|k\rangle$ with occupation numbers $n_\lambda(k)$, equal to 1 or 0.

Within our Hilbert space we have a truncated set of shell-model nuclear configurations. Within each configuration, there are a number of ways to occupy the magnetic substates of the j-levels in the active model space. These variations give rise to the m-scheme Slater determinants. The m-scheme wave function for n nucleons can be expressed as

$$\Psi_n = \frac{1}{\sqrt{n!}} \sum_P (-1)^P P \, \Psi_{j_1,m_1}(1) \Psi_{j_2,m_2}(2) \ldots \Psi_{j_n,m_n}(n) \,, \tag{2.8}$$

where P is the permutation to be summed over. Expressed as a Slater determinant,

$$\Psi_n = \frac{1}{\sqrt{n!}} \begin{vmatrix} \Psi_{j_1,m_1}(1) & \Psi_{j_2,m_2}(1) & \ldots & \Psi_{j_n,m_n}(1) \\ \Psi_{j_1,m_1}(2) & \Psi_{j_2,m_2}(2) & \ldots & \Psi_{j_n,m_n}(2) \\ \vdots & \vdots & \vdots & \vdots \\ \Psi_{j_1,m_1}(n) & \Psi_{j_2,m_2}(n) & \ldots & \Psi_{j_n,m_n}(n) \end{vmatrix} \tag{2.9}$$

Our basis states, $|k\rangle$ are combinations of numerous m-scheme determinants that result in good quantum numbers, J, M, π, T and T_3, which are the total angular momentum, its projection, the parity, the isospin and its projection.

One can introduce configurations (partitions) $\mathcal{P}$ defined by the occupancies $n_\lambda(k)$ of single-particle orbitals. All states $|k\rangle$ belonging to a partition $\mathcal{P}$ have the same number of particles in each orbital $n_\lambda(k)$. For all partitions, $\sum_\lambda n_\lambda(k) = A_v$, where A_v is the total number of valence particles. The organization of the model space in partitions presents two useful features. First, a subspace of the m-scheme states,

defined by a given configuration $\mathcal{P}$, is invariant with respect to the projection onto good total angular momentum J and total isospin T,

$$\mid JT;\ k \subset \mathcal{P}\rangle = \hat{P}_{JT} \mid MT_3;\ m_k \subset \mathcal{P}\rangle = \sum_{m \subset \mathcal{P}} X_m^{JTk} \mid MT_3;\ m\rangle. \tag{2.10}$$

This can be easily seen using the exact expression for the projection operator

$$\hat{P}_{J_\circ T_\circ} = \prod_{J \neq J_\circ}^{J_{max}} \frac{\hat{J}_-\hat{J}_+ + \hat{J}_3^2 + \hat{J}_3 - J(J+1)}{J_\circ(J_\circ+1) - J(J+1)} \prod_{T \neq T_\circ}^{T_{max}} \frac{\hat{T}_-\hat{T}_+ + \hat{T}_3^2 + \hat{T}_3 - T(T+1)}{T_\circ(T_\circ+1) - T(T+1)}. \tag{2.11}$$

Secondly, the m-scheme states and, as a consequence of the invariance of the projection, the projected states (2.10) also, are degenerate with respect to the one-body part of the hamiltonian, H_o.

To construct the many-body wave functions with good spin J and isospin T quantum numbers, we start with the m-scheme determinants which have, for given J and T, the maximum spin and isospin projection,

$$\mid M = J\, T_3 = T;\ m\rangle, \tag{2.12}$$

where m spans the m-scheme subspace of states with $M = J$ and $T_3 = T$.

The $J - T$ projected states $|k\rangle$ and the effective hamiltonian, (2.10) and (2.5), are used to construct the hamiltonian matrix, $\langle JT;\ k\,|H|JT;\ k\,\rangle$. Once diagonalized, this matrix produces our eigenvalues and eigenvectors;

$$H|\alpha\rangle = E_\alpha|\alpha\rangle. \tag{2.13}$$

The necessity of using the $J-T$ projected states with the appropriate total angular momentum, parity and isospin ($J^\pi T$) instead of the simple m-scheme determinants was demonstrated already in the first studies of quantum chaos in the nuclear shell model [19]. The popular cranking model [20] does not preserve the angular momentum. It operates with quasiparticle configurations similar to those of the m-scheme of

the spherical shell model but taken for a deformed uniformly rotating field. Absence of correct premixing (or angular momentum projection) implies artificial mixing by the residual interaction since angular momentum selection rules are lifted. In the shell model the number of particles is conserved, and the quantum numbers characterizing a given state are those of exact integrals of motion, total angular momentum, parity and isospin.

2.2 The $0s - 1d$ Shell Interaction

We use the Wildenthal hamiltonian [1] which defines the single-particle energies and the interaction between the valence particles by fitting close to 450 binding energies and excitation energies for the *sd*-shell nuclei. In this work we carry out calculations exclusively for the states with total angular momentum (J), parity(π), and isospin (T) of $J^\pi T = 0^+0$ in the many-body systems of 12 and 8 particles above the inert core of ^{16}O. The $A_v = 12$ system can be considered as a model for the ^{28}Si nucleus. Examples of other shell model applications for similar purposes can be found in [21]. The 0^+0 class contains $N = 839$ states (see table B.1). They are partitioned into the shell model configurations according to the occupation numbers $n_\lambda(k)$ of the spherical single-particle orbits $\{(nl_j)\} = 0d_{5/2}, 0d_{3/2}$ and $1s_{1/2}$. For $A_v = 8$, or ^{24}Mg, the 0^+0 class contains $N = 325$ states (see table B.2).

It is good to note here that spatial symmetry is energetically favorable. The central potential dominates the two-body interaction, producing a finite short-range attraction for states that have $l_1 = l_2$ and no short-range attraction for $l_1 \neq l_2$. Expressed as a complete set of functions, the interaction can be written as

$$V(r) = \sum_{k=0}^{\infty} v_k(r_1, r_2) P_k(cos\theta), \tag{2.14}$$

where $P_k(cos\theta)$ are the Legendre polynomials

$$P_k(cos\theta) = \sum_q 4\pi/(2k+1) Y^*_{kq}(\Omega_1) Y_{kq}(\Omega_2). \tag{2.15}$$

Where Y_{kq} are the spherical harmonics mentioned earlier (Sect. 2.1).

Table A lists the two-body reduced matrix elements of the residual interaction within the *sd* shell-model space. It shows the attractive behavior of the $T = 1$ states with even angular momenta. All of the matrix elements with $T = 1$ and $J = 0, 2$ and 4 are negative. These T and J values are the only ones allowed for identical nucleons in the same j-orbit. There is also a strong attractive diagonal component for isoscalar $T = 0$ pairs. In contrast to that, the $T = 0$ off-diagonal matrix elements are mainly repulsive in nature. In all, most of the large matrix elements of the residual interaction are negative. The diagonal part of the interaction attractive and results in a downward shift of the energy spectrum. In our discussion of total Gamow-Teller strengths, we will return to the issue of spatial symmetry and asymmetry.

Our shell model calculations are carried out using the Oxford-Buenos-Aires-Shell-Model (OXBASH) code [2] with the Wildenthal (USD) two-body interaction. The original configurations are described in the m-scheme. This requires, as a prerequisite for the diagonalization, the construction, with the help of the projection operators, of the proper linear combinations of the m-states within a partition which have the desired values $J^\pi T$. These superpositions form the basis states $|k\rangle$. The OXBASH computer program uses (1) m-scheme basis states and (2) angular momentum projection operators ($\hat{P}_{JT}$), to build and diagonalize matricies with good J and T in the isospin formalism. As discussed in [21], the projection procedure already creates fairly complex non-determinantal states which still have very close bare energies.

OXBASH contains seven major computer codes: 'BASIS', 'PREDICT', 'PROJ', 'MATRIX', 'LANCZOS', 'MVEC', and 'TRAMP'. Appendix C is the output from

the 'BASIS' computer code. 'BASIS' generates an m-scheme Slater determinant basis for a particular number of particles with a particular $J_z^\pi T_z$. A file is created to store the single-particle states, and restrictions can be placed on the J-orbits and the major shells. The output details the number of partitions, the placement of valence nucleons into single-particle j-levels for each partition, and the m-scheme and j-scheme dimension for each partition. It also gives the number of states with a certain spin(J) and isospin(T).

2.3 The Scope of the Shell Model

As stated earlier, with the correct order and spacing of the nucleon energy levels, the shell model reproduces a host of observables. To that end, we examine figures 2.2 and 2.3 which compare experimental energies and predicted energies using the Wildenthal (W) interaction [1].

Figure 2.2 shows the experimental (left) and theoretical (right) energy spectra for ^{27}Al, ^{28}Si, and ^{29}Si. The experimental and theoretical values are connected by a line for each of the three nuclei. The slopes of the lines correspond to rms deviations on the order of 180-190 keV. Figure 2.3 shows the values for two-neutron separation energy obtained with the W interaction. The isotopes are connected by solid lines and the deviations between experiment and theory $[S_{2n}(th) - S_{2n}(exp)]$ are indicated by the diameter and placement, relative to the lines, of the circles. With the notable exception of ^{31}Na, ^{31}Mg, and ^{32}Mg, the circles are consistent with the discrepancy of 180-190 keV [22].

In addition to the single-particle energy levels, the nuclear shell model with realistic interactions is successful in predicting r.m.s. radii, magnetic moments, quadrupole moments, electromagnetic moments, electron scattering, and beta decay.

On the left side of figure 2.4 the GT strength obtained from either β^+ or β^- decay of $0d-1s$ shell nuclei is compared with theory. T(GT), usually denoted $B(GT)$, represents the summed strength normalized by the sum-rule value of $3(N-Z)$. It is usually less than unity because the β-decay Q-value limits the decay to the lower part of the Gamow-Teller strength function. Theoretically the configurations outside of the $0d-1s$ shell-model space as well as Δ-particle admixtures are responsible for this reduction [18]. These higher-order effects can be approximately taken into account by the introduction of an effective GT operator, $O(GT)_{eff} = 0.77 \times O(GT)_{free}$, where $O(GT)_{free}$ is the free-nucleon operator. Comparisons of experiment with the effective operator calculations are shown on the right side of figure 2.4.

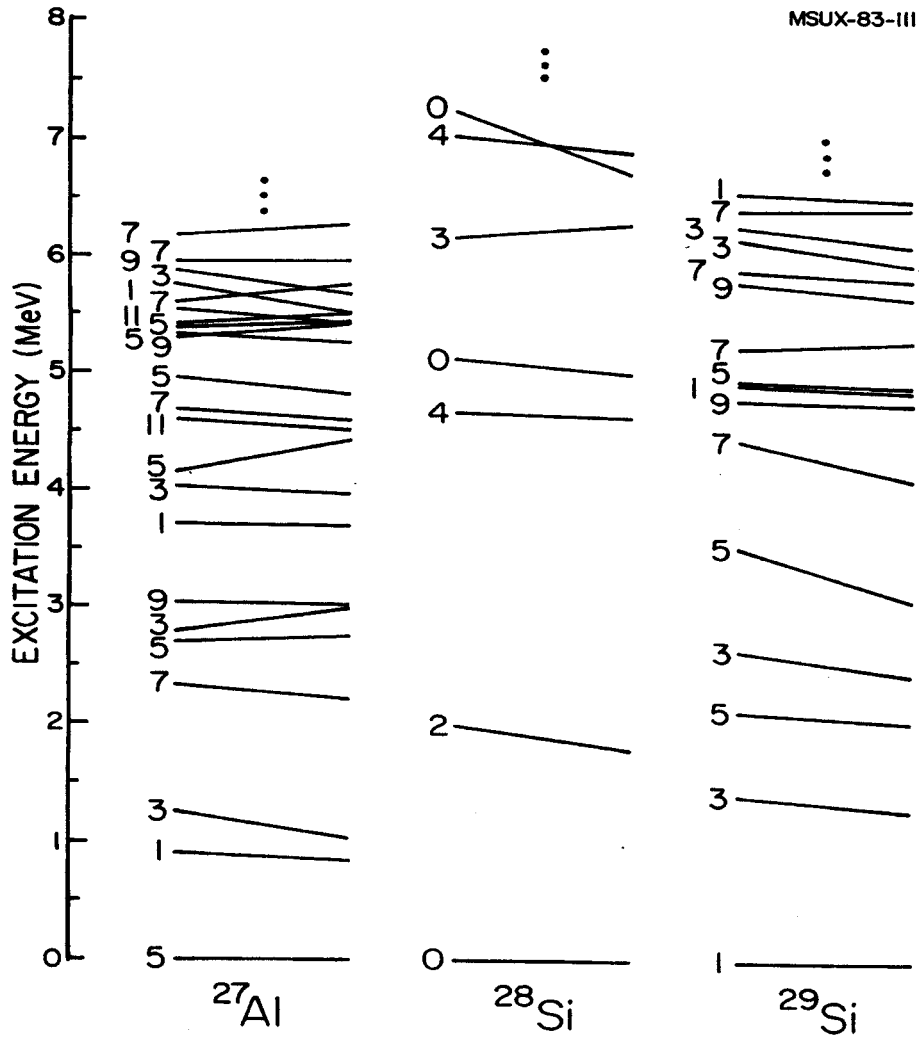

Figure 2.2: Energy levels - experiment (right) *vs.* theory (left) for three *sd*-shell nuclei using the W interaction (taken from [22]).

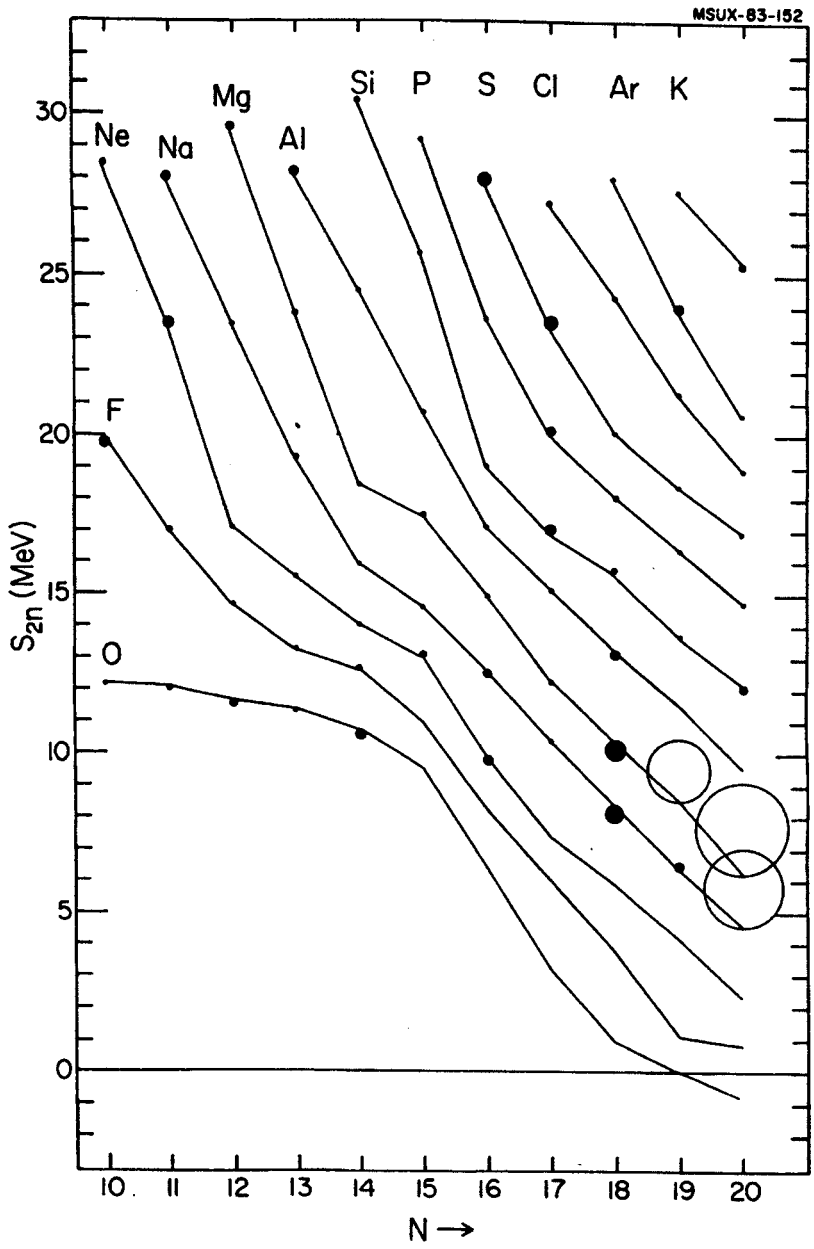

Figure 2.3: Two-neutron separation energy, S_{2n} for *sd*-shell nuclei - experiment *vs.* theory, as a function of neutron number N (taken from [22]).

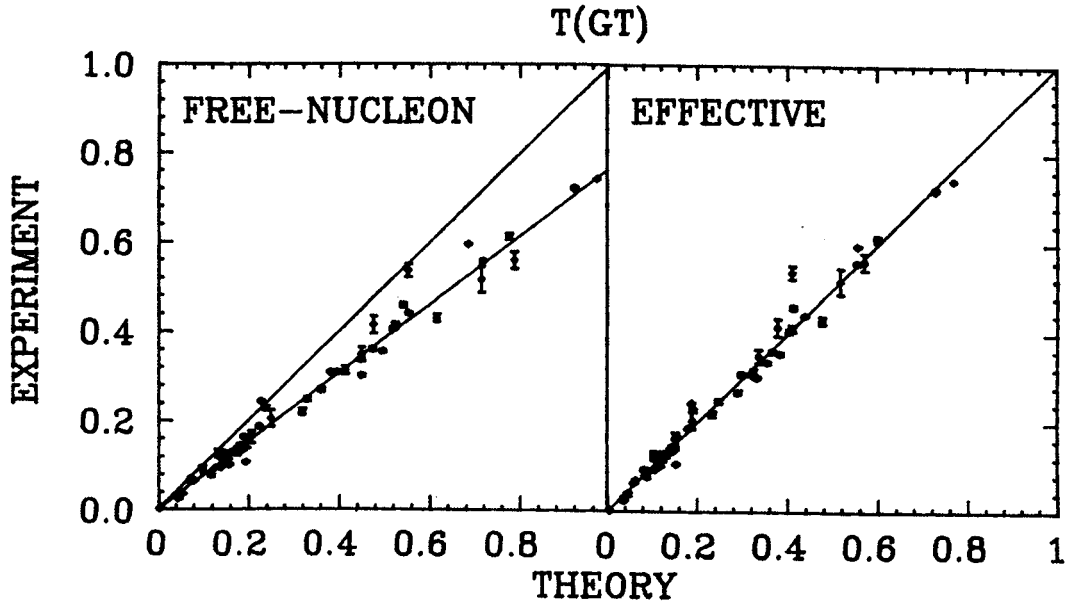

Figure 2.4: $B(GT)$ for ground states of different *sd*-shell nuclei; experiment versus theory for the free-nucleon, panel *a*, and the effective, panel *b*, GT operator (taken from [1]).

Chapter 3

Spreading Width of Shell Model Basis States

3.1 Background

3.1.1 Definitions

We consider a quantal system governed by the hamiltonian H in a truncated space spanned by the finite set of the basis states $|k\rangle$. In the independent-particle shell-model basis, the hamiltonian (2.5) contains the unperturbed configuration energies, given by H_o, and the residual interaction, given by H'. In the actual nuclear diagonalization, the integrals of motion, total angular momentum (J), parity (π) and isospin (T), are exactly preserved by the projection of the simple shell model m-scheme Slater determinants so that all states under consideration have the same exact quantum numbers $J^\pi T$.

The residual interaction has both diagonal $\tilde{H}$ and off-diagonal $\hat{H}$ matrix elements;

$$H' = \tilde{H} + \hat{H}. \tag{3.1}$$

It is convenient to include the diagonal part of the residual interaction $\tilde{H}$ in the unperturbed hamiltonian. The single-particle eigenfunctions $|k\rangle$ then satisfy the expression

$$H_{kk}|k\rangle = (H_o + \tilde{H})|k\rangle = \bar{E}_k|k\rangle \tag{3.2}$$

By including $\tilde{H}$, we remove the strict degeneracy of the pure shell-model configurations corresponding to a single partition.

If we now diagonalize the full hamiltonian matrix, including the off-diagonal matrix elements H'_{kl}, we deviate from the basis states $|k\rangle$ and obtain the eigenstates $|\alpha\rangle$ and their energies E_α,

$$H|\alpha\rangle = E_\alpha|\alpha\rangle. \tag{3.3}$$

The eigenstates are complicated superpositions of the basis states;

$$|\alpha\rangle = \sum_k C_k^\alpha |k\rangle. \tag{3.4}$$

The fragmentation of basis states, $|k\rangle = \sum_\alpha C_k^\alpha|\alpha\rangle$, is described by the same transformation coefficients C_k^α, which can be taken as real in our case of time reversal invariance.

In contrast to the Gaussian Orthogonal Ensemble (GOE), where the all basis states are uniformly mixed, the actual shell-model hamiltonian matrix does not couple each individual state with all others. The two-body interaction leads to the specific selection rules which allow the matrix elements only between configurations which differ in orbits of not more than two particles. This brings the matrix closer to the type described by the banded random matrix ensembles (BRME)[11]. However our many-body matrix elements are determined by a much smaller number of independent two-body matrix elements (63 for the *sd*-shell), and therefore cannot be considered as uncorrelated, which is the case in the BRME. The ensembles based on two-body random interactions in a many-body system were discussed in [23, 24].

The fragmentation, or distribution of strength, of the basis states over the eigenstates $|\alpha\rangle$ is determined by the transformation coefficients C_k^α of eq.(3.4). More specifically, it is determined by the weights of the components

$$W_k^\alpha \equiv (C_k^\alpha)^2. \tag{3.5}$$

This fragmentation is the focus of our studies in section 3.2.

Using completeness arguments, the average characteristics of the fragmentation can be expressed directly in terms of the matrix elements of the hamiltonian (2.5). For a given basis state $|k\rangle$, the centroid, or mean value, of the strength distribution coincides with the unperturbed energy (3.2),

$$\begin{array}{rcll} \bar{E}_k & = & \sum_\alpha E_\alpha W_k^\alpha & = \sum_{\alpha\alpha'} \langle k|\alpha\rangle\langle\alpha|H|\alpha'\rangle\langle\alpha'|k\rangle \\ & = & H_{kk} & = \epsilon_k + \tilde{H}_{kk} \end{array} \tag{3.6}$$

We define the higher (central) moments of the strength function as

$$\sigma_k^{(n)} = \sum_\alpha (E_\alpha - \bar{E}_k)^n W_k^\alpha. \tag{3.7}$$

The second moment of the strength distribution is determined by the sum of all off-diagonal matrix elements (starting at a given basis state) squared,

$$\sigma_k^2 \equiv \sum_\alpha (C_k^\alpha)^2 (E_\alpha - \bar{E}_k)^2 = \sum_{l\neq k} (H'_{kl})^2. \tag{3.8}$$

Note that this clearly demonstrates the relationship between the dispersion σ_k and the residual interaction, H'_{kl}, for a given unperturbed initial state. We will use the notation

$$\overline{\sigma^2} = \frac{1}{N}\sum_k \sigma_k^2 = \frac{1}{N}\Big(\sum_\alpha E_\alpha^2 - \sum_k \bar{E}_k^2\Big) \tag{3.9}$$

for the average dispersion of the states $|k\rangle$. The centroids and dispersions can also be obtained for a subclass of the states $|k\rangle$, for example, for each partition $\mathcal{P}$ separately.

For $A_v = 12$, the energy dispersion (3.8) of individual 0^+0 basis states turns out (Fig. 3.1) to be remarkably uniform, with $\sigma_k \approx \bar{\sigma} \approx 10$ MeV over the entire space. Similarly, for the system of $A_v = 8$ we have $\bar{\sigma} \approx 9$ MeV. The dispersion σ_k is closely related to the spreading width defined more precisely in Sect. 3.2.1. The uniformity of the dispersion supports the idea of saturation of the spreading width [25, 16] which has important consequences for understanding the damping of giant resonances.

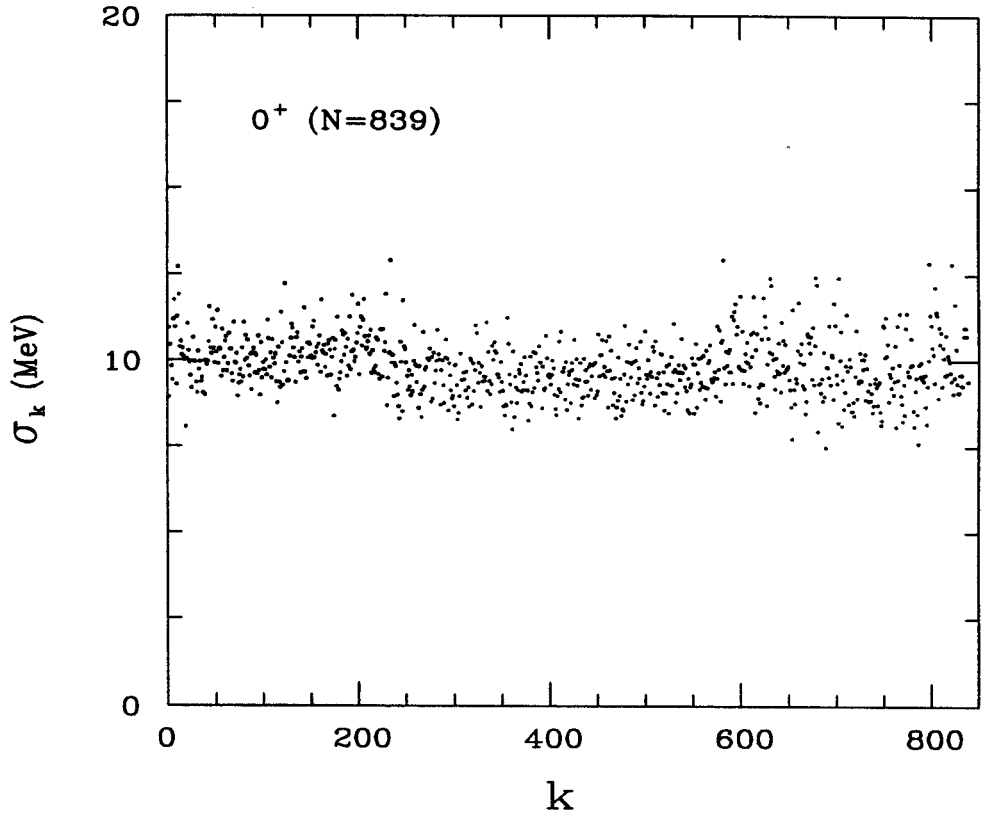

Figure 3.1: Energy dispersions σ_k of $J^\pi = 0^+, T = 0$ basis states of ^{28}Si.

Our objective is to describe how the amplitude for a particular basis state $|k\rangle$ may be distributed over the stationary states $|\alpha\rangle$ of a complex many-body system. Once accurately described, the distribution tells us what fraction of the original strength is in each excited state. If the distribution were described by a Gaussian

$$f(x) = f_o exp\left[\frac{(x-\mu)^2}{2\sigma^2}\right] \tag{3.10}$$

then it would have a Full Width at Half-Maximum(FWHM) of

$$\Gamma_{gauss} = \sqrt{8\,ln2}\;\sigma \;=\; 2.355\,\sigma. \tag{3.11}$$

Theoretically, all the moments of the strength distribution can be found from the strength function

$$F_k(E) = \sum_\alpha (C_k^\alpha)^2 \delta(E - E_\alpha). \tag{3.12}$$

As compared to the full density of states

$$\rho(E) = \sum_\alpha \delta(E - E_\alpha), \tag{3.13}$$

the strength function (3.12) is frequently called the "local density of states". $F_k(E)$ determines the contribution of the basis state $|k\rangle$ to $\rho(E)$ at $E = E_\alpha$,

$$F_k(E) = \rho(E)\langle (C_k^\alpha)^2\rangle_{E_\alpha = E}. \tag{3.14}$$

The level spectrum for excited states is very dense. As the energy increases the level density progresses from the number discrete states within a infinitesimal energy range to an envelope of states within a small energy region. This smearing, or , of the states is approximated Eq.(3.14) by a histogram where we sum over the eigenstates within a narrow energy bin. Each bin contains many states with close degrees of complexity. The functions are normalized according to

$$\int dE\rho(E) = N, \quad \int dE F_k(E) = 1. \tag{3.15}$$

Here N is the total dimension of the Hilbert space.

3.1.2 The "Standard Model" of the Spreading Width

The definition of the spreading width traditionally assumes that the decomposition of the simple state in terms of the stationary components with energies E_α has the Breit-Wigner shape. This would correspond to the pure exponential decay of a simple excitation with the mean lifetime $\tau \sim \hbar/\Gamma$. This is the case in the "standard" model [4] of the strength function, where a simple mode is coupled with the infinite picket fence of complicated background states through constant (or weakly fluctuating) matrix elements.

In the standard derivation of the spreading width [4], there are two steps.

1. Express the many-body hamiltonian in an intermediate basis in which a single state is coupled to the "background" of remaining states.

   To do this, one singles out a state $|k\rangle$ which is removed from the hamiltonian matrix.

$$H = \begin{pmatrix} H_{1,1} & H_{1,2} & H_{1,3} & \dots & \boldsymbol{H_{1,k}} & \dots \\ H_{2,1} & H_{2,2} & H_{2,3} & \dots & \dots & \dots \\ H_{3,1} & H_{3,2} & \dots & \dots & \vdots & \dots \\ \vdots & \vdots & \vdots & \vdots & \vdots & \vdots \\ \boldsymbol{H_{k,1}} & \dots & \dots & \dots & \boldsymbol{\bar{E}_k} & \dots \\ \vdots & \vdots & \vdots & \vdots & \vdots & \vdots \end{pmatrix} \tag{3.16}$$

   Once this state is excluded, the $(N-1) \times (N-1)$ submatrix of the hamiltonian is fully diagonalized to give intermediate eigenvectors $|\nu\rangle$ and eigenvalues E_ν. This diagonalization defines the transformation matrix $\langle k'|\nu\rangle$. The full matrix expressed in the basis $(|k\rangle, \{|\nu\rangle\})$ has the unperturbed energy $\bar{E}_k$ and intermediate energies E_ν on the main diagonal and off-diagonal matrix elements

$$V_{k\nu} = V_{\nu k} = \sum_{k' \neq k} H'_{kk'} \langle k'|\nu\rangle \tag{3.17}$$

in the k^{th} row and the ν^{th} column, $\nu \neq k$, due to the coupling between the single state $|k\rangle$ and the background.

$$H = \begin{pmatrix} \bar{E}_k & V_{k,2} & V_{k,3} & \dots & V_{k,\nu} & \dots \\ V_{2,k} & E_2 & 0 & 0 & 0 & \dots \\ V_{3,k} & 0 & E_3 & 0 & 0 & \dots \\ \vdots & 0 & 0 & \ddots & 0 & \vdots \\ V_{\nu,k} & 0 & 0 & 0 & E_\nu & \dots \\ \vdots & \vdots & \vdots & \vdots & \vdots & \ddots \end{pmatrix} \tag{3.18}$$

The advantage of this approach is that the omission of a single state cannot significantly change the statistical properties of the dense spectrum. We can expect that the level density of the background is the same as in the exact solution including all N states.

2. Diagonalization of the intermediate hamiltonian.

The problem of interaction of a single state with background states is easily solved. The exact energies $E = E_\alpha$ are the roots of the secular equation (poles of the Greens function $G(E)$)

$$G^{-1}(E) \equiv E - \bar{E}_k - \sum_\nu \frac{V_{k\nu}^2}{E - E_\nu} = 0. \tag{3.19}$$

The intermediate energies E_ν and the matrix elements (3.17) do depend on the choice of the removed state $|k\rangle$ but the roots E_α do not.

The eigenstates $|\alpha\rangle$ are the combinations

$$|\alpha\rangle = C_k^\alpha |k\rangle + \sum_\nu B_\nu^\alpha |\nu\rangle, \tag{3.20}$$

where the amplitudes C_k^α, which coincide with those in (3.4), determine the fraction of the strength of a simple state $|k\rangle$ carried by an eigenstate $|\alpha\rangle$.

Eliminating the coefficients B_ν^α with the use of the Schrödinger equation

$$\begin{array}{lll} \langle k|H|\alpha\rangle & = & \langle k|H\, C_k^\alpha|k\rangle \quad +\langle k|H\sum_\nu B_\nu^\alpha|\nu\rangle \\ E_\alpha\, C_k^\alpha & = & \bar{E}_k\, C_k^\alpha + \qquad \sum_\nu V_{k\nu} B_\nu^\alpha \end{array} \tag{3.21}$$

and normalizing the wave function, we obtain the weights

$$W_k^\alpha \equiv (C_k^\alpha)^2 = \Big(\frac{dG^{-1}}{dE}\Big)^{-1}_{E=E_\alpha} = \Big[1+\sum_\nu \frac{V_{k\nu}^2}{(E_\alpha - E_\nu)^2}\Big]^{-1}, \tag{3.22}$$

or the residues of $G(E)$.

The results of the standard model are based on additional assumptions.

(a) The background spectrum is dense and rigid so one can consider instead an equidistant sequence of levels with the mean spacing D. ($E_\nu = \nu\, D$; $\nu = 0, \pm 1, \pm 2, \ldots$)

(b) This spectrum does not considerably change due to the removal of a single state $|k\rangle$.

(c) The mixing is sufficiently strong, $\langle V^2\rangle/D^2 \gg 1$.

(d) The coupling intensities $V_{k\nu}^2$ are uncorrelated with the energies E_ν of the background states and weakly fluctuate around the mean value $\langle V^2\rangle$.

According to (3.14) the dense uniform background is characterized by the level density $\rho(E) \simeq D^{-1}$. Therefore, one can introduce a smooth strength function $F_k(E)$ of the state $|k\rangle$,

$$F_k(E) = \sum_\alpha W_k^\alpha \delta(E - E_\alpha) = \rho(E)\langle W_k^\alpha\rangle_{E_\alpha = E} \tag{3.23}$$

where the average is taken over several eigenstates in the vicinity of energy E. The assumptions of the standard model allow one to substitute $V_{k\nu}^2$ effectively by the appropriate average value $\langle V^2\rangle$. The following summation over the infinite picket fence of the background states implies the infinite energy dispersion.

Under these assumptions, and using (3.19) and (3.22), it is easy to calculate the sums over the intermediate states ν (see appendix D) and to obtain a strength function (3.14) of Breit-Wigner shape

$$F_k(E) = \frac{1}{2\pi} \frac{\Gamma_s}{(E - \bar{E}_k)^2 + \Gamma_s^2/4} \tag{3.24}$$

where the spreading width Γ_s is given by the "golden rule"

$$\Gamma_s = 2\pi \frac{\langle V^2 \rangle}{D}. \tag{3.25}$$

The expressions (3.24) and (3.25) are sometimes taken for granted although they are valid under the above-mentioned assumptions only.

3.2 Strength Functions of Shell Model States

There are 63 independent two-body interaction matrix elements which define all many-body matrix elements (see Appendix A) for the $0d - 1s$ shell-model space. Therefore, the many-body matrix elements cannot be considered uncorrelated as in the GOE or BRME. The global properties of the mixing interaction are seen [21] by inspection of the matrix H' prior to the actual diagonalization. The second moment σ_k (3.8) stays essentially constant for the majority of the states $|k\rangle$. Its fluctuations are presumably of statistical character. The constancy of σ_k (figure 3.1) is one of the manifestations of the N-scaling [26, 27] in that, as the mixing proceeds, involving the increasing number N of fine structure states, each coupling matrix element diminishes $\propto 1/\sqrt{N}$ keeping the sum (3.8) constant. The same phenomenon is responsible for the saturation of the damping width of giant resonances [28, 29] and isobaric analog resonances [30, 31].

3.2.1 Strong Coupling Limit

As discussed in [21], (d) is the most vulnerable assumption of the standard model. That the coupling intensities $V_{k\nu}^2$ are uncorrelated with the energies E_ν of the background states is correct only as long as the resulting standard spreading width is relatively small. In general, the matrix elements decrease as one moves away from the centroid of the original state. This can be understood from the band-like structure of the shell-model hamiltonian. Therefore, Γ_s should be compared with the energy range ΔE over which the level density and the coupling matrix elements can be considered as approximately constant.

In the framework of the shell model, the two-body interactions are capable of admixing the close configurations of gradually increasing levels of complexity. The shell-model selection rules define, for each basis state, its doorway states as those participating in the first mixing step. In the exciton (particle-hole) language these doorway states belong to the same or next level of complexity. Because doorway states have their own finite spreading widths, their strength covers a finite range of energy ΔE. Outside of this interval the magnitude of the coupling matrix elements $V_{k\nu}$ decreases. As discussed in [12, 15], this restricts the validity of the standard model and can bring the shape of the strength function closer to Gaussian.

The finiteness of this energy interval plays no role if $\Gamma_s < \Delta E$. The formal limit of $\Delta E \to \infty$ corresponds to the standard model. But as the coupling strength and the spreading width increase, the finite size of the doorway strength interval becomes important. One can estimate what happens in this limit assuming that the coupling $V_{k\nu}^2$ suddenly disappears at some finite distance $\Delta E = E_\nu - \bar{E}_k$ from the centroid $\bar{E}_k$. The strength distribution is then determined by the outer roots of the secular

equation (3.19) which are located at the distance

$$(E_\alpha - \bar{E}_k)^2 = \sum_\nu V_{k\nu}^2 = \sigma_k^2 \tag{3.26}$$

where the last equality follows from the definition (3.8), the expression for the transformed coupling matrix elements (3.17), and the completeness of the set of the intermediate states $|\nu\rangle$ in a space of dimension $(N-1)$.

The result (3.26) allows one to say that the bulk of the distribution lies between $+\sigma_k$ and $-\sigma_k$. From there we can give a simple estimate

$$\Gamma_{SC} \approx 2\,\sigma_k \tag{3.27}$$

for the spreading width in the limit of complete mixing. Written as (3.27), the expression for the spreading width does not refer to the specific form of decrease of the coupling matrix elements $V_{k\nu}$ as one moves away from the centroid $\bar{E}_k$. Using the idea of uniformity of complicated states in a given energy region [16, 21] we expect small variations of the width for various states $|k\rangle$ in this limit. Indeed, the quantity σ_k is found to be roughly constant for all states.

The new and important property of the strong coupling limit (3.27) is that the quadratic dependence of the spreading width on the interaction strength is replaced by the linear dependence. Such a prediction was first made on qualitative grounds [12] in relation to the problem of the damping width of the double giant resonances. In the harmonic approximation for the giant mode, the matrix elements $V_{k\nu}$ of coupling between the collective n-phonon state $|k\rangle$ and the compound states $|\nu\rangle$ scale as $\sqrt{n}$. Therefore, in agreement with data [14], the ratio $\Gamma(n)/\Gamma(1)$ of the widths of the multiple and single excitations should increase $\propto \sqrt{n}$ in the strong coupling limit (3.27) rather than $\propto n$ as predicted by the golden rule (3.25) with the quadratic dependence on the coupling matrix elements.

The detailed behavior of the spreading width as a function of the interaction strength depends on the explicit dependence of (1) the level density and (2) the coupling matrix elements on energy of the background states. The general theory which incorporates this behavior as input and then predicts the strength function and the value of the spreading width was developed in [16], see also [21]. When going from weak to strong coupling, the strength function evolves from a Breit-Wigner distribution, eq.(3.24), to a nonuniversal shape with a finite second moment. The spreading width (defined as the FWHM) undergoes a transition from the standard golden rule quadratic expression to the linear dependence, similar to our estimate (3.27).

In the region of chaotic dynamics one defines a generic strength function, $F(E)$, of the basic states where the basis state label k is omitted. Of course, there can be fluctuations of the spreading width from one basis state to another one. The case of the collective state with a nongeneric strength function was studied in [16].

Figure 3.2a shows a total energy level spectrum of 325 0^+0 states (see table B.2) for 8 valence particles (^{24}Mg nucleus) as a function of a parameter λ (in percent) taken as a common factor in front of the residual off-diagonal interaction hamiltonian $\hat{H}$ ($H' = \tilde{H} + \lambda \hat{H}$), where $\lambda = 1$ corresponds to the realistic strength. One can also see the overall repulsive effect of the interaction on the spacing of the levels. Figure 3.2*b* shows the same set of levels on an unfolded number scale, and a magnified fragment containing about 30 levels in the middle of the spectrum is shown in 3.2*c*. The uniform level spacing of the unfolded scale allows us to concentrate on the fluctuations of each state as a function of interaction strength. The avoided crossings, being very frequent at $\lambda \leq 0.4$, become more rare at larger λ. As discussed in [32], as λ increases, the "gas" of levels with finite N is expanding. This general expansion is clearly seen in Fig. 3.2a. It goes approximately linearly with λ. In this region the increase of λ

mainly rescales the energies rather than mixes the states.

The direct diagonalization of the hamiltonian matrix results in the energies E_α of the eigenstates $|\alpha\rangle$ and their wave functions expressed as the superpositions (3.4) of the basis states. The level density (3.13) has a Gaussian shape with the variance which broadens by 5 Mev from $\lambda = 0$ to $\lambda = 1$. The mean level spacings near the middle of the spectrum are $D_0 = 24$ keV and $D = 40$ keV for $\lambda = 0$ and $\lambda = 1$, respectively. It is known [23, 33] that the Gaussian shape occurs mainly due to combinatorial reasons for the two-body interaction in the many-body system, irrespectively of the random or deterministic nature of the two-body matrix elements. In contrast, the Wigner semicircle level density is obtained for the uncorrelated many-body matrix elements in a full or banded (but sufficiently wide) matrix [21].

The local level statistics display an onset of chaos already for the weak interaction, $\lambda \approx 0.2$. The complexity of the eigenstates and the related localization length measured in the original basis continue to regularly evolve beyond this point. This manifests the greater sensitivity, compared to energy levels, of the wave functions to the deviations from the chaotic limit. Below we concentrate on the structure of the individual eigenstates which will allow us to extract the generic strength function.

3.2.2 Shape of the Strength Function

The presence of single-particle and collective motion (shape vibrations, rotation and giant resonances in nuclei) associated with simple excitation modes displays the regular mean field component of dynamics persisting in the stochastic region. Of course, those states are highly fragmented and the concept of the localization length of an eigenstate can be translated into the conventional notion of the spreading width [4] of a basis state.

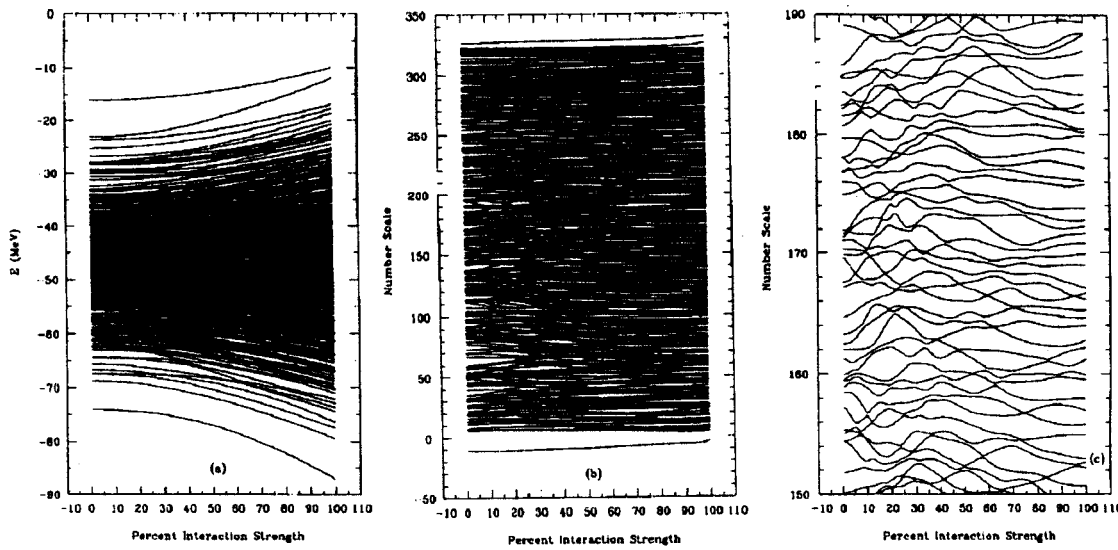

Figure 3.2: Parametric spectrum of 325 $J^\pi = 0^+, T = 0$ states in the $(0d1s)^8$ shell-model. Shown as a function of the residual interaction strength, λ - (a) on an energy scale, (b) unfolded, and (c) unfolded on an expanded portion of the spectrum (taken from [21]).

One of the main conclusions of the analysis given in [21] was that of similarity of individual wave functions in the chaotic region, in accordance with Percival's conjecture [34]. The degree of complexity of the eigenstates measured by the moments of the distribution function of the amplitudes C_k^α was found to saturate in the central part of the spectrum. The average properties of the eigenstates with approximately the same degree of complexity can be related to thermodynamical entropy and temperature of the equilibrium thermal ensemble [35]. These properties can be extracted by averaging out the fluctuations. We expect that the closely related problem of the fragmentation of the basis states over the eigenstates can be solved similarly.

There are three obvious possibilities for the shape of the strength function distribution; (a) a sharp peak, (b) a smeared distribution of finite width, and (c) a constant distribution of infinite width. Options (a) and (c) are the extremes of either complete order, in which case $C_k^\alpha = \delta_{k\alpha}$ and $|k\rangle = |\alpha\rangle$, or complete chaos where $C_k^\alpha = C_o = 1/\sqrt{N}$ for N dimensions. Option (b) implies a relation between the strength function $F_k(E)$ and the energy difference of $E - \bar{E}_k$. All three possibilities are shown in figure 3.3a - c.

Figure 3.3 clearly displays the relation between localization and spreading width; with 3.3a being completely localized, and 3.3c being completely delocalized. Fig. 3.4 shows the "empirical" strength functions $F_k(E)$, eq.(3.14), for nine individual basis states $|k\rangle$ with centroids $\bar{E}_k$ located in the middle of the spectrum.

The histograms obtained with the bin size of 1 MeV are plotted as a function of the energy distance from the corresponding centroid. Taking the basis states in this high-density, mid-energy range as members of a statistical ensemble, we superimpose their strength functions in order to reduce the statistical fluctuations and produce a smooth "generic" strength function. In Fig. 3.4 this averaging is performed over

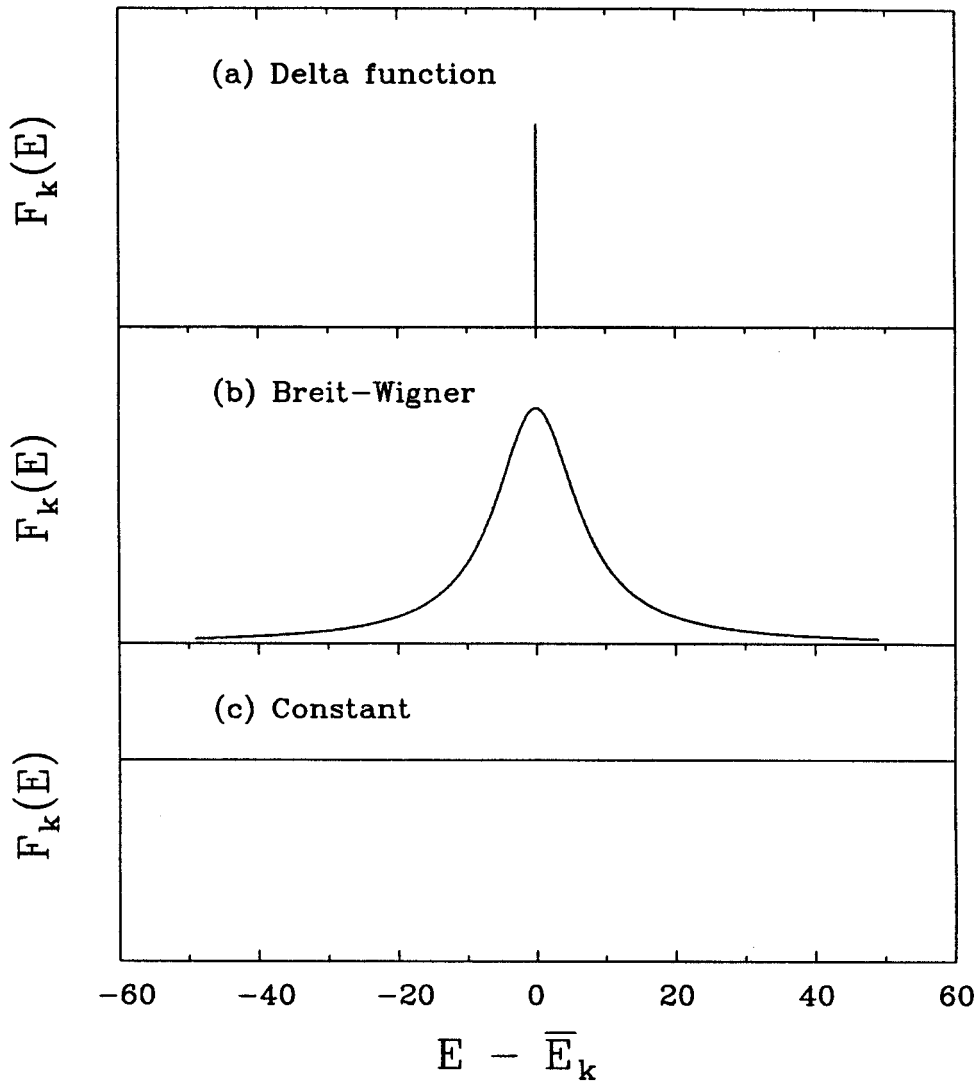

Figure 3.3: Three possible strength function distributions for basis states $|k\rangle$ (histograms) plotted as a function of the energy distance, $E - \bar{E}_k$, from the centroid of the unperturbed state $|k\rangle$.

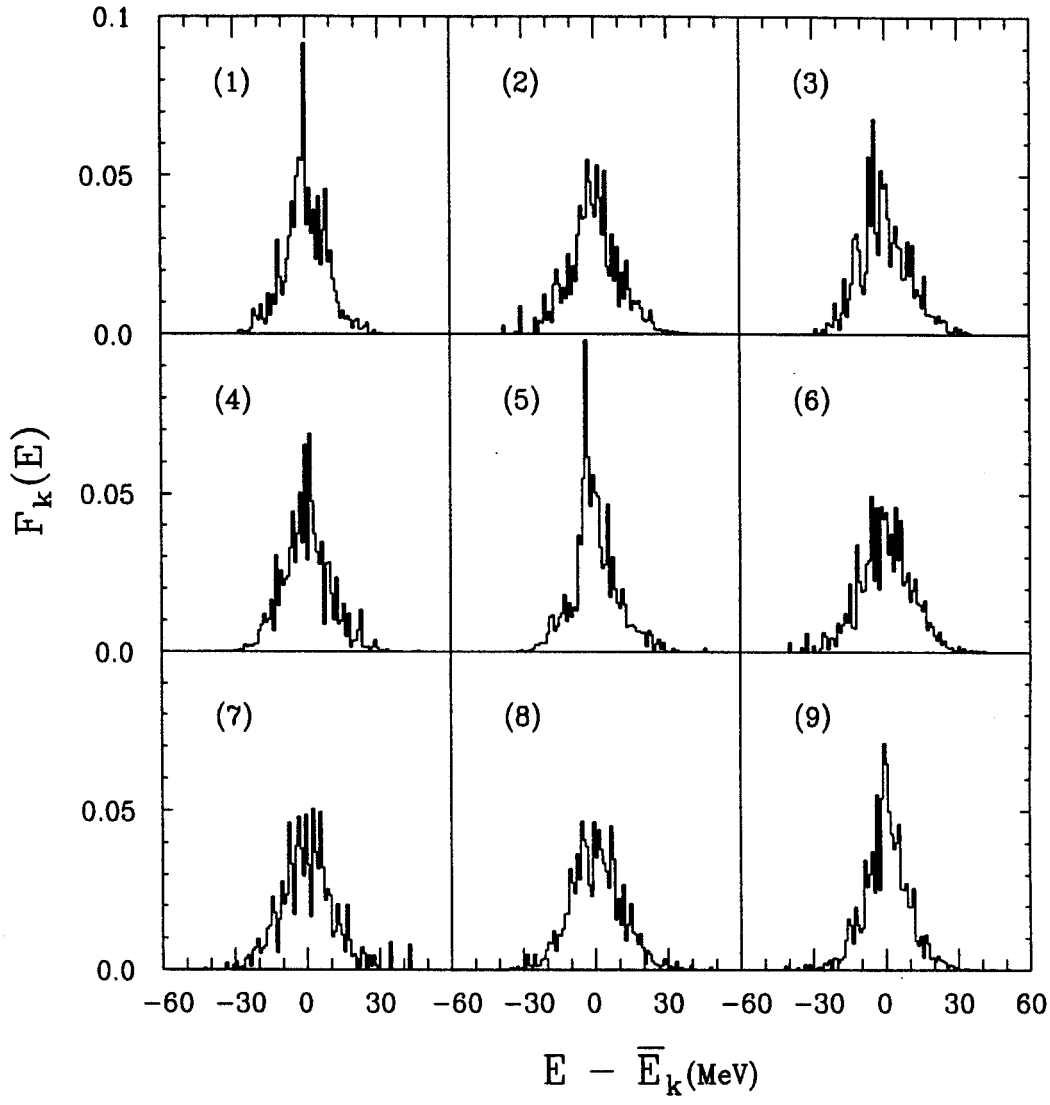

Figure 3.4: The strength functions for 9 individual 0^+0 basis states $|k\rangle$ in the middle of the spectrum (histograms) *vs* the energy distance, $E - \bar{E}_k$, from the centroid of the unperturbed state $|k\rangle$, panels *1* - *9*. The bin size is 1 MeV.

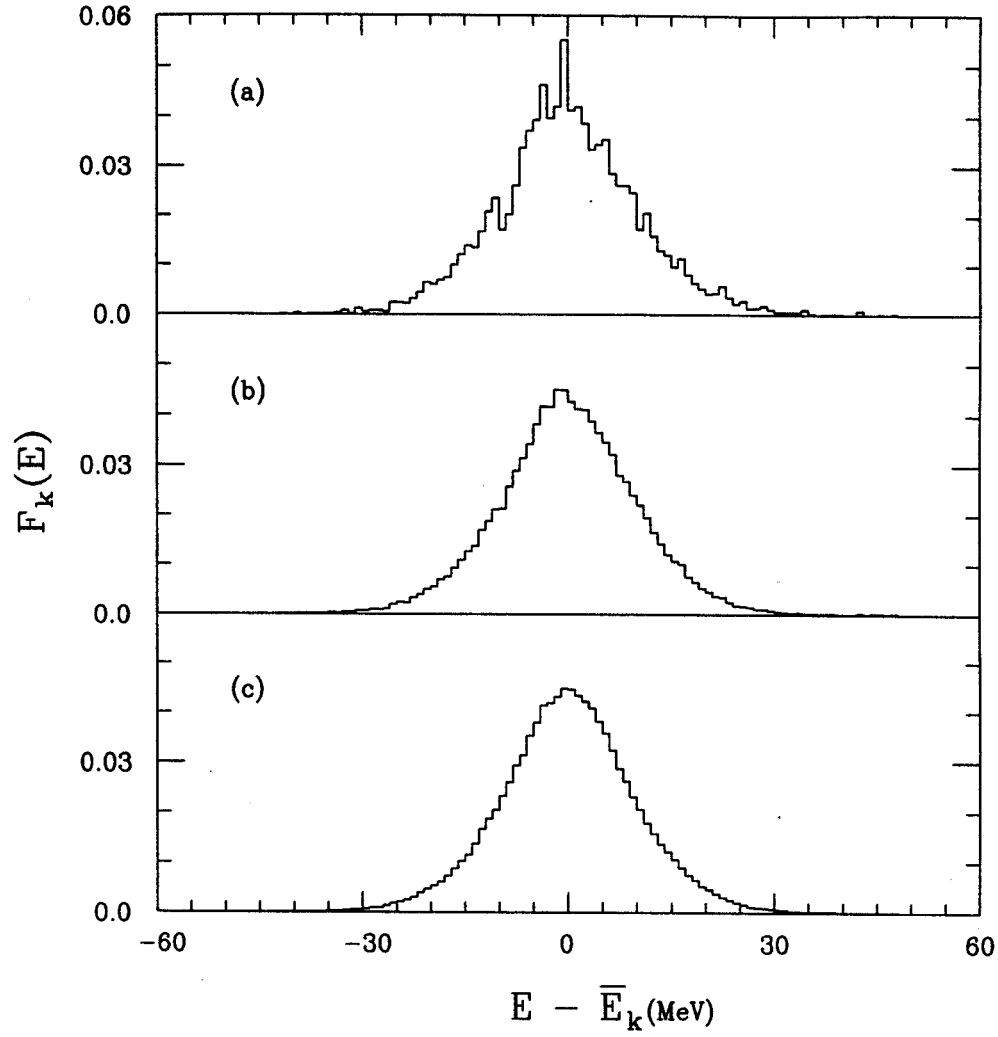

Figure 3.5: The strength function averaged over 10, 100, and 400 states in the middle of the spectrum, panels *a* - *c*, respectively. The bin size is 1 MeV.

10, 100 and 400 basis states, parts 3.5a, 3.5*b* and 3.5*c*, respectively. The resulting strength function is already very smooth at the step *b*.

Fig. 3.6a demonstrates that the Breit-Wigner curve does not fit particularly well in any region. For the detailed fit we use the histograms with the finer bin size of 100 keV. The wings of the curve are decreasing much faster than expected for the Breit-Wigner distribution. Our attempt, Fig. 3.6*b*, to fit only the central region results in an extremely poor fit to the tails, Fig. 3.6*c*. The poor fit implies that the

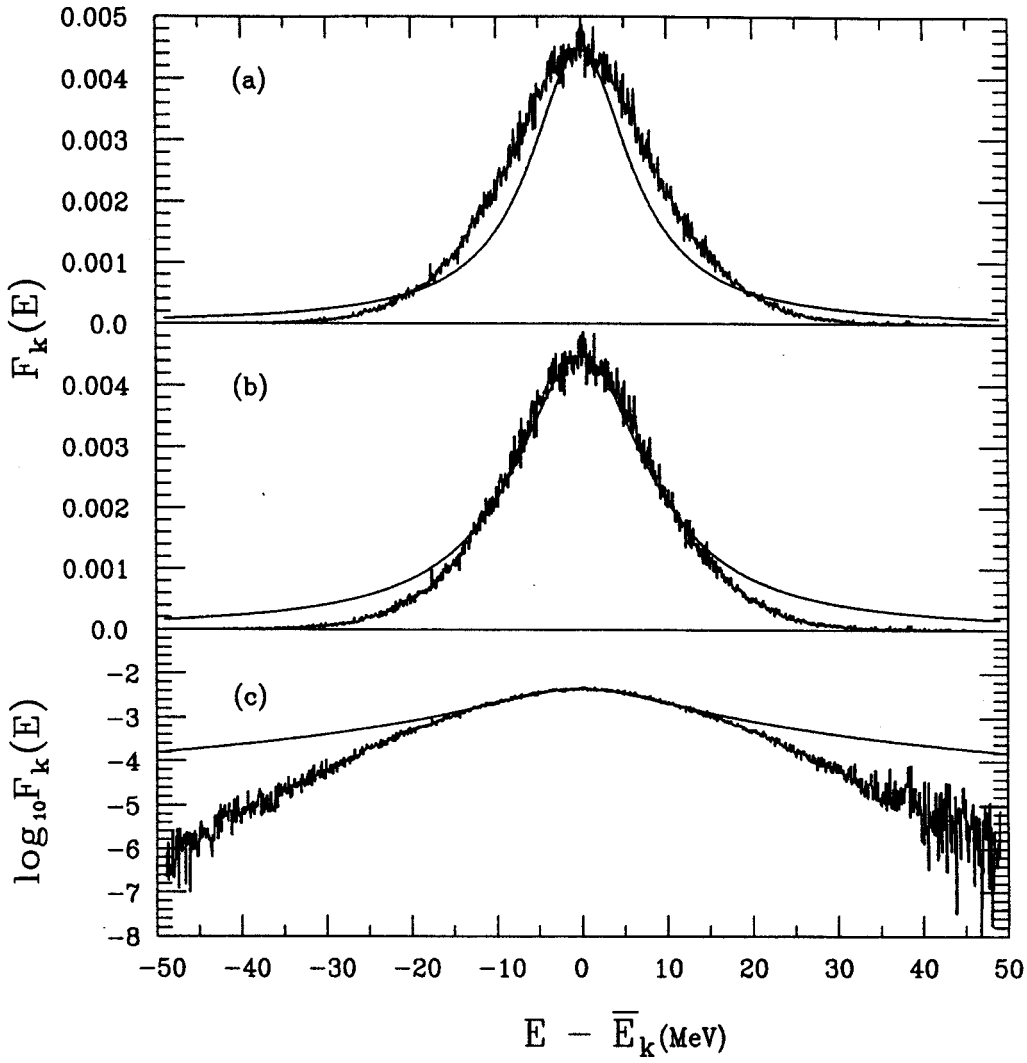

Figure 3.6: The overall Breit-Wigner fit (solid lines) to the strength function of Fig. 3.5, *c* (histograms), panel a, to the central part of the strength function of Fig. 3.5, *c* (histograms), panel *b*, and the same fit on the logarithmic scale, panel *c*. The bin size is 100 keV.

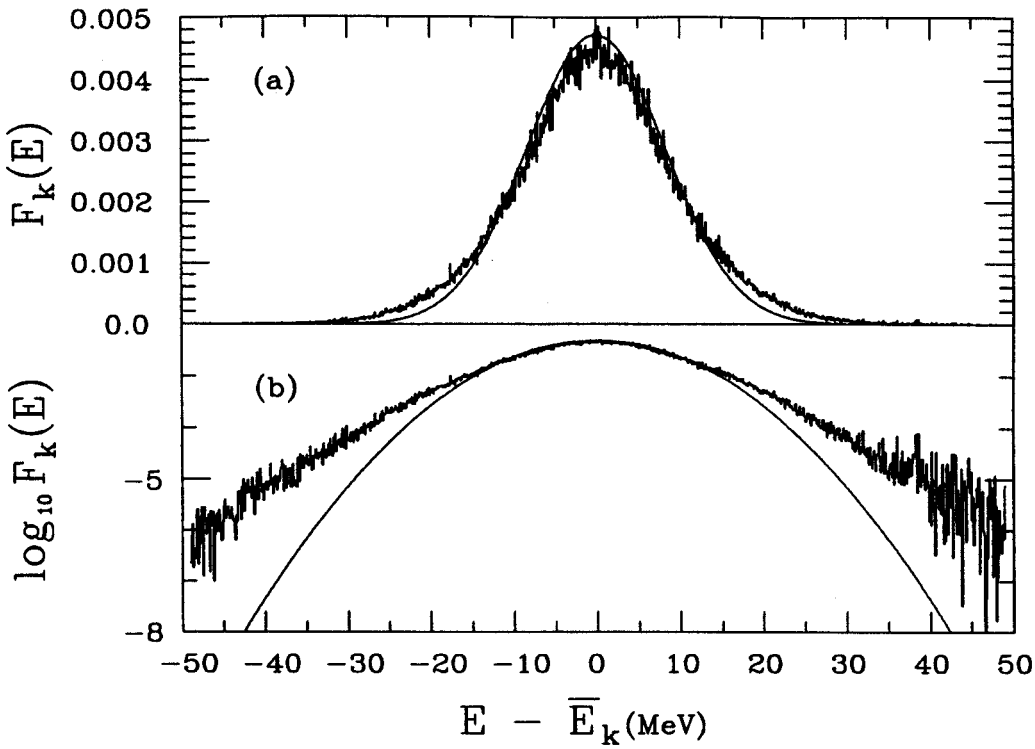

Figure 3.7: The Gaussian fit (solid lines) to the strength function of Fig. 3.5, *c* (histograms), panel *a*, and the same fit on the logarithmic scale, panel *b*. The bin size is 100 keV.

strong coupling case is closer to reality for the states in the middle of the spectrum at the actual interaction strength.

Although the BW fit can be used to determine the FWHM, the overall Gaussian fit, Fig. 3.7*a*, is a better fit to the distribution. The variance of the basis-state strength functions obtained from the Gaussian fit, $\sigma_{basis} = 8.3 \pm 0.3$ MeV, the typical spreading width (FWHM) of the central 0^+0 states equals $\Gamma_{basis} = \sqrt{8 \ln 2}\, \sigma_{basis} = 19.6 \pm .7$ MeV. This agrees with the estimate (3.27), $\Gamma_{basis} = 2\bar{\sigma} = 20$ MeV made for the strong coupling limit. Again we observe deviations from the Gaussian shape in the tails of the strength function, Fig. 3.7*b*.

Because of the breakdown of both the Gaussian and the Breit-Wigner fits for the tails of the strength function, it becomes necessary to examine both the central region and the tails of the distribution more closely. If we fit a Gaussian to the only central

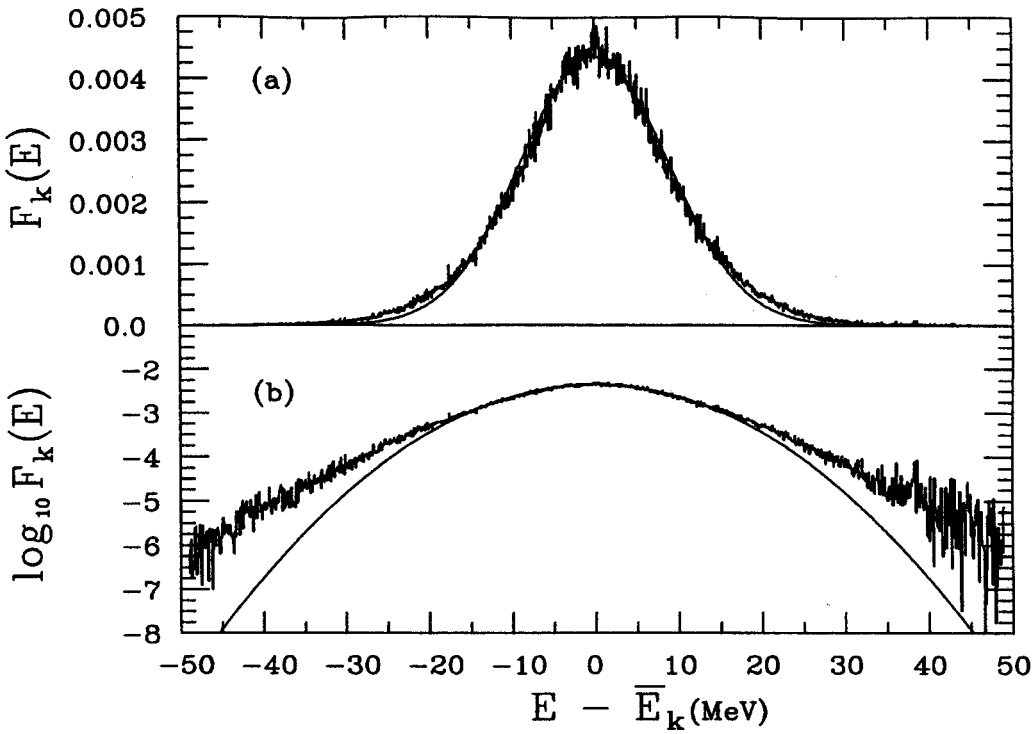

Figure 3.8: The Gaussian fit (solid lines) to the strength function of Fig. 3.5, *c* (histograms), panel *a*, and the same fit on the logarithmic scale, panel *b*. The bin size is 100 keV.

portion of the distribution (figure 3.8), the variance increases to $\sigma_{basis} = 8.9 \pm 0.7$ MeV, and the spreading width (FWHM) of the central 0^+0 states equals $\Gamma_{basis} = 21.0 \pm 1.6$ MeV.

According to eq.(3.14), the strength function histograms actually involve two factors, the average value $\langle (C_k^\alpha)^2 \rangle$ of the eigenfunction components corresponding to the basis state $|k\rangle$, and the level density $\rho(E)$. The level density itself is described [21] by the Gaussian curve of Fig. 3.9. This is typical [23] for the many-body systems with two-body interactions in the finite Hilbert space. The level density effects dominate the central part of the strength function distribution. Eliminating the level density from the strength function, we come to the "pure" weight function $W_k^\alpha = \langle (C_k^\alpha)^2 \rangle$ of Fig. 3.10.

We see that the Breit-Wigner shape that fit poorly to the strength function (Fig.

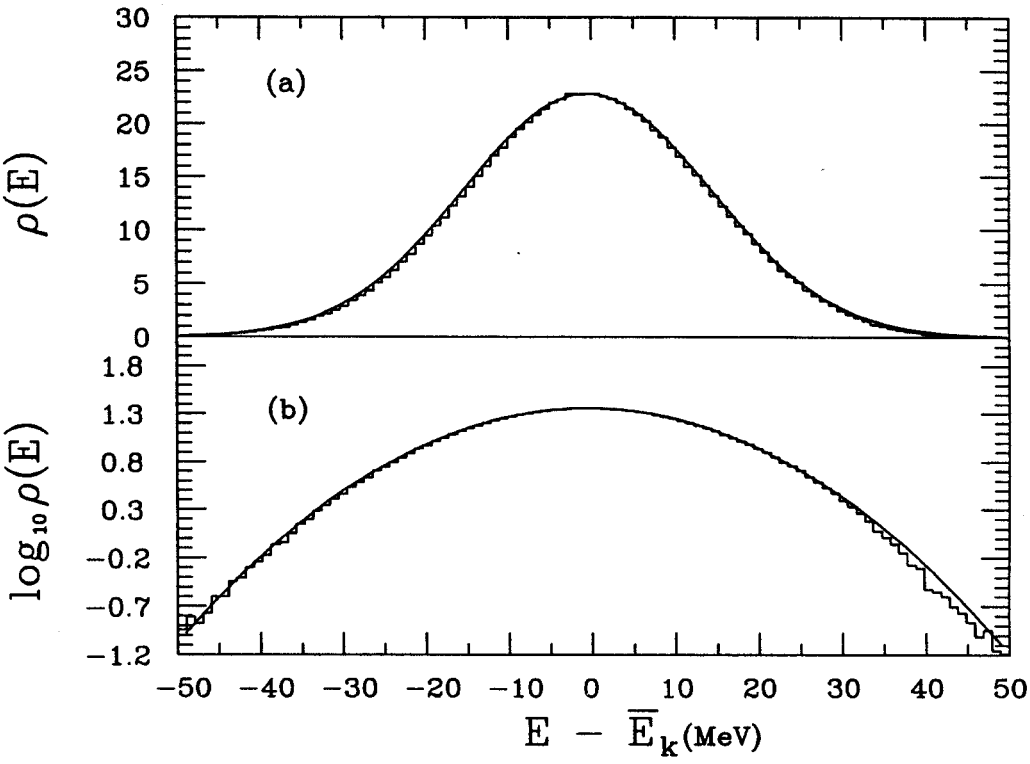

Figure 3.9: Gaussian fit (solid lines) to the level density, $\rho(E)$, for the strength function averaged over 400 states, panel a, and the same fit on the logarithmic scale, panel *b*. The bin size is 1 MeV.

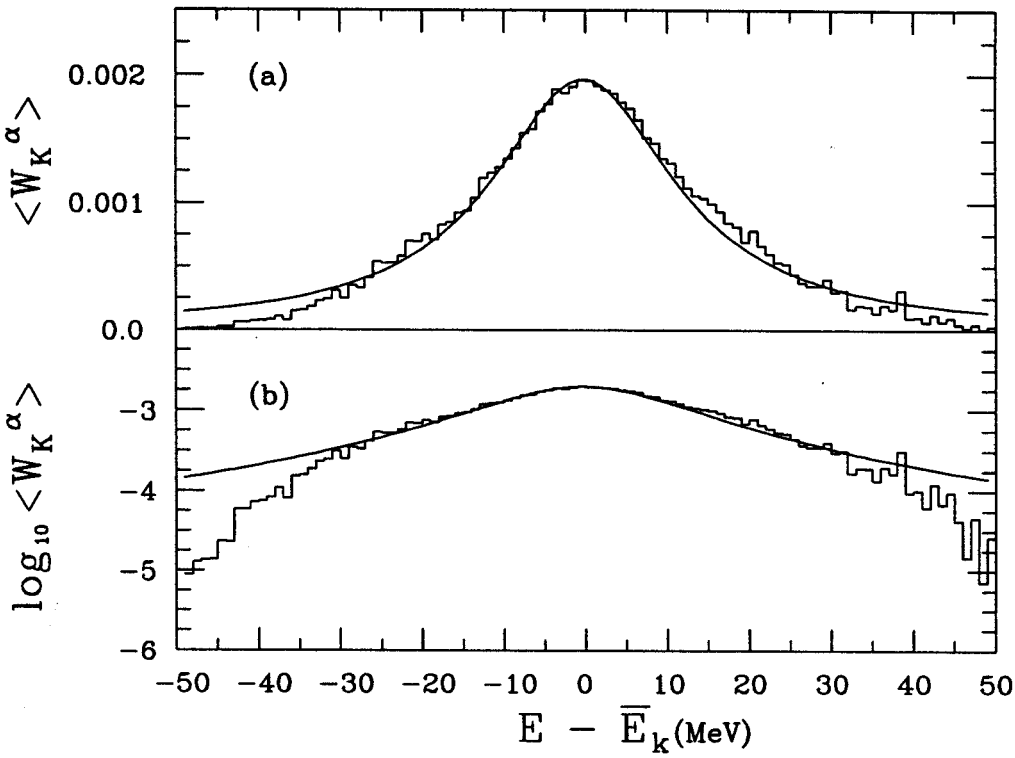

Figure 3.10: Breit-Wigner fit (solid lines) to the average weight, $\langle W_k^\alpha \rangle = \langle (C_k^\alpha)^2 \rangle$, for 400 states, panel a, and the same fit on the logarithmic scale, panel *b*. The bin size is 1 MeV.

3.6a) is noticeably improved in the central region for the pure weight function of Fig. 3.10a. The tail of the weight distribution on a logarithmic scale shows a linear behavior, Fig. 3.10*b*. It is clear from Fig. 3.11, especially from the logarithmic plot of Fig. 3.11*b*, that such an exponential fit does, in fact, represent the tails of the strength distribution. The final form of this fit is

$$F_k(E-\bar{E}_k) \approx F_0 \exp\Big(-\frac{E-\bar{E}_k}{E_l}\Big) \tag{3.28}$$

where the energy localization length is $E_l = 5$ MeV. Of course, the expression (3.28) is valid only for the tails of the distribution, $(E-\bar{E}_k) > \Gamma$. The exponential behavior holds for at least three orders of magnitude.

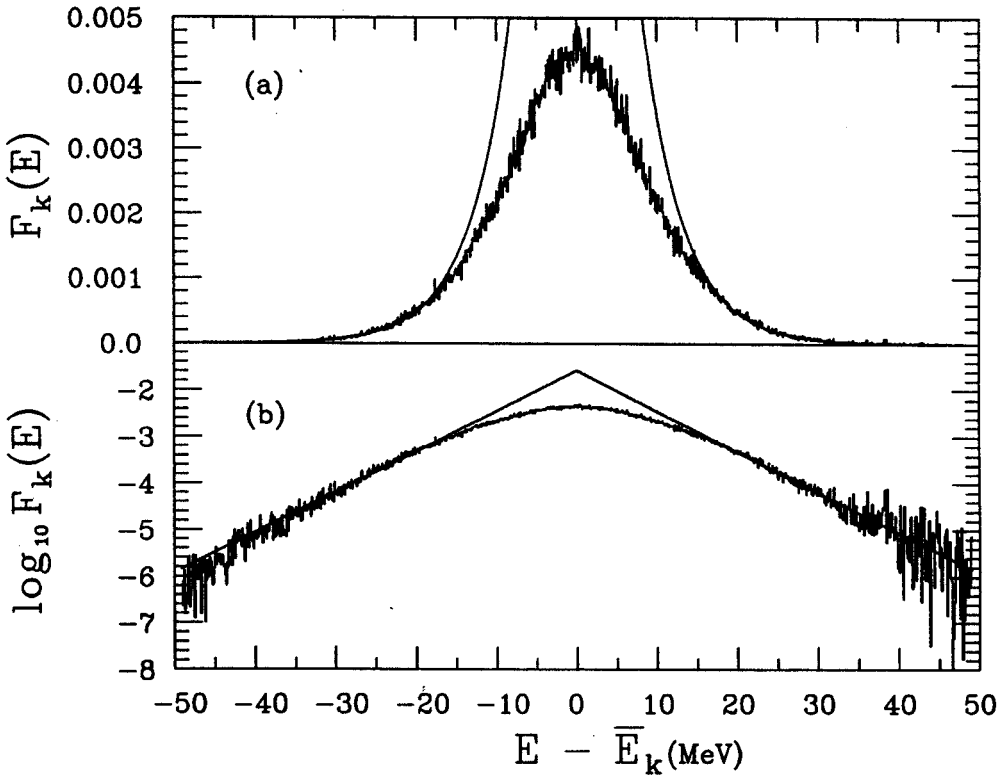

Figure 3.11: The exponential fit of eq.(3.28), solid lines, to the wings of the strength function of Fig. 3.5, *c* (histograms), panel *a*, and the same fit on the logarithmic scale, panel *b*. The bin size is 100 keV.

One could, in fact, construct a function that would be a weighted combination of an exponential and Breit-Wigner or Gaussian. The problem with this approach is

interpretation. It would not be possible to form an interpretation of any consistent nature with our present knowledge. The strength function falling off much faster than the Breit-Wigner distribution was also seen in a study of atomic levels [36] where it was difficult to establish the generic shape of the actual distribution because of the lack of statistics.

The exponential localization is the part of the folklore accompanying studies of complicated wave functions [37]. To the best of our knowledge, there is no general proof of this notion. The exponential localization of the wave functions in real space is known [38] in disordered solids. The situation in this case is different because the localized functions of nearly the same energy do not overlap if the distance between their centroids exceeds the spatial size of the wave function. In our case the exponential wings of the strength function coexist with the perfect chaotic level statistics.

3.3 Spreading Width

3.3.1 Two-Step Diagonalization and the Spectral Function

In order to observe the spreading widths of individual shell-model states, we performed the procedure of the two-step diagonalization described earlier (section 3.1.2) in relation to the standard model. Taking out an arbitrary basis state $|k\rangle$ and performing the diagonalization of the remaining matrix we obtain the intermediate basis $(|k\rangle, \{|\nu\rangle\})$ with energies $(\bar{E}_k, \{E_\nu\})$ and coupling matrix elements $V_{k\nu}$, eq.(3.17), between the single excluded state and intermediate fine structure states. As we discussed, in the realistic situation these matrix elements are correlated with the energy distance $\bar{E}_k - E_\nu$. To characterize the distribution function of the coupling matrix elements, we introduce, for each removed state $|k\rangle$, the spectral function (form-factor)

$$g_k(\bar{E}_k, \bar{E}_k + \omega) = \sum_\nu |V_{k\nu}|^2 \delta(\bar{E}_k - E_\nu + \omega). \tag{3.29}$$

This function can be presented by a histogram with the help of the density $\bar{\rho}_k(E_\nu)$ of the intermediate states available for the mixing with the single state $|k\rangle$. Introducing the average coupling intensity $\langle|V_{k\nu}|^2\rangle$, we get for the spectral form-factor (3.29)

$$g_k(\bar{E}_k, \bar{E}_k + \omega) \approx \bar{\rho}_k(\bar{E}_k + \omega)\langle|V_{k\nu}|^2\rangle. \tag{3.30}$$

According to (3.26), this function is normalized as

$$\int d\omega g_k(\bar{E}_k, \bar{E}_k + \omega) = \sigma_k^2. \tag{3.31}$$

The spectral form-factor $g_k(\bar{E}_k, \bar{E}_k + \omega)$ is shown in Fig. 3.12a for a single state $|k\rangle$ taken in the middle of the spectrum. It is concentrated around the unperturbed energy, $E_\nu \approx \bar{E}_k$. Using the same arguments of uniform complexity, we expect to be able to extract the "generic" spectral function $\bar{g}(\omega)$, depending on the transition frequency ω only, from the superposition of the form-factors g_k derived for different original states $|k\rangle$.

As the interval of averaging increases, the average form-factor rapidly evolves to the Gaussian shape. The form-factor averaged over 100 close states is shown in Fig. 3.12c. The Gaussian fit to the average distribution for 100 states is shown in figure 3.13a. The dispersion of the Gaussian is equal to $\sigma_g = 17$ MeV. The fitted normalization leads to the integral $\int d\omega \bar{g}(\omega) = 104$ MeV^2 which agrees, see eq.(3.31), with the average value of $\sigma_k \approx \bar{\sigma} \approx 10$ MeV.

Dividing out the level density of the intermediate basis states from the average form-factor (Fig. 3.13a), we determine the average coupling intensity (Fig. 3.13*b*), $\langle|V_{k\nu}|^2\rangle$, eq. (3.30). Except for the excess corresponding to the highest and, less pronounced, lowest states $|\nu\rangle$, the matrix elements are nearly constant on the level $\langle|V|^2\rangle \simeq 0.149(62)$ MeV^2.

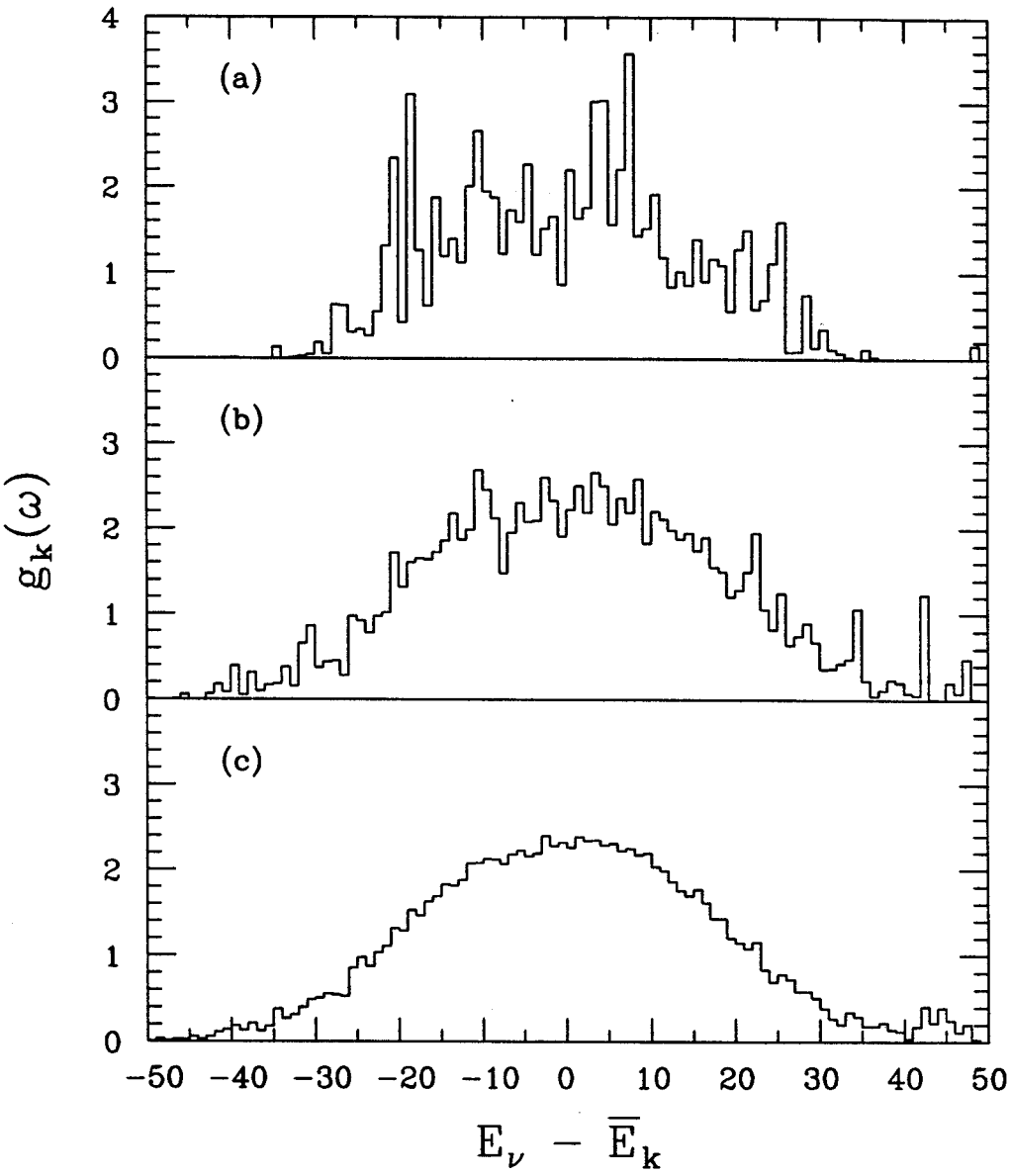

Figure 3.12: The spectral form-factor $g(\omega)$ for one state, panel *a*, and averaged over 10, and 100 0^+0 basis states in the middle of the spectrum, panels *b*, and *c* (histograms).

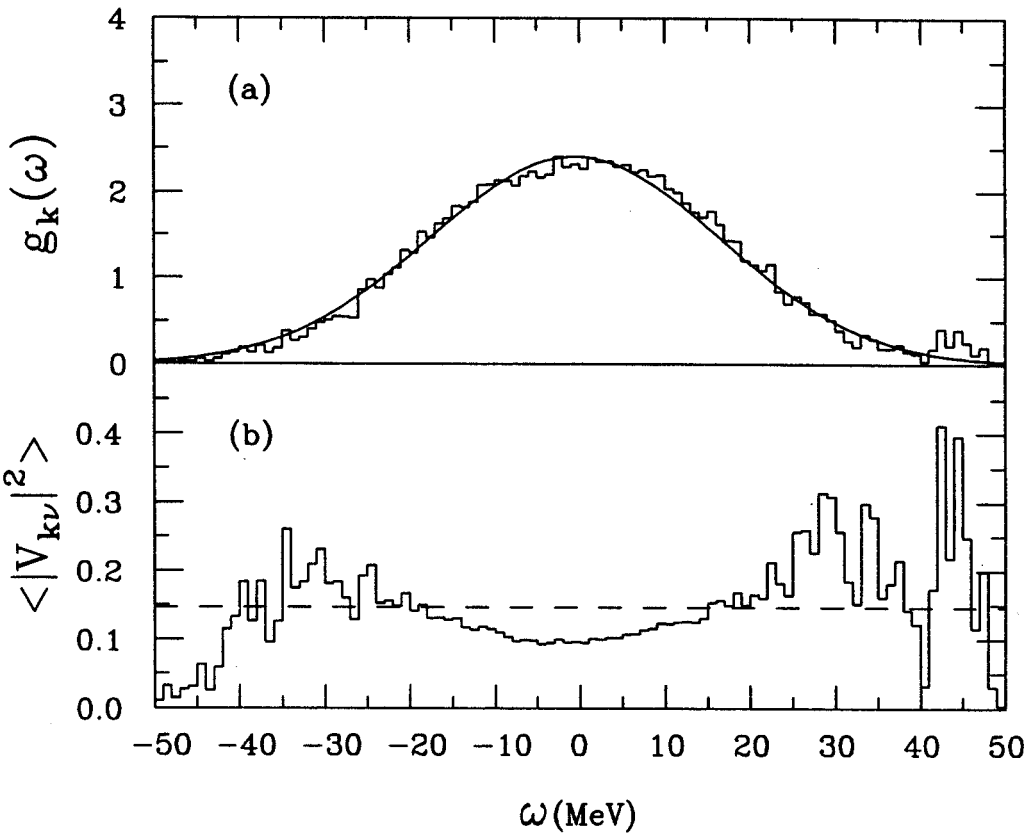

Figure 3.13: The spectral form-factor $g(\omega)$ over 100 0^+0 basis states in the middle of the spectrum, panel a, (histograms); with a Gaussian fit (solid line). The coupling intensity $\langle V^2_{k\nu}\rangle$ for the same basis states $|k\rangle$ in the middle of the spectrum (histogram), as a function of $\omega = E_\nu - \bar{E}_k$, panel b; dashes correspond to the constant value of $\langle V^2\rangle = 0.149$ MeV^2.

The value of the average coupling strength substituted into the golden rule, $\Gamma_s = 2\pi\frac{\langle V^2\rangle}{D}$, along with the average level spacing ~ 100 keV would result in the spreading width $\Gamma \approx 9.4$ MeV which is less than the value of 21 MeV found directly from the data by a factor 2.2. The evident disagreement demonstrates that the golden-rule estimate based on the standard model is not reliable when dealing with the fragmentation and spreading widths which are of the order or larger than the scale of the change of the level density. Taking a significantly larger level density in the center of the spectrum, $\rho(E) \simeq \frac{1}{D}$, with $D \approx 40$ keV instead of 100 keV, we would get the golden-rule width of 23 MeV, which is closer to the actual value.

This means that the realistic coupling is strong and involves remote parts of the spectrum with a different level density which mainly determine the shape of the form-factor. Recall that in our discussion of mixing and width σ_k, N-scaling was the scale by which we measured the extent of the mixing. That is, as the number N of fine structure states involved increases, each coupling matrix element diminishes, keeping the sum (3.8) constant. So, in agreement with the idea of N-scaling, the matrix elements are bigger and display stronger fluctuations near the edges where the states of lower complexity are located.

Finally, we show in Fig. 3.14 that, in the intermediate basis, the wings of the strength function $F_k(E)$ can be actually calculated by perturbation theory using in eq. (3.14) the weight coefficients

$$\langle (C_k^\alpha)^2 \rangle \to (C_k^\nu)^2 \equiv \Big(\frac{V_{k\nu}}{\bar{E}_k - E_\nu}\Big)^2. \tag{3.32}$$

The agreement with the original calculation in the peripheral regions is seen by coincidence of the two logarithmic plots in these regions (Fig. 3.15).

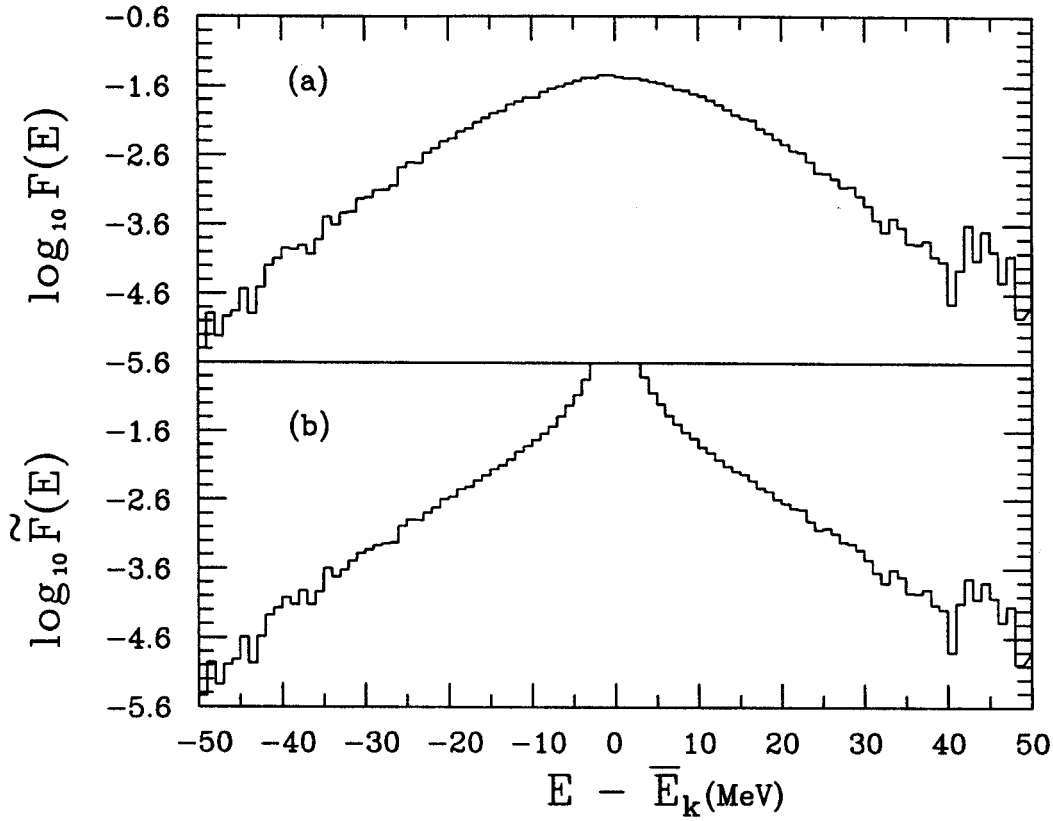

Figure 3.14: Strength function $F_k(E)$, panel *a*, and perturbative result $\tilde{F}_k(E)$, panel *b*, on a logarithmic scale. Bin size is 1 MeV.

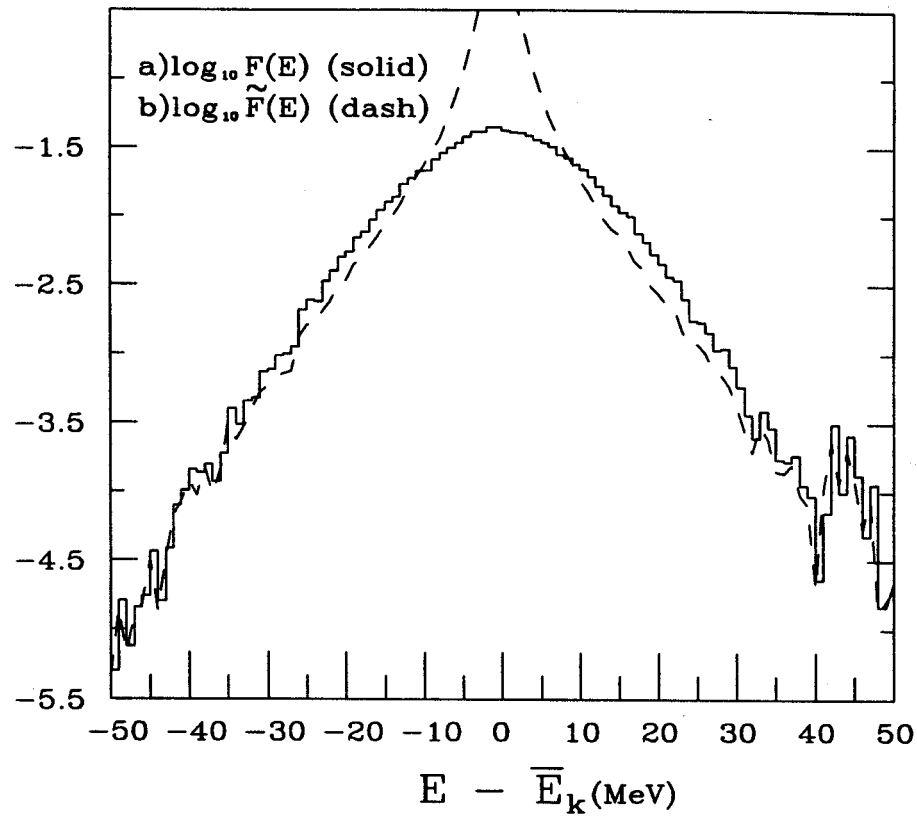

Figure 3.15: $F_k(E)$, 3.14a, and $\tilde{F}_k(E)$, 3.14b, on the same graph.

3.3.2 Dependence on the Interaction Strength

Here we study the evolution of the strength function and the spreading width as functions of the strength of the residual interaction λ. As we mentioned, the level statistics reveal standard signatures of quantum chaos already at $\lambda \approx 0.2$. The mixing of the wave functions, the growth of the degree of complexity and the evolution of the strength function are parallel aspects of the stochastization process.

In agreement with the general trends discussed in Sect. 3.3.2, at weak interaction strength the shape of the strength function becomes closer to the Breit-Wigner one. Figure 3.16 clearly shows the Breit-Wigner behavior for $\lambda = 0.1, 0.2$ and 0.3, panels 10a, 10*b* and 10c, respectively.

The whole evolution pattern is seen in the logarithmic plots of Fig. 3.17, a through *f*. The curve evolves in the direction of the Gaussian in the central part with exponential tails. The Breit-Wigner description of the main part of the strength function can be considered as satisfactory up to $\lambda \approx 0.4$. In this region the narrow strength function is not strongly influenced by the change of the level density. As seen from Fig. 3.18, the quality of the Gaussian fit clearly improves as one goes to the strong coupling limit; the last panel, 13*d*, corresponds to $\lambda = 1.2$.

Using "empirical" generic strength functions, we can trace the evolution of the spreading width (FWHM) as a function of the intensity of the residual interaction. Figure 3.19 shows the results for the values of λ between 0 and 1.2. The dependence of the spreading width on the interaction changes from quadratic for the weak coupling limit to linear for strong coupling.

At this point we limit ourselves with the simple interpolation formula for the

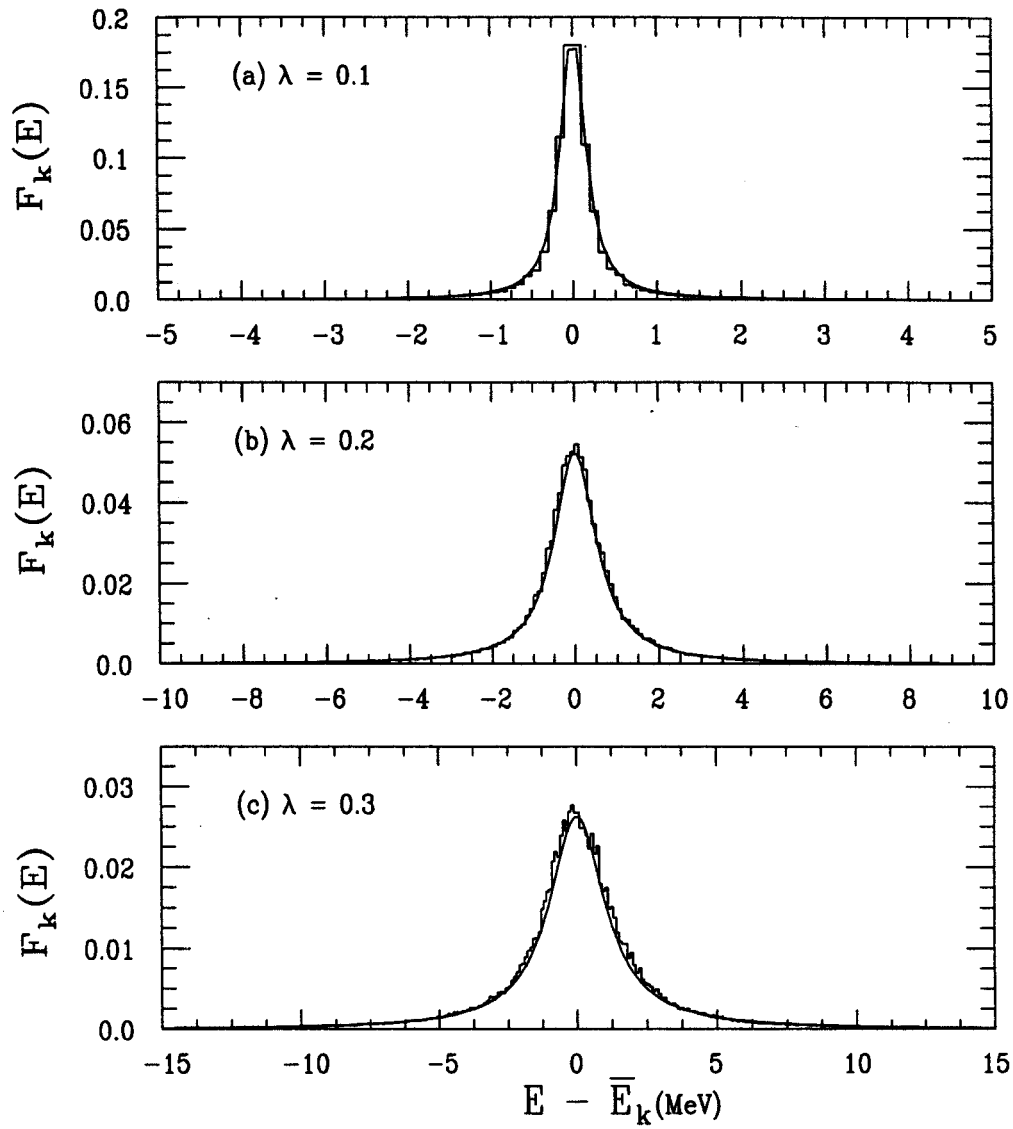

Figure 3.16: Breit-Wigner fit (solid lines) to the strength function averaged over 400 0^+0 mid-energy states for $\lambda = 0.1$, 0.2, and 0.3, panels *a*, *b*, and *c*, respectively. The bin size is 100 keV.

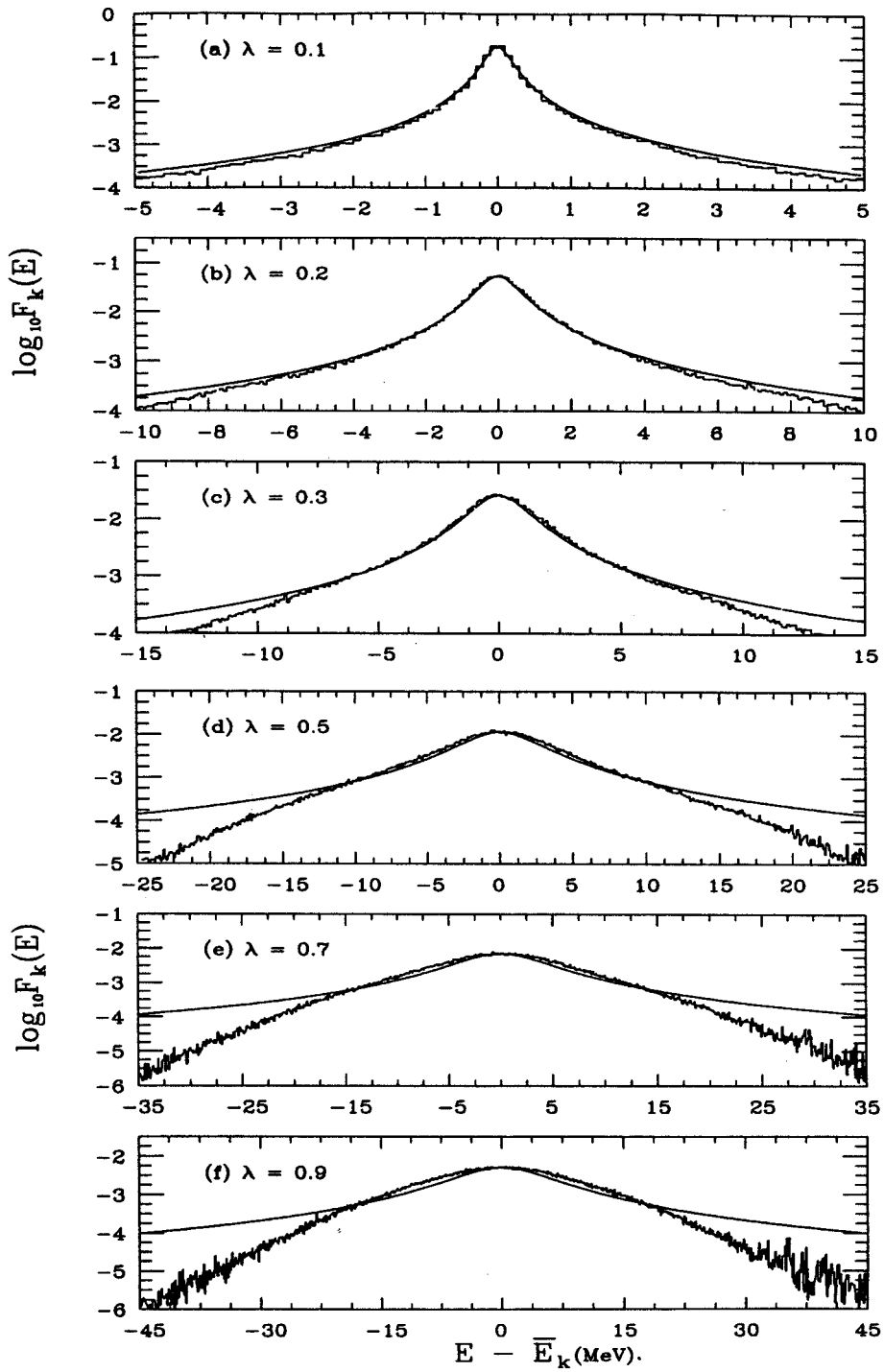

Figure 3.17: Breit-Wigner fit (solid lines) to the strength function averaged over 400 0^+0 mid-energy states for $\lambda = 0.1$, 0.2, and 0.3, panels *a*, *b*, and *c*, respectively, and $\lambda = 0.5$, 0.7 and 0.9, panels *d*, *e*, and *f*, respectively, on a logarithmic scale. The bin size is 100 keV.

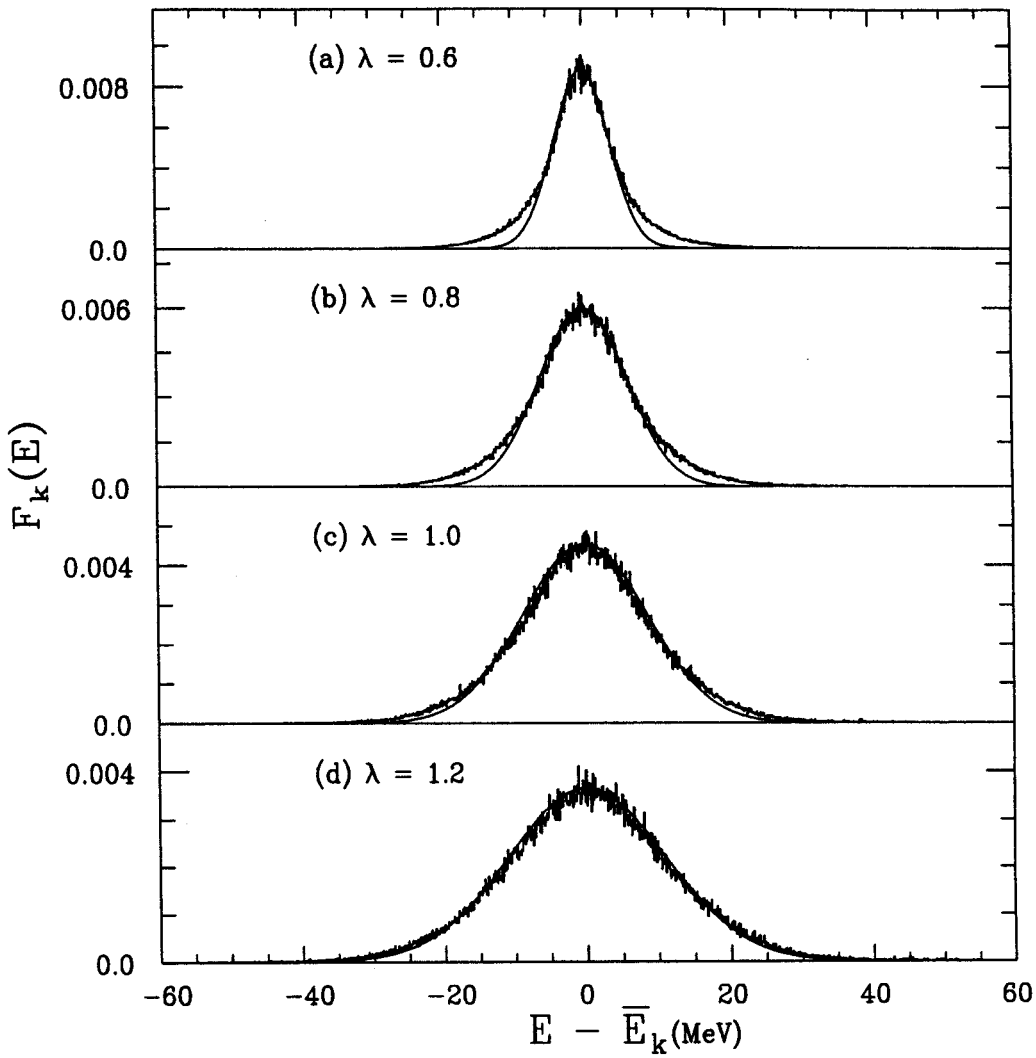

Figure 3.18: Gaussian fit to the strength function averaged over 400 0^+0 mid-energy states for $\lambda = 0.6$, 0.8, 1.0, and 1.2, panels *a*, *b*, *c* and *d*, respectively.

spreading width as a function of the strength of the residual interaction λ,

$$\Gamma = \frac{\gamma\lambda^2}{1+y\lambda}. \tag{3.33}$$

The parameters γ and y of eq.(3.33) are related to the weak and strong coupling limits. For the weak interaction case, the comparison of (3.25) and (3.33) determines

$$\gamma = \frac{2\pi}{D_0}\frac{\langle V^2(\lambda)\rangle}{\lambda^2} \tag{3.34}$$

where D_0 is the mean level spacing for the unperturbed system. The strong coupling limit determines, according to (3.27),

$$1+y = \frac{\gamma\lambda}{2\bar{\sigma}} \approx \frac{\pi\langle V^2\rangle}{D_0\bar{\sigma}} \tag{3.35}$$

where $\langle V^2\rangle$ and the mean value $\bar{\sigma}$ of the quantity (3.9) are taken at $\lambda = 1$ under the assumption that the actual value of the interaction strength belongs to the chaotic regime.

Our results are nicely described by the simple interpolation (3.33) with parameters $\gamma \approx 44.9$ MeV and $y \approx 1.32$. Our estimates (3.34) and (3.35), using the value of the average level spacing at weak interaction $D_0 \approx 21$ keV, predict for these parameters $\gamma = 44.6$ MeV and $y = 1.23$.

3.4 Summary

We conclude our analysis of basis state spreading widths by enumerating our findings. Our primary goal was to describe the shape of the distributions as a function of excitation energy. We also calculated the widths of these distributions as a function of interaction strength.

Our main points relating to basis-state strength functions, as far as the shape of the "average" distribution is concerned, are as follows:

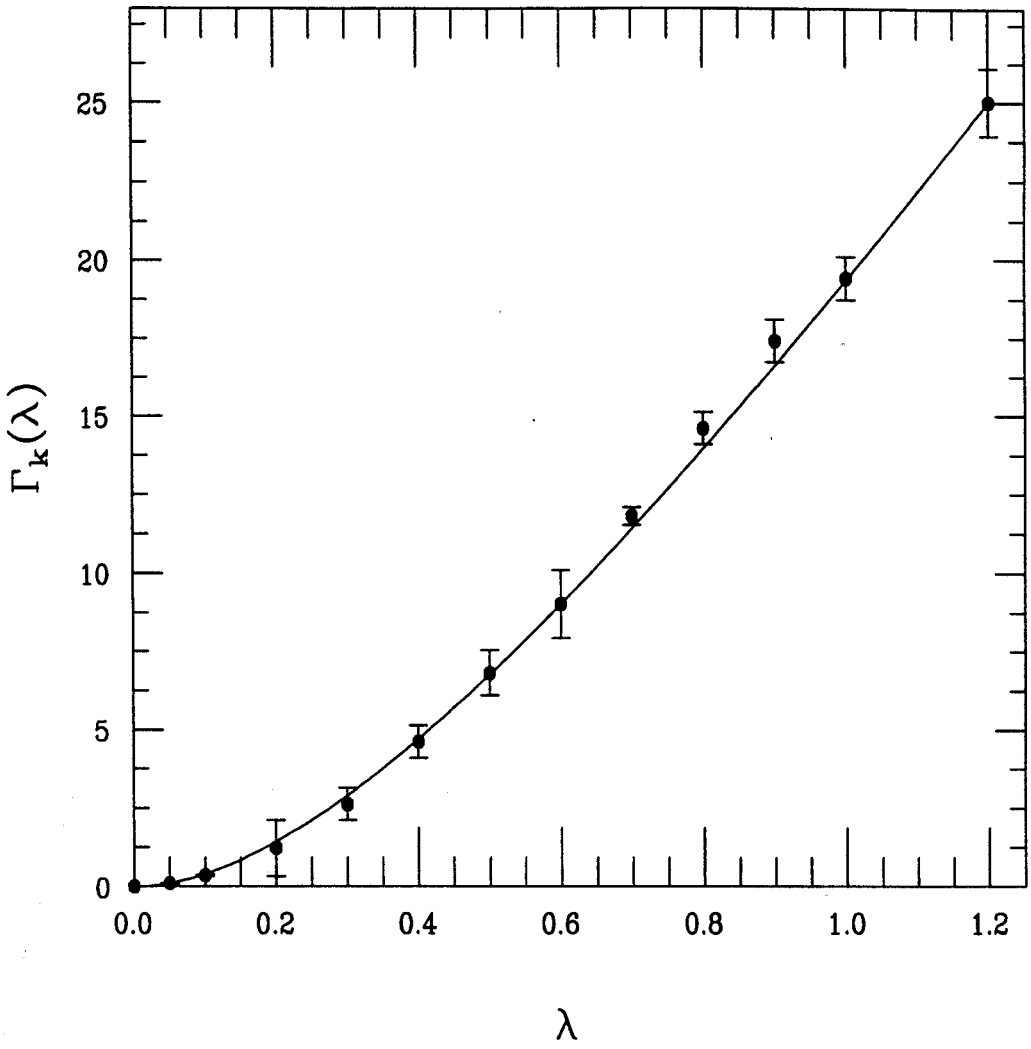

Figure 3.19: Spreading width Γ_k of the basis states as a function of the interaction strength λ for 400 middle 0^+0 states. The solid line corresponds to eq.(3.33) with $\gamma = 44.9$ MeV and $y = 1.32$. The error bars are defined by the deviations of the fit from the calculated data.

1. An overall Gaussian fit, Fig. 3.7*a*, is consistent with the central region of the strength function.

2. The variance obtained from the Gaussian fit is $\sigma_{basis} = 8.3 \pm 0.3$ MeV giving a spreading width (FWHM) of the central 0^+0 states equal to $\Gamma_{basis} = \sqrt{(8 \ln 2)}\, \sigma_{basis} = 19.6$ MeV. This width agrees with the estimate (3.27), $\Gamma_{SC} = 2\bar{\sigma} = 20$ MeV made for the strong coupling limit. It is clear that the Breit-Wigner shape predicted by the standard model of the strength function does not hold in the realm of strong coupling.

3. The central part of the distribution is successfully fit with a Gaussian, but we observe deviations from the Gaussian shape in the tails (Fig. 3.7*b*) of the strength function. Figure 3.11 shows that the wings can be described by an exponential fit $F_k(E - \bar{E}_k) \approx F_0 \exp\left(-\frac{E-\bar{E}_k}{E_l}\right)$. The exponential tails of the strength function $F_k(E)$ can be reproduced by perturbation theory.

Next, our results pertaining to the interaction strength.

1. The quadratic dependence of the spreading width on the interaction strength is replaced by the linear dependence as we go from weak to strong coupling, or as λ goes from $0 \rightarrow 1$.

2. Just as we can artificially suppress the interaction to retrieve the standard golden rule, we can enhance the interaction. By setting $\lambda = 1.2$ we see the continuation of the linear trend. We also see that the Gaussian level density determines the shape of the strength function distribution, even for the wings which were formerly described by an exponential curve (Fig. 3.18).

Chapter 4

Spectroscopic Factors

4.1 Introduction

As a bridge from calculations of the basis-state strength functions (ch. 3) to calculations of Gamow-Teller strength functions (ch. 5) we examine the spectroscopic factor, S_j. In this section we carry out calculations for the transitions from the $J^\pi T = 0^+0$ initial states of 8 particles above the inert core of ^{16}O to the $J^\pi T = \frac{1}{2}^+\frac{1}{2}$ final states of 9 particles above the inert core of ^{16}O (see table B.3). The system can be considered as a model for the transfer reaction leading to the transition from the ^{24}Mg nucleus to the ^{25}Mg or ^{25}Al nucleus. We look closely at the width of the distribution, both for insight into excited-state single-nucleon transfer and in relation to the widths for basis-state strength functions and Gamow-Teller strength functions.

In single-nucleon transfer reactions, the projectile either gains (pickup) or loses (stripping) a single nucleon as a consequence of interaction with the target nucleus. This process has three integral steps:

(i) the projectile moves in an average field of the *target* nucleus,

(ii) a nucleon is transferred from the projectile to an orbit in the target,

(iii) the outgoing particle proceeds in the average field of the *final* nucleus.

The final state of the residual nucleus is formed from the addition of the transferred

nucleon to the initial state of the target. From stage (ii) we garner information about the structure of the nuclear states of the final nucleus.

Strong excitations in stripping reactions indicate a state in the projectile nucleus with dominant single-particle features. The nucleon is tightly bound to projectile nucleus and has to be highly excited to remove a nucleon from the highest filled single-particle orbit. In pickup reactions, dominant single-particle features of the target mean a state in the projectile nucleus that is strongly coupled to the loosely bound target nucleon it picks up. The nuclear matrix elements of these transfer reactions are commonly expressed in terms of the spectroscopic factor S_j,

$$S_j = \frac{1}{2J_f + 1} |\langle f | a^\dagger_{j,t} | i \rangle|^2. \tag{4.1}$$

Single-nucleon transfer has a definite spreading width determined by the overlap between the initial and final nuclei, denoted by the Coefficient of Fractional Parentage (CFP) $\langle f | a^\dagger_{j,t} | i \rangle$. In terms of the reduced matrix elements of the creation operator $a^\dagger$, we can express the amplitude θ_j as

$$\theta_j(J_i, J_f) = \frac{\langle f, J_f \| a^\dagger_{j,t} \| i, J_i \rangle}{\sqrt{2J_f + 1}}. \tag{4.2}$$

Since $a^\dagger_{j,t}|i\rangle$ is overlapped with $\langle f|$, we can view the raising operator as a filter between the initial and final eigenstates. The initial and final states considered in the one-nucleon transfer are both eigenstates of their respective nuclei. In dealing with single-nucleon transfer, we are not looking at how the basis states are spread over eigenstates as in chapter 3, we are instead looking at how the state $|\zeta\rangle = a^\dagger_{j,t}|i\rangle$ is spread over the eigenstates. This being the case, it is plausible that the spreading width for single-nucleon transfer will be smaller than that for basis states. The simplicity of the one-body raising operator implies that the excitation caused by $a^\dagger_{j,t}$

will not appreciably change the original eigenstate wavefunction $|i\rangle$, which already contains the full dynamics of A_v particles.

Our calculations involve only the creation of a single particle in the $s\frac{1}{2}$ orbital. Single-nucleon transfer transition is from $J_i^\pi T_i = 0^+0$ to $J_f^\pi T_f = \frac{1}{2}^+\frac{1}{2}$ for all shell-model eigenstates in the $0d - 1s$ shell model space. The 0^+0 class contains $N = 325$ states and the $\frac{1}{2}^+\frac{1}{2}$ class contains $N = 1434$ states (see table B.3) partitioned into the shell model configurations according to the occupation numbers of the three active spherical orbits in the *sd*-shell.

4.2 Spreading Widths

As with the fragmentation of shell-model basis states, and later with Gamow-Teller strength distributions, the width of the distribution gives us insight into the role of the residual interaction. In cases of strong coupling this is especially important as a means of determining the extent of stochastization and chaos in high-lying levels.

Figure 4.1 shows the ground state distribution for the $A \rightarrow (A+1)$ single-nucleon transfer. It is centered on the mean value of the difference $(E_f^* - E_i^*)$ between the initial $A = 24$ and final $A = 25$ nuclei. When compared to the experimental result of figure 4.2, we see the agreement between the theoretical and experimental distributions for the ground state and first excited state.

In figure 4.3, we see the distribution of strengths of the spectroscopic factors for the excited levels. Panels a - c of figure 4.3 show the distributions summed over the ground and excited $J^\pi T = 0^+0$ states $1 - 100$, $101 - 200$, and $201 - 325$ respectively. From the distributions we see that the amplitude is fairly constant in all three energy sectors. There is also a relatively small change in the width from 4.3a to 4.3c. This is consistent with a conclusion that the transition strengths depend on the relative

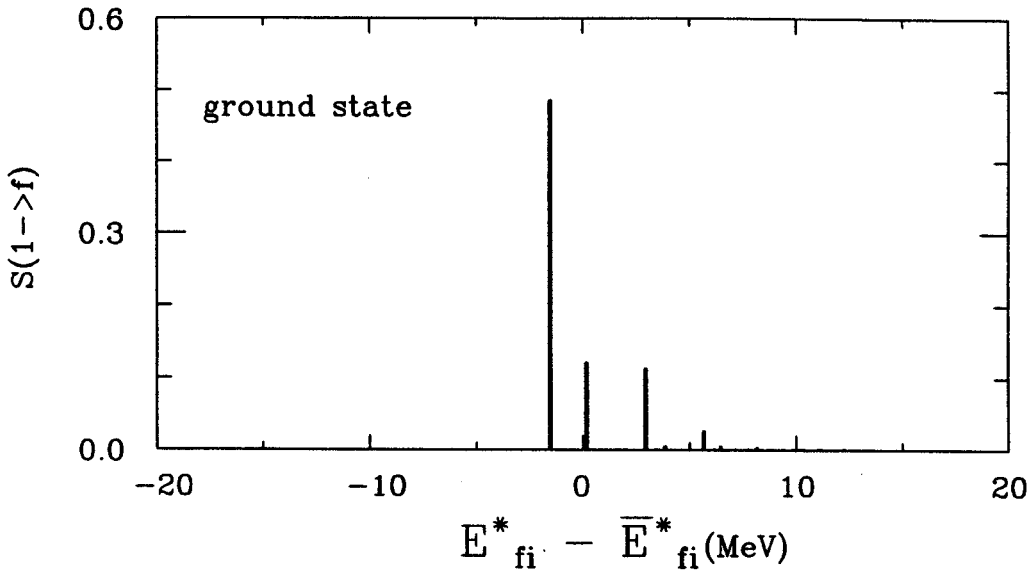

Figure 4.1: The calculated spectroscopic strength functions for $A = 24 \rightarrow A = 25$ plotted as a function of difference in excitation energy $(E^*_{f1} - \overline{E^*_{f1}})$ between the ground state of the initial nucleus and all states of the final nucleus. Energy in MeV.

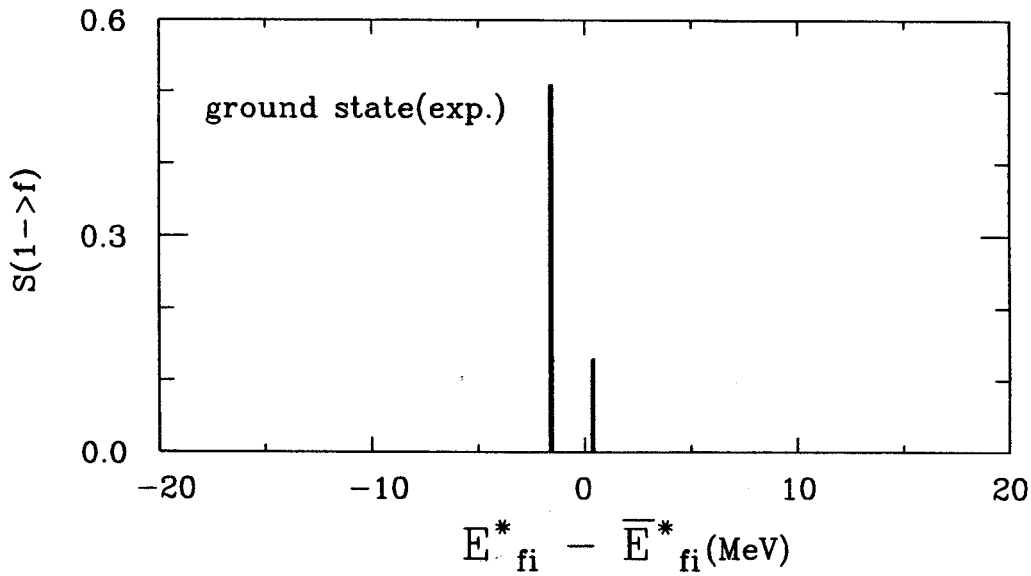

Figure 4.2: The experimental [39] spectroscopic strength for $A = 24 \rightarrow A = 25$ plotted as a function of excitation energy E^*_{f1}. Energy in MeV.

energy between the initial and final state energy levels (E^*_{fi}), but not on the specific level from which the nucleon transfer occurs.

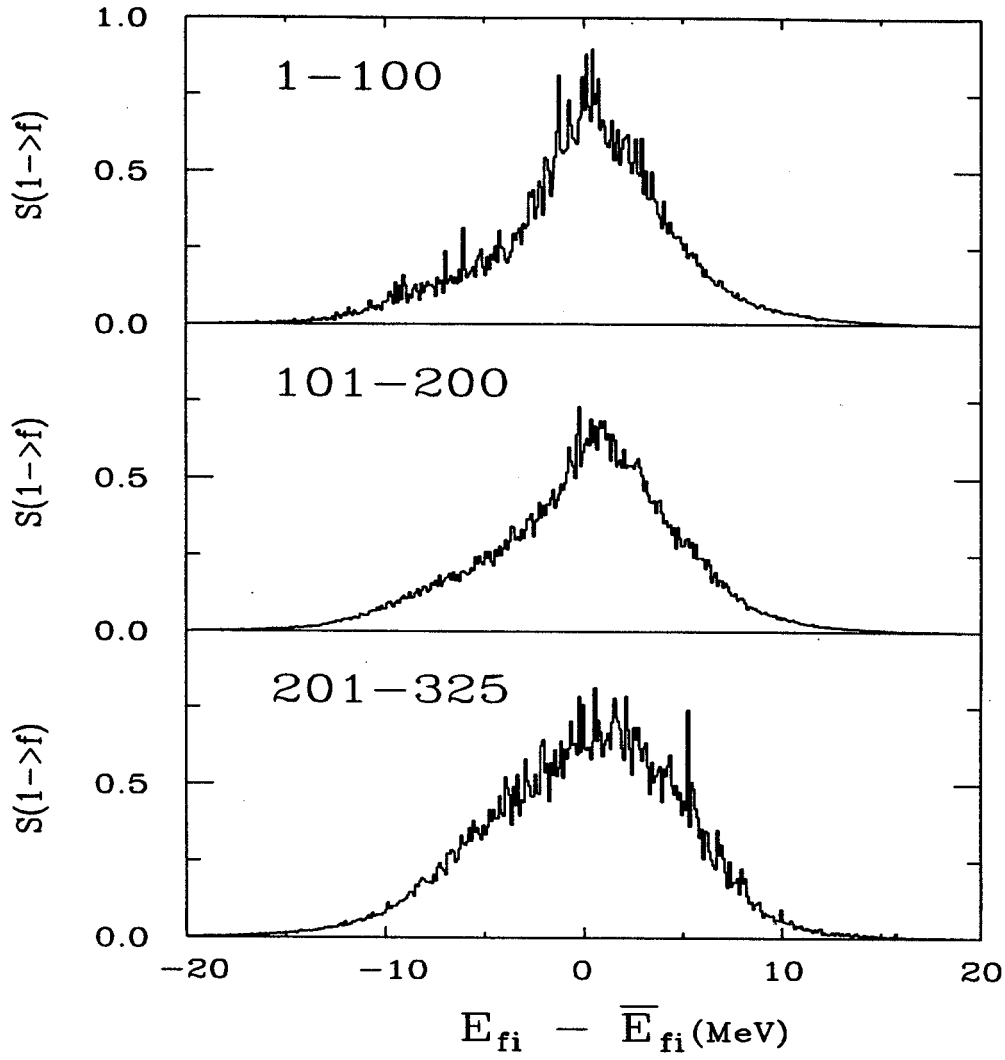

Figure 4.3: The spectroscopic strength functions for $A = 24 \rightarrow A = 25$ plotted as a function of difference in excitation energy ($E^*_{fi} - \overline{E^*_{fi}}$) between the initial and final nucleus for states 1-100, panel (a),101-200, panel (b), and 201-325, panel (c). Energy in 100 KeV.

There is an obvious low-energy tail for the $i = 101 - 200$ distribution. To fit this distribution we make a cut that doesn't weight the low end of the distribution. By doing this, we get a more accurate fit (fig. 4.4) to the central portion of the spec-

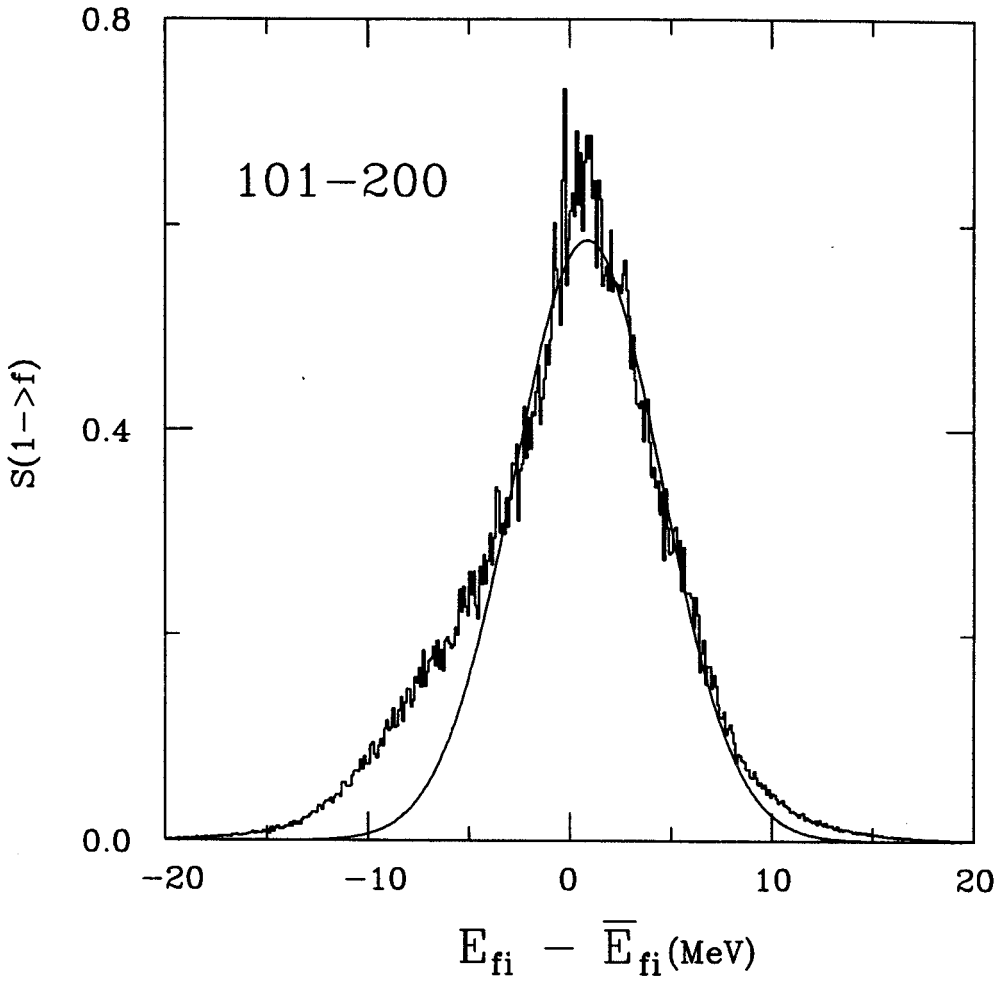

Figure 4.4: Gaussian fit to the spectroscopic strength function distribution for a superposition of 100 mid-energy states excluding the low-lying tail. Energy in MeV.

troscopic strength function. This cut gives a Full Width at Half-Maximum (FWHM) value of $\tilde{\Gamma}_{at} = 8.55(34)$ MeV. The error here is that given from a χ^2 fit to the data after the cut. At this point, the low-energy tail is not fully understood. The width for the middle set of spectroscopic amplitudes (fig. 4.5) is $\Gamma_{at} = 8.73(76)$ MeV without the low-energy cut. The width for this distribution is less than half the width seen for the basis state distributions of section 3.2.2.

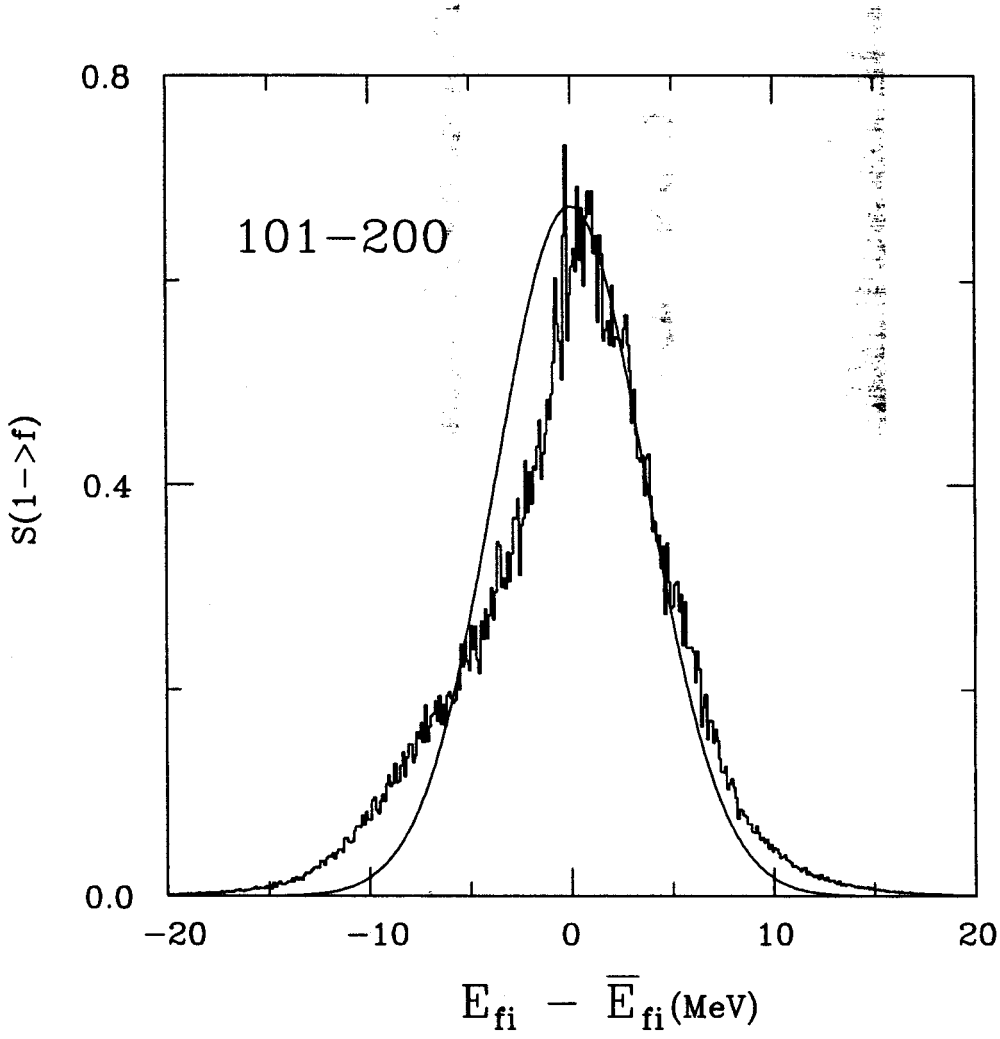

Figure 4.5: Gaussian fit to the spectroscopic strength function distribution for a superposition of 100 mid-energy states. Energy in MeV.

4.3 Summary

We will now conclude our analysis of spectroscopic spreading widths. Our primary goal was to describe the shape of the average distributions as a function of excitation energy. We also calculated the widths of these distributions in order to observe the width relative to basis-state strength functions and, later, Gamow-Teller strength functions. So, for spectroscopic factors, we conclude by saying

1. The width of the set of spectroscopic amplitudes corresponding to the middle 100 states is $\Gamma_{at} = 8.73(76)$ MeV. A better fit to the curve is obtained if we fit the mid-to high-lying region of the spectrum using a Gaussian curve. The FWHM is then $\tilde{\Gamma}_{at} = 8.47(25)$ MeV.

2. Both the Gaussian shape and the decrease in width relative to basis state strength functions, $\Gamma_{basis} = 20$ MeV to $\Gamma_{at} = 8.7$ MeV are reasonable results.

   (a) The Gaussian character of the distribution follows from the fact that we are again in the region of strong mixing.

   (b) The final state wavefunctions are interpreted as being closer to initial-state wavefunctions that have been acted on by a simple operator, than basis states are to these shell-model eigenstates. These eigenstate wavefunctions already include effects of the strong interaction between A_v particles.

Chapter 5

Gamow-Teller Transitions

5.1 Introduction

Gamow-Teller (GT) transitions represent a typical one-body process in which one nucleon is destroyed and another is created. It is distinguished from another class of weak transitions, the Fermi (F) transitions, by the fact that GT decays involve the transfer of one unit of spin angular momentum S. GT matrix elements are important in that they give us information about the coupling of the nucleon spins, and spin-dependent effects of weak interactions.

The Gamow-Teller operator is defined as a sum over nucleons (j)

$$O_{\mu\,GT}(\pm) = \sum_j \sigma_{\mu,j}\tau_{\pm,j} \tag{5.1}$$

The Gamow-Teller strength function is obtained by calculating the matrix element squared for the $\langle f\,|\sigma\tau|i\,\rangle$ transition,

$$B_{GT}(\pm; i \rightarrow f) = \sum_\mu |\langle f;\, J_f^\pi T_f|O_{\mu\,GT}|i;\, J_i^\pi T_i\rangle|^2 \tag{5.2}$$

between the eigenstates of the initial $|i;\, J_i^\pi T_i\rangle$ and final $\langle f;\, J_f^\pi T_f|$ nuclei. Fermi transitions can be described in a similar form by

$$B_F(\pm; i \rightarrow f) = |\langle f;\, J_f^\pi T_f|\sum_j \tau_{\pm,j}|i;\, J_i^\pi T_i\rangle|^2. \tag{5.3}$$

The GT operator changes both the intrinsic spin, S, of the nucleus and the isospin T. S is altered by the $\vec{\sigma}$ operator, constructed from the Pauli spin matricies, $(\sigma_x, \sigma_y, \sigma_z)$, and related to the $\vec{s}$ operator by $\vec{s} = \frac{\vec{\sigma}}{2}$. T is altered by the $\vec{\tau}$ operator,

$$\vec{\tau} = \sum_{j=1}^{A} \vec{\tau}_j. \tag{5.4}$$

In nuclear physics we deal primarily with neutron rich nuclei. For this reason τ_+ acting on a proton will produce a neutron. In general, our single-particle isospin operators act in the following manner:

$$\tau_+|p\rangle = |n\rangle \qquad \tau_+|n\rangle = 0$$
$$\tau_-|p\rangle = 0 \qquad \tau_-|n\rangle = |p\rangle.$$

Using the Wildenthal hamiltonian, we construct the realistic wavefunctions and use them to calculate the amplitudes for Gamow-Teller transitions. I will be examining the transitions from $J_i^\pi T_i = 0^+0$ to $J_f^\pi T_f = 1^+1$ for all initial eigenstates in the $0d - 1s$ shell-model space, where J, π, and T are good total angular momentum, parity, and isospin quantum numbers. In addition to the transfer of a unit of spin angular momentum ($\Delta S = 1$), single-particle GT transitions have the following selection rules:

$\Delta l = 0$

$\Delta j = 0, 1$ $\qquad J_i = 0 \rightarrow J_f = 0$ transitions forbidden

$\Delta t = 0, 1$ $\qquad T_i = 0 \rightarrow T_f = 0$ transitions forbidden

$\Delta \pi = 0$

β^--decay and (n,p) charge-exchange reactions are transitions that we associate with $O_{GT}(-)$

$$n \longrightarrow p + e^- + \overline{\nu_e}.$$

One can also have a β^+ or (p,n) reaction, which along with the (p,p') reaction, fall under the heading of Fermi or Gamow-Teller transitions. In the case of a (p,n) reaction, a nucleus A is bombarded with a beams of protons. A proton is absorbed by the nucleus A and a neutron is emitted in the exchange.

$$A(Z,N) + p \longrightarrow A'(Z+1, N-1) + n + e^+ + \nu_e.$$

As shown in the examples above, GT transitions emit leptons. These leptons have parallel spins which sum to $S = 1$. A level diagram for the initial $J_i^\pi T_i = 0^+0$ states and the final $J_f^\pi T_f = 1^+1$ states for all shell-model eigenstates can be seen in figure 5.1.

Although we have a full range of theoretical $B(GT)$ values, the experimental values for $B(GT)$ are limited in a number of ways. First and foremost, we know that excited states are too short lived to be seen experimentally. Therefore, the experimental strength values can be obtained for the ground state only. Added to that are the energetic limitations. Decay is allowed only if the initial state is higher in energy than the final state. The experimental sum for the ground state only includes those final states which lie within the Q value window.

In shell-model calculations, a proton or neutron in a nucleus of definite angular momentum, spin, and parity is destroyed and another nucleon is created in keeping with the rules of charge, space, spin, and isospin conservation rules for GT transitions. Our primary objective is to look at the behavior of the total Gamow-Teller strength as a function of excitation energy. We calculate the Gamow-Teller transitions for the system of 8 valence particles within the *sd*-shell or ^{24}Mg. This is the initial nucleus from which we will have either (p,n) or (n,p) reactions, corresponding to the $O_{GT}(+)$

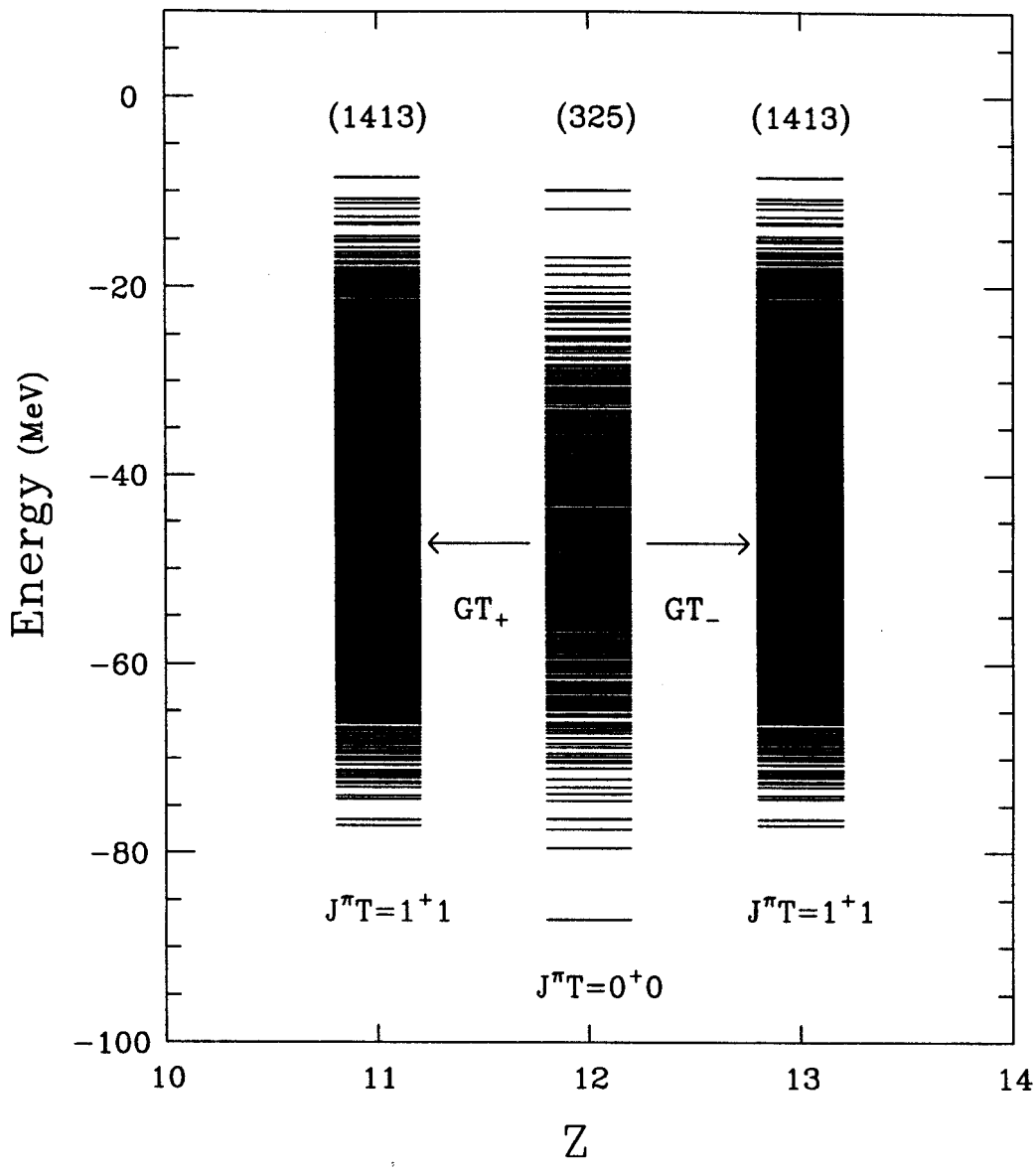

Figure 5.1: Energy spectra for the $J^\pi T = 0^+0$ states of the initial ^{24}Mg nucleus and the $J^\pi T = 1^+1$ states of the final ^{24}Na and ^{24}Al nuclei. Plotted as energy versus proton number, Z.

or $O_{GT}(-)$ operator respectively. We will also examine the effect of the coherence induced by the residual interaction. Finally, we will determine the contribution to the total strength from each orbital in the active model space.

5.2 Gamow-Teller Strength Distribution

Before we address the total strength, we take a closer look at the fragmented strength function distribution,

$$B_{GT}(\pm; i \rightarrow f) = \sum_{\mu} |\langle f;\ 1^+1| \sum_{j} \sigma_{\mu}\tau_{\pm}|i;\ 0^+0\rangle|^2. \tag{5.5}$$

Because of the strong fragmentation that occurs, we obtain a distribution whose characteristics will give us insight into beta decay ($\beta^{\pm}$) and charge exchange reactions at high temperatures. If a reaction occurs that changes the charge state, (p,n), (π^+,π^o), or (π^o,π^-), but does not excite the nucleon to a different single-particle orbit, then the final state can be described as the isobaric analogue state (IAS) of the initial target state. Members of an isobar have the same A but different N and Z. Isobaric analogue states are states in a neighboring nucleus that are related by a rotation in the isospin space. Although they belong to different nuclei, they are members of the same isobaric multiplet and as such they have similar properties. When one discusses isobaric analogue resonances they are referring to the sharp peak, or resonance, located at an energy which corresponds to the difference in binding energy for the two nuclei, mainly due to the coulomb interaction.

5.2.1 Nucleon-Nucleon Interaction

The N-N interaction strongly mixes the L and S components of angular momentum. This means that instead of a GT transition going from one initial state to one final GT analog state, as it would if the intrinsic spin was conserved, the GT strength,

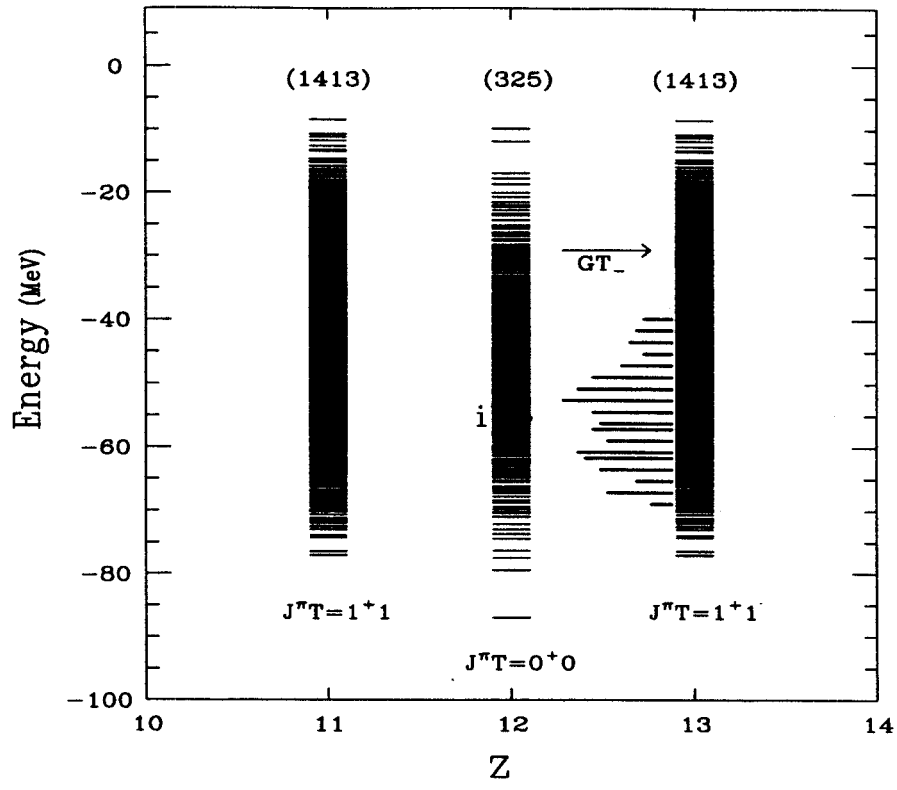

Figure 5.2: Schematic showing the fragmentation over final states for the Gamow-Teller transition from an arbitrary state $|i;0^+0\rangle$ to all possible final states $|f;1^+1\rangle$. Plotted as energy versus proton number, Z for the $J^\pi T = 0^+0$ states of the initial ^{24}Mg nucleus and the $J^\pi T = 1^+1$ states of the possible final ^{24}Na and ^{24}Al nuclei.

$B(GT)$, is strongly split amongst many states. In fact the GT strength is related to the spin-isospin term of the NN-interaction (2.2). With the inclusion of the SO interaction, only J, π, and T are invariant. A schematic view of the $B(GT)$ strength fragmentation is shown in figure 5.2.

5.2.2 Spreading Width

This strength distribution is interesting because its width is related to the chaoticity of the wavefunctions involved in the GT transitions. The widths can also be compared to the results for the fragmentation of shell-model basis states (section 3.2) and the fragmentation induced by the raising operator (section 4.2).

With the previous arguments for the spreading width of the spectroscopic factor, finding a width for the GT strength distribution Γ_{GT} in the same system consistent with that of spectroscopic strength functions would be understandable. The overlap between the final and initial state such that $[a^\dagger(j) \otimes \tilde{a}(j')]$ acting on the initial states is very similar to the overlap that occurs for the $[a^\dagger(j)]$ operator acting on the initial states. In fact, following the reasoning for the spreading width of single-nucleon transfer, we might expect a slightly larger width. This is because $[a^\dagger(j) \otimes \tilde{a}(j')]$ is a more complex operator than $[a^\dagger(j)]$ and therefore able to alter the initial eigenstate to a larger degree.

As in chapter 2, the distributions have been superimposed to reduce the statistical fluctuations and get an idea of the general shape of the distribution. We notice right away that the distribution for the first 100 states is asymmetric (see figure 5.3a). We will address the issue of the asymmetry in this distribution in a later section. Oddly enough, the effects due to our finite Hilbert space that one would expect to contribute to this asymmetry does not affect the top 100 states to the same extent (Fig. 5.3*b*). For the superposition of all states (Fig. 5.4) the high-energy tail is still evident.

To continue with our analysis of spreading widths, we must remain consistent in our sampling of the states in the mid-energy, high-density region. For this reason, we superimpose states 101 through 200. Figure 5.5 shows a Gaussian fit to the central part of the distribution. Again we see the high energy tail reminiscent of the basis state and single-nucleon transfer distributions of chapter 3. The width of this distribution is $\Gamma_{GT} = 9.5(6)$ MeV.

If we further separate the regions and look at bins of 10 initial states spread over all final states, we see a definite trend. Figure 5.6 shows that the widths clearly decrease with increasing excitation energy. The widths of the distributions range

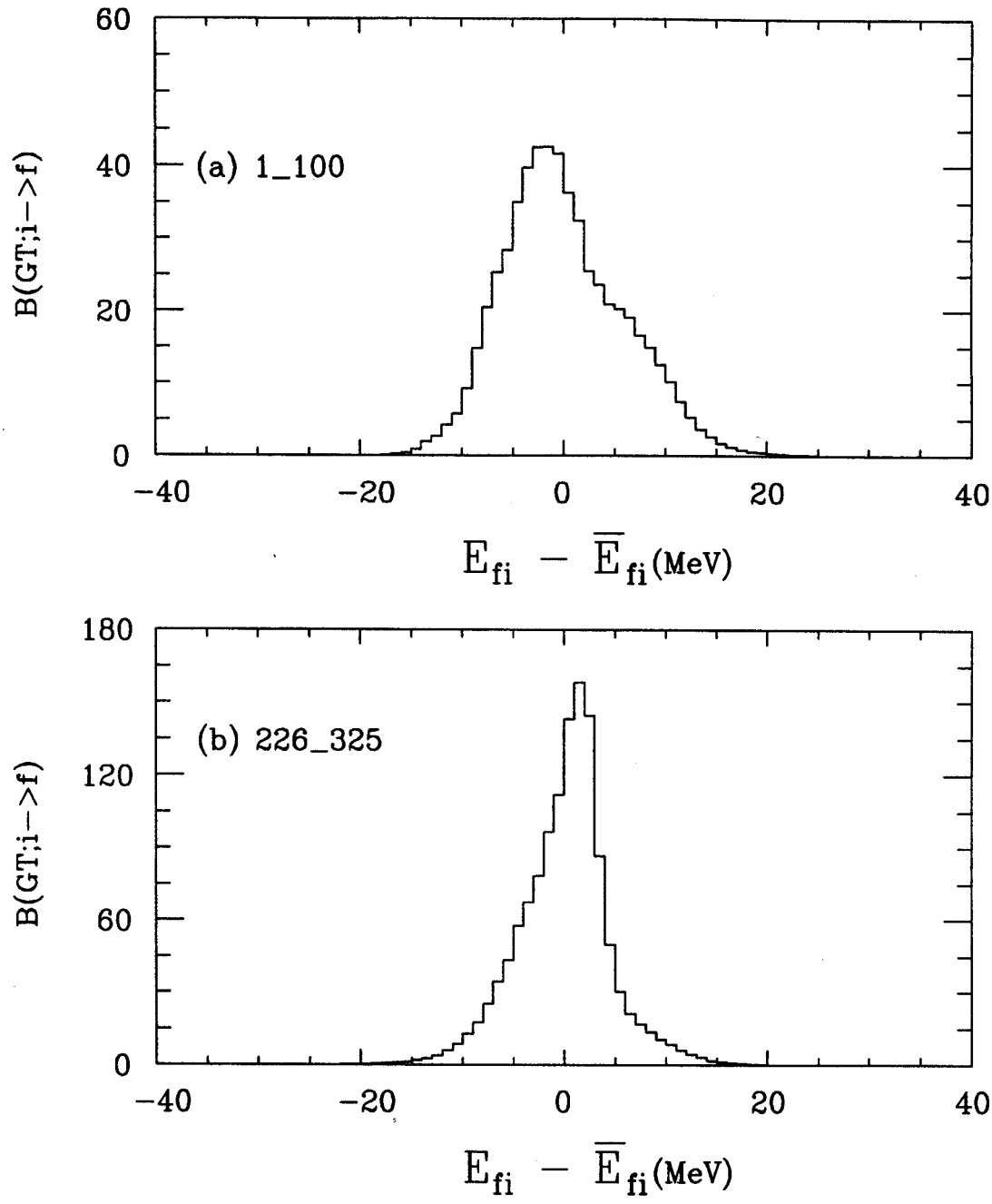

Figure 5.3: Superposition of Gamow-Teller strength functions, $B(GT; i \rightarrow f)$, for the first 100 (panel a) and last 100 (panel b)states plotted as a function of ΔE_{fi}.

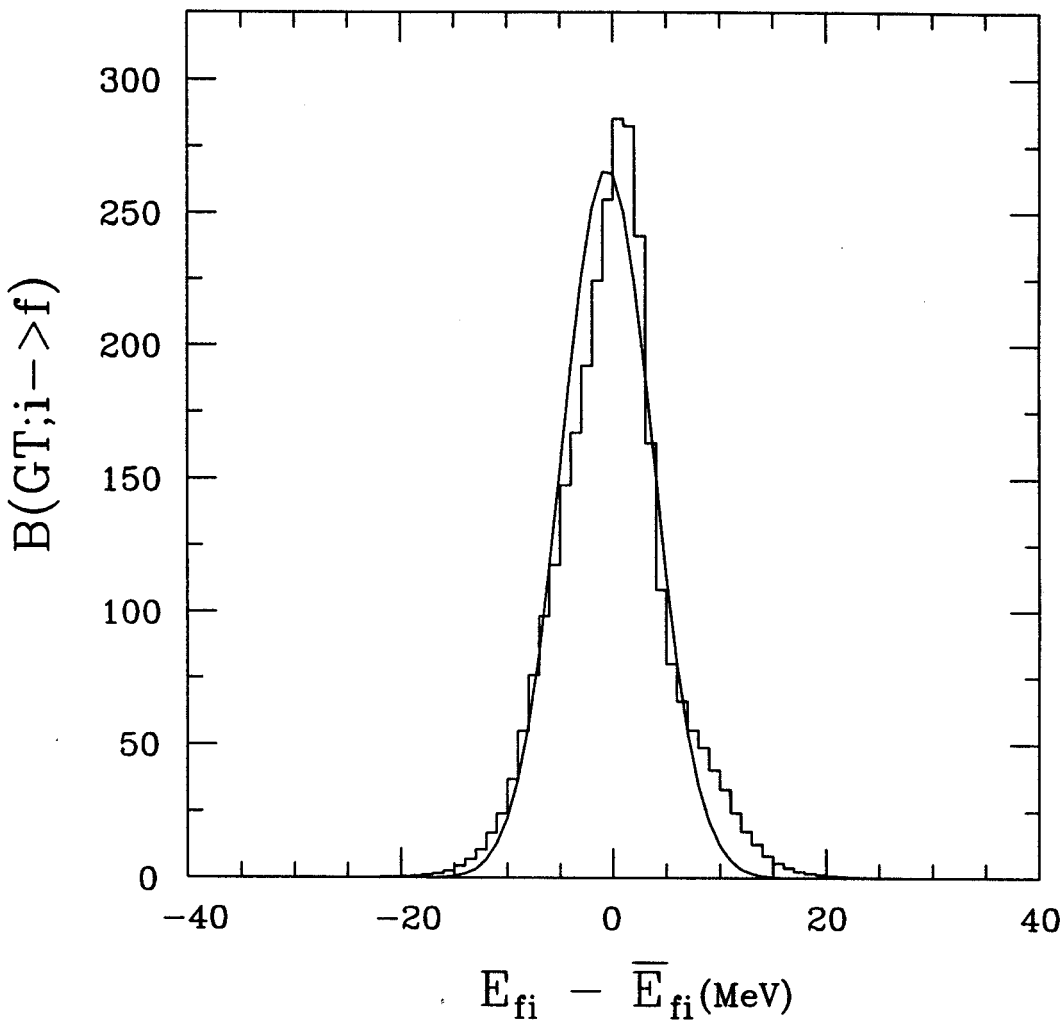

Figure 5.4: Gaussian fit (solid line) to the Gamow-Teller strength function, $B(GT; i \rightarrow f)$, for ^{24}Mg plotted as a function of ΔE, between the all 325 initial ^{24}Mg ($J^{\pi}T = 0^{+}0$) and all 1413 final ^{24}Na ($J^{\pi}T = 1^{+}1$) states.

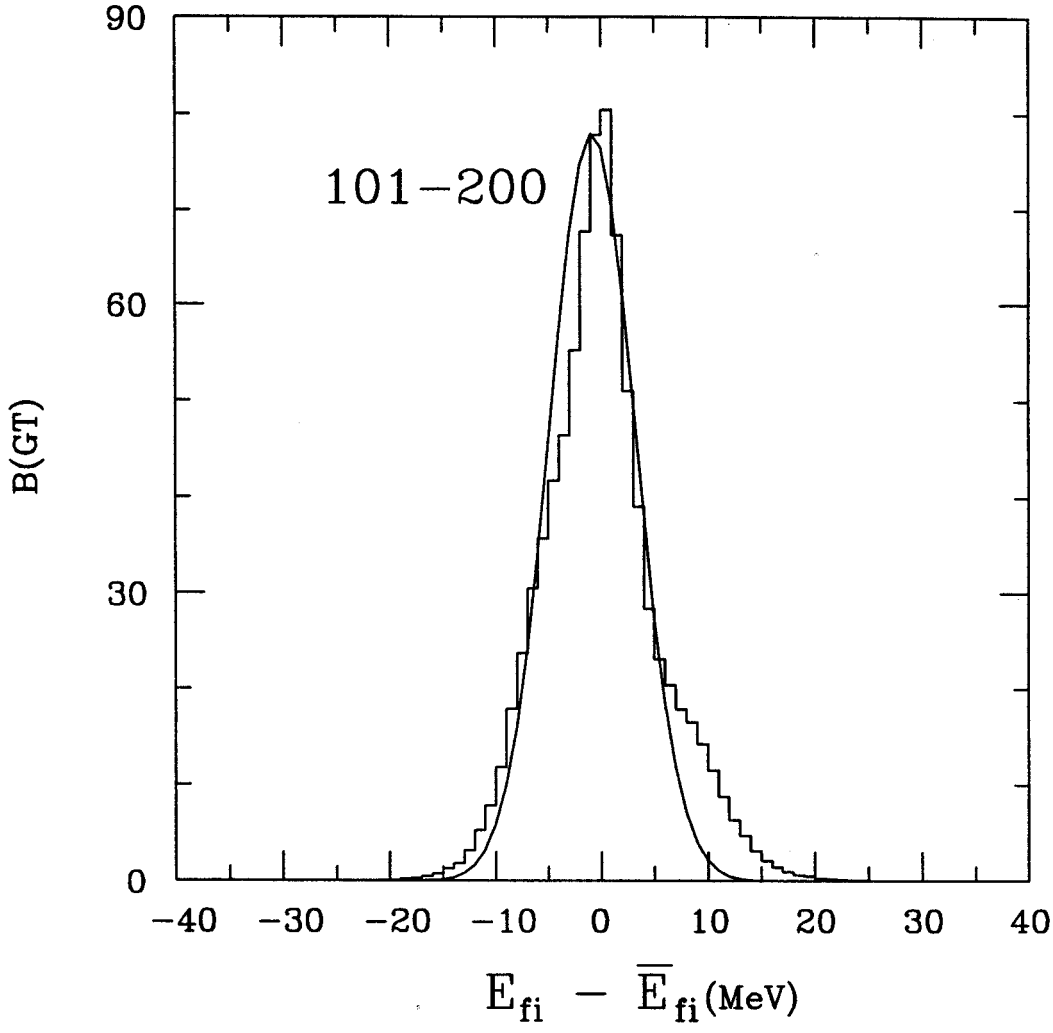

Figure 5.5: Gaussian fit (solid line) to the Gamow-Teller strength function, $B(GT; i \rightarrow f)$, for the mid 100 initial states and all final states, plotted as a function of ΔE, between initial and final energies.

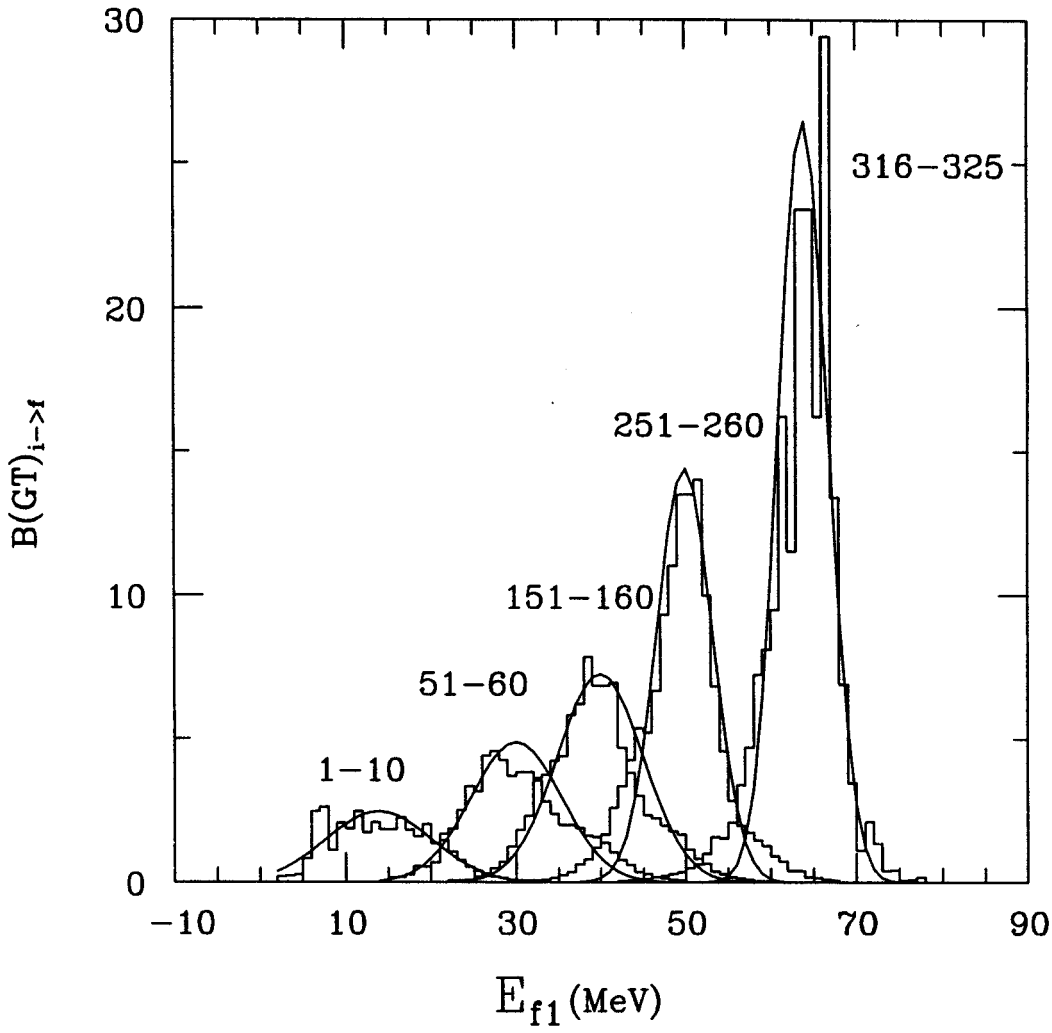

Figure 5.6: Gamow-Teller strength function, $B(GT; i \rightarrow f)$, for ^{24}Mg plotted as a function of ΔE, between the initial ^{24}Mg ($J^{\pi}T = 0^{+}0$) and the final ^{24}Na ($J^{\pi}T = 1^{+}1$) states. Solid lines represent Gaussian fits to the histograms.

from $\Gamma = 14.6$ MeV for states $1 - 10$ to $\Gamma = 6.8$ Mev for states $316 - 325$. This decrease of the spreading width is qualitatively understood: as $B(GT)$ increases, the states get more collective with respect to the GT operator and less chaotic.

5.2.3 Restricted Transition Strength Distribution

Recall the asymmetry of the GT strength function distribution for the first 100 states (5.3 a). Obviously, the first question such a distribution raises is whether this lack of symmetry is related to the probable transitions in this energy region.

This can be understood by examining the level spacing of the three active orbitals in the *sd*-shell (Fig. 5.7). The lowest $d_{5/2}$ level is highly populated at lower energies, thus making transitions from that orbital highly probable. In contrast, the higher $d_{3/2}$ level is weakly populated at lower energies and one does not expect transitions from unoccupied levels. The situation reverses itself for highly excited states, at which point we see the switch in the role of these strengths.

Because the $d_{5/2}$ orbital is so highly populated at lower energies, we expect that transitions from that orbital are the most active and contribute the most to the distribution.

The non-zero values for the *sd*-case correspond to the following (lj, lj') transitions:

$$\begin{aligned} d_{5/2} &\longrightarrow d_{5/2} \\ d_{5/2} &\longrightarrow d_{3/2} \\ d_{3/2} &\longrightarrow d_{3/2} \\ d_{3/2} &\longrightarrow d_{5/2} \\ s_{1/2} &\longrightarrow s_{1/2} \end{aligned}$$

These transitions correspond to the terms in the calculation of the strength that contribute to the coherent pattern. By restricting j and j', we observe these contributions in the absence of interference. This is done within the OXBASH code, by taking

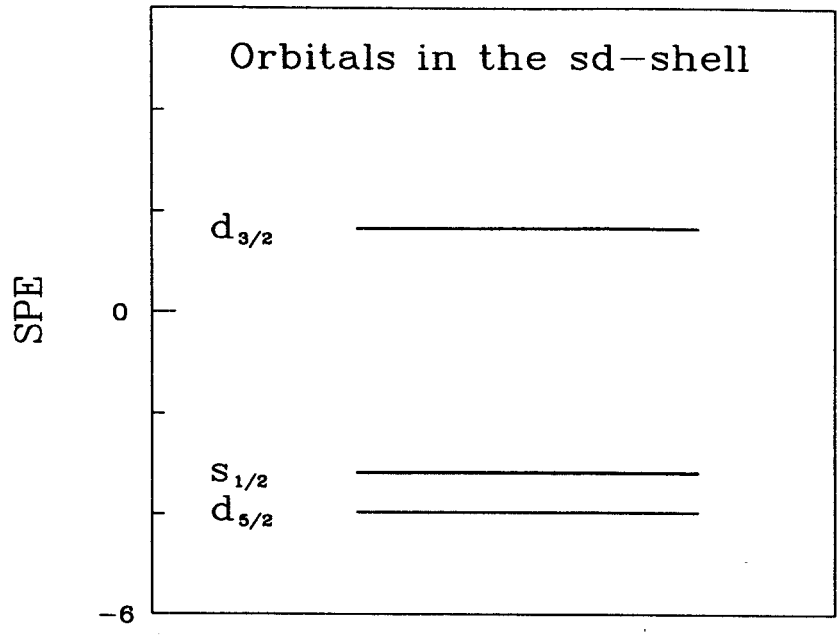

Figure 5.7: Level spacing of the three active orbitals in the *sd*-shell on the single-particle energy scale.

single-orbit transition densities. Numerically the strength comes from squaring the sum over orbitals, j, j', of the following matrix element

$$M(GT; i \rightarrow f) = \sum_{j,j'} OBTD(f,i,j,j') \langle j|\sigma_\mu \tau_\pm|j'\rangle \tag{5.6}$$

where, $\langle j|\sigma_\mu \tau_\pm|j'\rangle$ is the single-particle matrix element or $SPME(j,j')$, and the one-body transition density ($OBTD$) is given by

$$OBTD(f,i,j,j') = \langle f \,||| [a^\dagger(j) \otimes \tilde{a}(j')]^{(\Delta J, \Delta T)} ||| \, i \rangle / \sqrt{(2\Delta J + 1)(2\Delta T + 1)} \tag{5.7}$$

From 5.6 one can clearly see that depending on the phase of the $OBTD(f,i,j,j')$ and the $SPME(j,j')$, or more specifically, the phase of the product of $OBTD(f,i,j,j') \times SPME(j,j')$, one can achieve either constructive or destructive interference,

$$B(GT; i \rightarrow f) = |M(GT; i \rightarrow f)|^2. \tag{5.8}$$

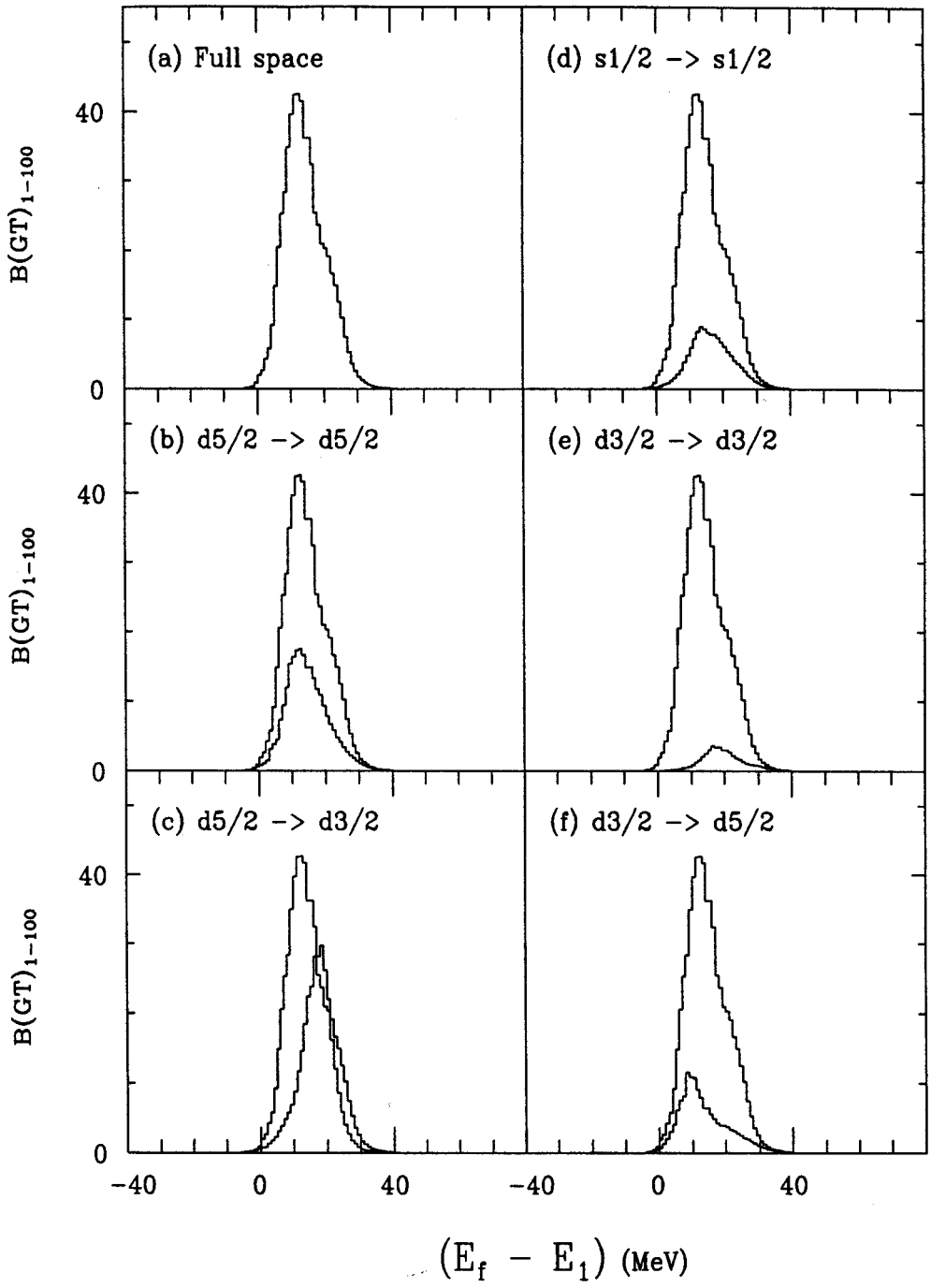

Figure 5.8: GT strength distribution for the first 100 states with no restrictions, panel a, and for the five restricted transitions, panels b - f. $B(GT; i \rightarrow f)$, versus the energy difference $E_f - E_1$.

Figure 5.8 reveals that the greatest contribution to both the amplitude and the asymmetry of the distribution for the first 100 states is from the $d_{5/2} \longrightarrow d_{3/2}$ transition. The relative size of this restricted transition is not unexpected when one considers the occupation of the $d_{5/2}$ orbital at low excitation energy. The asymmetry can be understood by the change in spin. The GT operator cannot change the orbital angular momentum, but it can, and does in this case change the spin angular momentum. Figure 5.8 shows the transitions responsible for the pronounced asymmetry as well as the regions within the spectrum in which the various transitions dominate the strength. The $d_{5/2} \longrightarrow d_{3/2}$ distribution has its mean at a higher energy than the $d_{5/2} \longrightarrow d_{5/2}$, in accordance with the larger amount of energy needed to excite a particle into the $d_{3/2}$ orbital.

5.3 Total Gamow-Teller Strength

5.3.1 Introduction

The total strength of the Gamow-Teller distribution is important to our understanding of the transition rates to excited states of the daughter nucleus. Without this information, we cannot accurately discern the relative abundances in stars. This carries over into our estimates for the mass and lifetime of pre-supernova stars. Granted, these are only theoretical calculations, but the information obtained from the magnitude and enhancement of the total strength as a function of excitation energy (temperature) might prove to be invaluable in probing the structure of the nucleus and the structure of stars.

Having already discussed the fragmentation of the strength resulting from the strong mixing of simple configurations (section 5.2), we now move on to our study of the strength function summed over all final states $|f\rangle$ which gives the *total* GT

strength, B_{GT}, of the initial state $|i\rangle$,

$$B_{GT}^{(\pm)}(i) = \sum_f B_{GT}^{(\pm)}(i \to f) = \sum_f |\langle f|O^{(\pm)}|i\rangle|^2 = \langle i|O^{(\pm)\dagger}O^{(\pm)}|i\rangle \tag{5.9}$$

where the closure summation over $|f\rangle$ was used.

The sum rule tells us that the difference in total strength of the $B_{GT}(+;i)$ and the $B_{GT}(-;i)$ is directly related to the number of protons and neutrons in the initial nucleus

$$S(GT) = B_{GT}^{-}(i) - B_{GT}^{+}(i) = 3(N_i - Z_i) \tag{5.10}$$

^{24}Mg has $N = Z = 12$, therefore

$$\sum_f B_{GT}^{-}(i \to f) = \sum_f B_{GT}^{+}(i \to f) \tag{5.11}$$

From this result we can cease to denote $B_{GT}^{\pm}(i)$, and concentrate on the behavior of the total strength, $B_{GT}^{\pm}(i) = B(GT)$ as a function of excitation energy (Fig. 5.9).

5.3.2 Single-Particle Estimate

In the absence of the obvious interference that results from residual interaction, one can obtain a reasonable idea of the value expected for the total strength. This result is based on the fact that a bare nucleon has $B(GT) = 3$, and that the nucleons, being fermions, have a limited number of orbital spaces, or holes, they can occupy, Ω. Within the *sd*-shell, there are 24 spaces, $\Omega_p = 12$ and $\Omega_n = 12$, available.

Assuming that the very complicated eigenstates have nearly random phases of components [21, 43], we can substitute the one-body transition densities by their mean values for the heated Fermi-liquid, $\sqrt{n_{j'l}(1 - p_{jl})}$ in terms of neutron and proton mean occupation numbers (the GT operator does not change the orbital momentum l). For the occupancies which on average do not depend on the projection m_j, we

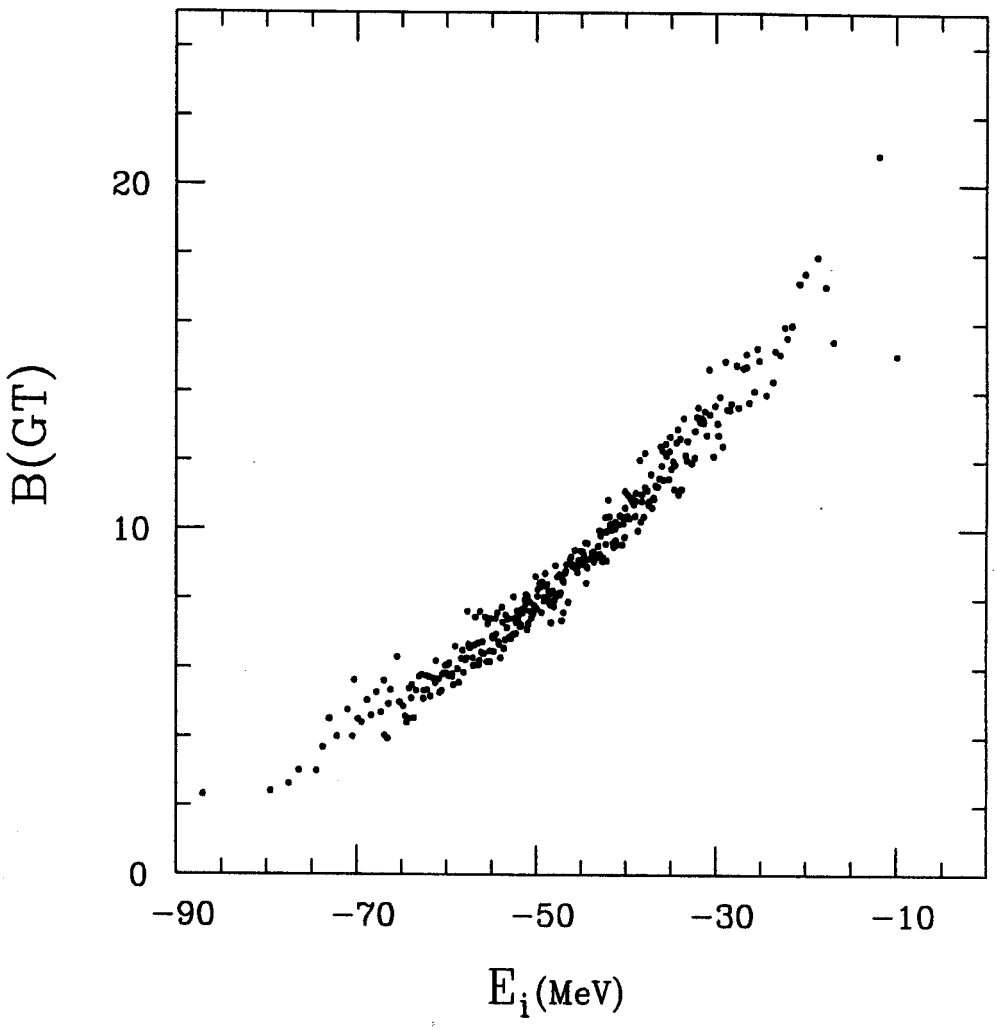

Figure 5.9: Total Gamow-Teller strength, $B(GT)$, for ^{24}Mg plotted as a function of initial ^{24}Mg ($J^{\pi}T = 0^{+}0$) energy.

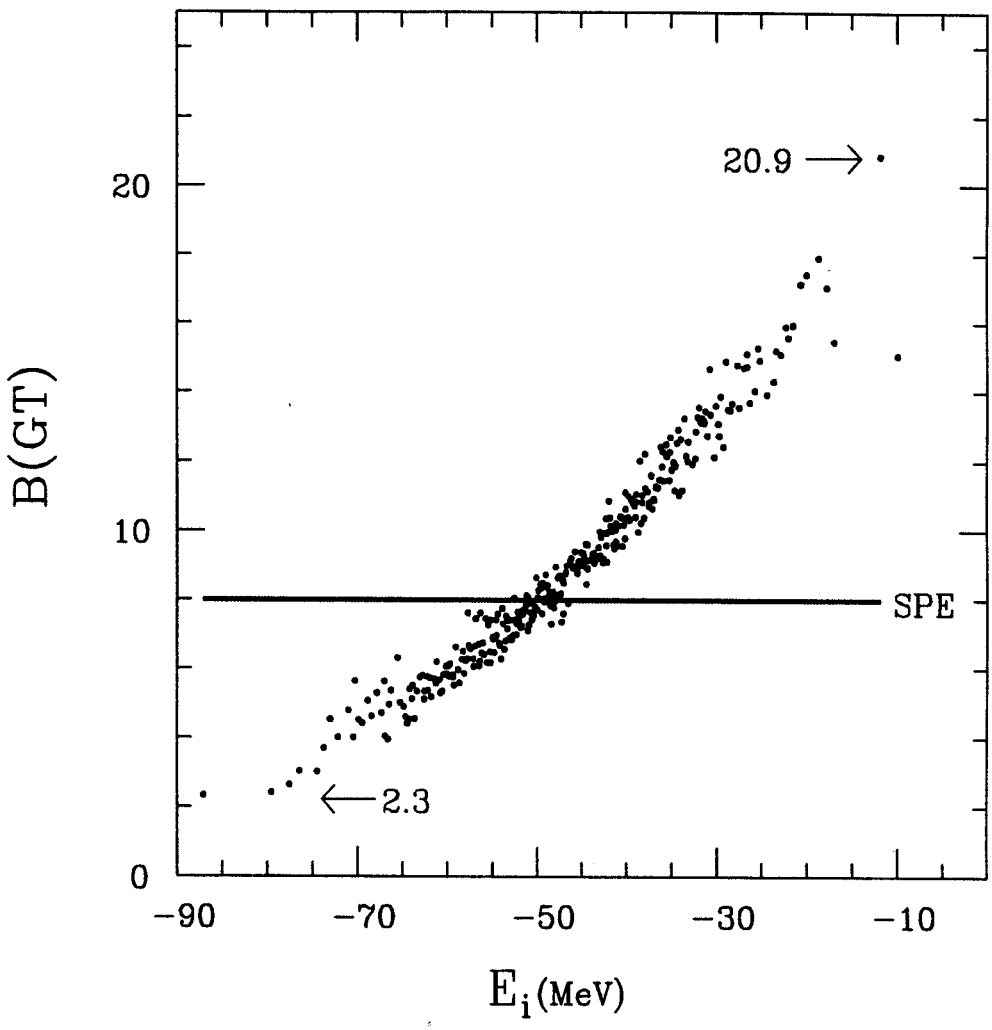

Figure 5.10: Total Gamow-Teller strength for ^{24}Mg in relation to the single-particle estimate (SPE). Plotted as a function of initial energy.

obtain

$$B(GT)^{(-)} = \sum_{jj'l} n_{j'l}(1 - p_{jl})6(2j+1)(2j'+1) \left\{ \begin{array}{ccc} j & 1 & j' \\ 1/2 & l & 1/2 \end{array} \right\}^2 . \qquad (5.12)$$

This approximation neglects all coherent effects and leads to a very weak energy dependence of the strength. In particular, the lowest unperturbed state with 4 particles in the $d_{5/2}$ level would have $n_{d5/2} = p_{d5/2} = 2/3$ and $B(GT) = 8.3$ while the highest unperturbed state with the filled $d_{3/2}$ orbit would have $B(GT) = 9.6$.

The middle of the shell-model spectrum corresponds to the equipopulation of the orbitals ("infinite temperature", [21, 35]). Then (5.12) simplifies to the universal result

$$B(GT)^{(-)} = 3N \left(1 - \frac{Z}{\Omega_p}\right) \qquad (5.13)$$

where the Pauli blocking factor is just the average proton population of available Ω_p orbitals; eq. 5.13 gives 8 in the case under study. Precisely the same result (5.13) follows from the statistical spectroscopy [42] as an average for all states allowed for given N and Z in a truncated shell-model space, regardless of their exact quantum numbers. This number is close to what we see in the middle of the spectrum.

5.3.3 Coherence of Total Strength

The reduction present in the model calculations for Gamow-Teller strengths from the ground state is well established. That it is even stronger in the experimental data supposedly reveals a part of the GT strength related to the excitation of the configurations outside of the shell-model states or delta-isobar excitation. The shell-model suppression is related to the sensitivity of the GT strength to spin-isospin correlations. Although the residual interaction strongly mixes the orbital and spin components of angular momentum, in general the energetically lowest states prefer spatial symmetry and, accordingly, spin-isospin asymmetry of the many-body wave

functions. This asymmetry hinders the GT transitions involving spin-isospin flip components which become partly forbidden by the Pauli blocking. Therefore one should expect the opposite effect of enhanced GT strength to be revealed for the high lying states with spatially asymmetric wave functions. Indeed, our calculations in the *sd*-shell model show that the magnitude of the reduction decreases for higher excitation energies and turns into enhancement for transitions in the mid- to high-energy region of the spectrum.

The reduction at lower excitation energies and enhancement at higher excitation energies is a direct result of the residual interaction. The qualitative explanation becomes obvious when the probabilities of the nucleon pairs of different symmetry are considered for the many-body wave functions. Defined as a sum over the nucleons, the GT operator can be written as

$$O^{(\pm)} = \sum_{nucleons} \left(\sum_{\mu} \sigma_{\mu} \tau_{\pm} \right) = \sum_{\lambda\lambda'} (\sigma_{\mu} \tau_{\pm})_{\lambda\lambda'} a^{\dagger}_{\lambda} a_{\lambda'} \tag{5.14}$$

where the equivalent form is given in second quantization, λ means a complete set of single-particle quantum numbers including the isospin projection. According to the GT sum rule (5.10), the difference in total strength is directly related to the number of protons and neutrons in the initial nucleus. For $N = Z$ nuclei it is sufficient to consider one of those sums, let us say $B(GT)^{(-)}$. Using the anticommutator relations, the expression for the strength (5.9) can be split into single-particle ($\sim a^{\dagger}a$) and pair ($\sim (a^{\dagger}a^{\dagger})(aa) \sim \sum A^{\dagger}_{ST} A_{ST}$) parts where $A^{\dagger}_{ST}$ and A_{ST} correspond to the pairs with total spin and isospin of S and T, respectively. The Pauli principle determines the spatial symmetry $(-)^L$ of a pair according to $(-1)^{S+T+L} = -1$. After a little algebra we obtain the general equation [59]

$$B(GT)^{(-)} = B_{s-p} + B_{pair} = 3\{N - \langle N_{0,1} \rangle - \frac{1}{3}\langle N_{1,0} \rangle + \langle N_{0,0} \rangle + \frac{1}{3}\langle N_{1,1} \rangle\} \tag{5.15}$$

where $3N$ would be the result for a pure system of N neutrons whereas $\langle N_{S,T} \rangle$ gives

an expectation value of the number of pairs with quantum numbers $S, T, T_3 = 0$ in the state $|i\rangle$. The spatially symmetric $p-n$ pairs give a negative contribution while the spatially anti-asymmetric pairs contribute positively. For example, in the case of $J = 0$ states of one valence $p-n$ pair, we have $T = 1$, so the exact prediction of (5.15) is 0 for a spin singlet, $S = L = 0$, and 4 for a spin triplet, $S = L = 1$. Without going into details of the nuclear structure we see that, depending on correlations, the result for a many-pair state, roughly speaking, ranges from $B(GT) = 0$, for $\langle N_{0,1}\rangle = N$, to $B(GT) = 6N$, for $\langle N_{0,0}\rangle = N$. These estimates can be further improved by taking into account the nonorthogonality of the components of the many-body wave functions with different pair contents.

The total GT strength (5.9) is shown in Fig. 5.9 as a function of excitation energy for all 325 individual $J^\pi T = 0^+0$ states in ^{24}Mg found in the *sd*-shell model. We see the clear trend of the monotonic increase of the $B(GT)$ with excitation energy. The lowest and the highest possible values are close to the borders of the range predicted by eq. (5.15), 0 and 24, for $N = Z = 4$.

In the jj-coupling scheme the $SU(4)$ symmetry is violated by the spin-orbit interaction. The matrix element $\langle f|O|i\rangle$ of any one-body operator between complicated many-body states is the coherent sum of the products of single-particle matrix elements, $(j||\sigma_\mu\tau_-||j')$ in our case, and the one-body transition densities $\langle f||a^\dagger a||i\rangle$.

As stated earlier, there are 5 non-zero values of the product $SPME \times OBTD$, and we have an interference between these terms. The statistical consideration neglects the interference effects between these 5 partial transitions contributing to the total GT strength. This interference, destructive at low energies and constructive at higher energies, is responsible for the regular behavior seen in Fig. 5.9. The partial contributions to the total GT strength for all 5 groups of transitions can be seen in

Fig. 5.11. The transitions with ($j = j'$) have relatively flat distributions while those that involve two different orbitals ($j \neq j'$), have strengths that slightly increase and decrease with excitation energy. In agreement with (5.12), this reflects an average population of $d_{5/2}$ and $d_{3/2}$ orbitals according their single-particle energy levels in the *sd*-shell with spin-orbital coupling. The sum of the partial strengths, shown in Fig. 5.12 *b*, is close to the single-particle estimate and the energy behavior is noticeably flatter than that of the original, unrestricted strength (Fig. 5.12 *a*). This is a direct result of the omission of interference.

Since the coherence effects for the GT operator are related to the interplay of spatial and spin-isospin symmetry, they can be revealed in the appropriate basis, namely the Wigner supermultiplet basis characterized by the Young tableaux $[f]$, quantum numbers $(\lambda\mu)$ of the $SU(3)$ group, orbital L, spin S and total angular momentum J, isospin T and additional quantum numbers for multiple occurrences. Components of the Gamow-Teller operator are among the generators of the $SU(4)$ group which allows one to calculate their matrix elements using the Racah algebra for the $SU(4)$ group developed by Hecht and Pang [44], see also [45].

The result for the $B(GT)$ is very simple for $T = 0$ initial states. Namely, for pure supermultiplet states with the total spin S, the sum rule is [60]

$$B(GT) = \frac{2}{3}\{C[SU(4)] - S(S+1)\} \tag{5.16}$$

Here $C[SU(4)]$ are the eigenvalues for the Casimir operator of the $SU(4)$ group (quadratic sum of the generators). They are given by [60]

$$C(SU4) = [P(P+4) + P'(P'+2) + (P'')^2] \tag{5.17}$$

where, for the Young tableaux $[f]$ (see also Appendix E),

$$P = \frac{1}{2}(f_1+f_2-f_3-f_4), \quad P' = \frac{1}{2}(f_1-f_2+f_3-f_4), \quad P'' = \frac{1}{2}(f_1-f_2-f_3+f_4). \tag{5.18}$$

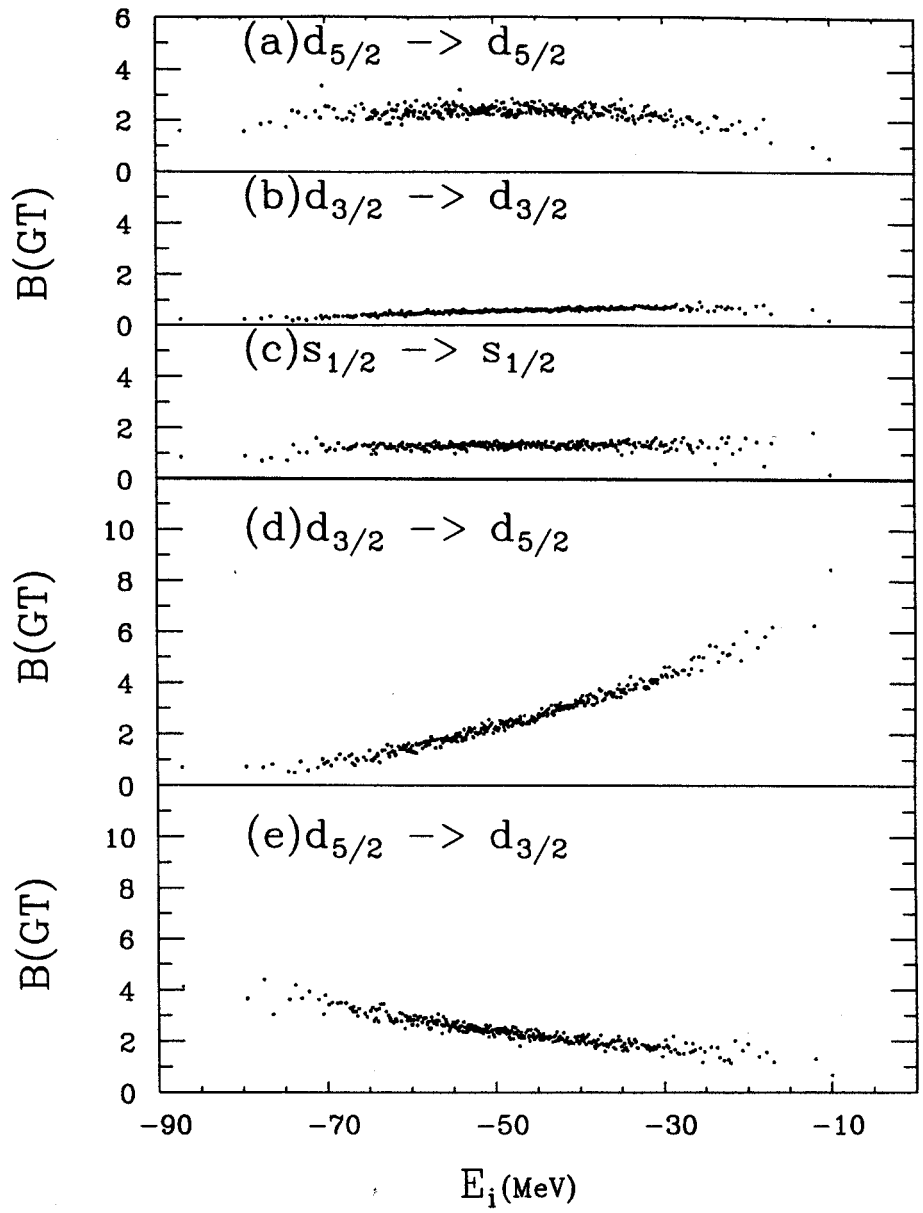

Figure 5.11: Total Gamow-Teller strength for ^{24}Mg in the case of unrestricted transitions, panel (a), $d_{5/2} \rightarrow d_{5/2}$, panel (b), $d_{3/2} \rightarrow d_{3/2}$, panel (c), $s_{1/2} \rightarrow s_{1/2}$, panel (d), $d_{5/2} \rightarrow d_{3/2}$, panel (e), $d_{3/2} \rightarrow d_{5/2}$, panel (f). Plotted as a function of initial energy.

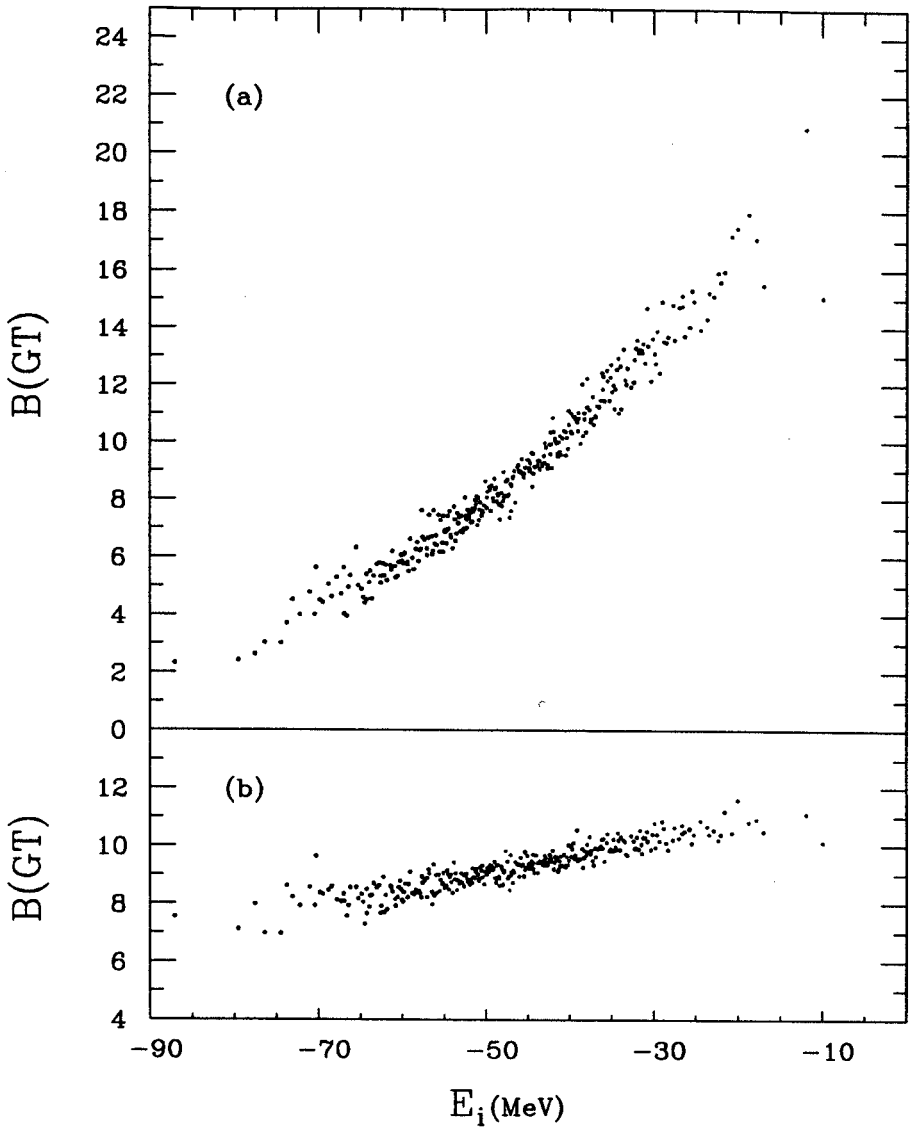

Figure 5.12: The total strength for unrestricted transitions, panel a, the sum of the five individual strengths, $\sum_\alpha B(GT;\alpha)$,panel *b*. Plotted as a function of initial ^{24}Mg ($J^\pi T = 0^+0$) energies.

Since $C[SU(4)]$ increases with decreasing spatial symmetry, this explains the resulting increase in the total GT strength. The strong space-exchange component in the two-body effective interaction is going to order the states in this way before the spin-orbit force disrupts the symmetry. The GT sum-rule for the shell-model ground states of ^{24}Mg will be a linear combination of the values in Eq. (5.16) weighted by the intensities for each $[f]$ and S in the wave function. In a sense, the total GT strength is a measure of the $SU(4)$ symmetry breaking and of the strength of the spin-orbit interaction. For the states $J = T = 0$ in ^{24}Mg the minimum strength is zero, and the maximum is $B(GT) = 76/3$, in agreement with our findings. The maximum is reached for $[f] = [62]$ and $S = 2$; the [62] symmetry with $S = 0$ which would correspond to even bigger value $B(GT) = 88/3$ does not occur for $J = 0$ since the only allowed $SU(3)$ representation $(\lambda\mu) = (21)$ is incompatible with $L = 0$.

The shell-model hamiltonian consists of the independent particle (one-body) part and the two-body residual interaction, $H = H_0 + H'$. The almost perfect antisymmetric pattern of the $B(GT)$ reduction at lower excitation energies and enhancement at higher excitation energies can be mimicked by using a "mirror reflected" hamiltonian $\tilde{H}$ in which we change the sign of the residual interaction,

$$\tilde{H} = H_0 - H' \tag{5.19}$$

In the finite Hilbert space the transition occurs in the mid energy region along with the transition [35] to the negative temperatures and decreasing complexity of the eigenstates.

Finally, we are able to compare the complementary behavior of the Gamow-Teller strength for our original hamiltonian to that of the Gamow-Teller strength for a hamiltonian (5.19) where the sign of the residual interaction H' is changed. From this conclude that the effective sign of the two-body interaction becomes negative once

we begin considering initial-state configurations that correspond to higher excitation energies. In fact, this change occurs in the mid-energy region where the total strength begins to exceed the single-particle estimate.

5.4 Summary

Our main points relating to Gamow-Teller strength functions, as far as the shape of the "average" distribution is concerned, are as follows:

1. For the Gamow-Teller strength distribution for the states in the mid-energy, high-density region, states 101 through 200, we have a Gaussian fit to the central part of the distribution (figure 5.5). The width of the distribution is Γ_{GT} = 9.5(6) MeV.

2. We see the high energy tail reminiscent of the basis state and single-nucleon transfer distributions of chapter 4.

3. The greatest contribution to both the amplitude and the asymmetry of the distribution for the first 100 states is the $d_{5/2} \longrightarrow d_{3/2}$ transition.

4. The relative size and position of this restricted transition is not unexpected when one considers (1) the occupation of the $d_{5/2}$ orbital at low excitation energy, and (2) the larger amount of energy needed to excite a particle into the $d_{3/2}$ orbital.

We have three major points that have been made about the total strength, both unrestricted and restricted.

1. The spatially symmetric p–n pairs give a negative contribution to total Gamow-Teller Strength while the spatially anti-symmetric pairs contribute positively.

The exact prediction of $B(GT)$ in terms of $\langle N_{S,T} \rangle$ is $B(GT)^{(-)} = 3\{N - \langle N_{0,1} \rangle - \frac{1}{3}\langle N_{1,0} \rangle + \langle N_{0,0} \rangle + \frac{1}{3}\langle N_{1,1} \rangle$. This equation yields 0 for a spin singlet, $S = L = 0$, and 4 for a spin triplet, $S = L = 1$. So the result for a many-pair state ranges from $B(GT) = 0$, for $\langle N_{0,1} \rangle = N$, to $B(GT) = 6N$, for $\langle N_{0,0} \rangle = N$.

2. The transitions with $(j = j')$ have relatively flat distributions while those that involve two different orbitals $(j \neq j')$, have strengths that slightly increase and decrease with excitation energy, reflecting an average population of $d_{5/2}$ and $d_{3/2}$ orbitals according to their single-particle energy levels in the *sd*-shell with spin-orbital coupling.

3. The incoherent sum is close to the single-particle estimate and the energy behavior is noticeably flatter than that of the original, unrestricted strength. This is a direct result of the omission of interference.

4. The narrow width and strongly enhanced $B(GT)$ value for highly excited states shows the coherent collectivity of the GT mode and the strength concentration in the region of predominantly odd orbital symmetry.

Chapter 6

Conclusion

The proven sucess of the nuclear shell model in predicting various experimental observables in the region of low-lying states encourages us to extend its use into the region of high-lying states in order to reach some conclusions about statistical features of the more complicated states. Our studies of these light nuclei are meant to serve as prototypes of general nuclear properties, including those for heavier nuclei whose observables remain beyond the scope of shell-model calculations due to the increase in the dimensionality of shell-model space.

We set out to (1) study the fragmentation of simple shell-model configurations as a function of excitation energy and interaction strength, (2) determine the effect that basis state mixing has on the distributions of the strengths associated with simple operators, $a^\dagger_\lambda$ and $[(\sigma_\mu \tau_\pm)_{\lambda\lambda'} a^\dagger_\lambda a_{\lambda'}]$, and (3) analyze the total Gamow-Teller strength as a function of excitation energy in order to gain theoretical information about excited states of the nucleus.

Table 6.1 shows the values for Full-Width at Half-Maximum (FWHM) taken from both the average interaction with $\overline{\Gamma} \approx 2\,\overline{\sigma}$ for strong coupling, where $\sigma^2_{basis} = \sum_\alpha (C^\alpha_k)^2 (E_\alpha - \bar{E}_k)^2$, and the fits to the various strength distributions for the basis states Γ_{basis}, single-nucleon transfer Γ_{at}, and GT transitions Γ_{GT}. Note that the

$A_v = 12$ system cannot be compared to the $A_v = 8$ without taking into account the different number of valence nucleons present. For this reason we take $\Gamma_{basis} \sim 18$ for $A_v = 8$.

Table 6.1: Energy dispersion and widths for 12 and 8 valence nucleons in the $0d1s$ shell-model space.

	From average interaction		From χ^2 fit		
A_v	$\bar{\sigma}$ (MeV)	$\bar{\Gamma}$ (MeV)	Γ_{basis}	Γ_{at}	Γ_{GT}
12	9.8	19.6	20	-	-
8	9.2	18.2	(18)	8.6	9.5

6.1 Strength Function

The strength function for simple configurations of independent particles was, for the first time, extracted from the exact solution of the many-body problem in the truncated Hilbert space of shell-model configurations. Taking the most complicated states near the middle which could be considered as uniform in their properties, we examined the shape and the width of the strength function. For realistic interaction strengths the results are not satisfactorily described by the standard Breit-Wigner model of the strength function. Rather, the generic shape of the compound states at high excitation energy is close to a Gaussian but with exponential wings. In order to better understand this we investigated evolution of the strength function from the region of "strong" to"weak" mixing. The uniformity of the dispersion supports the idea of saturation of the spreading width [25, 16] which has important consequences for understanding the damping of giant resonances.

The variance obtained from the Gaussian fit is $\sigma_{basis} = 8.3 \pm 0.3$ MeV giving a spreading width (FWHM) of the central 0^+0 states equal to $\Gamma_{basis} = \sqrt{(8 \ln 2)}\, \sigma_{basis} =$ 19.6 MeV. This width agrees with the estimate (3.27), $\Gamma_{SC} = 2\bar{\sigma} = 20$ MeV made for the strong coupling limit. It is clear the the Breit-Wigner shape predicted by the standard model of the strength function does not hold in the realm of realistic coupling.

We observe deviations from the Gaussian shape in the tails of the strength function, Fig. 3.7*b*. Fig. 3.11 shows that the wings can be described by an exponential fit $F_k(E - \bar{E}_k) \approx F_0 \exp\left(-\frac{E-\bar{E}_k}{E_l}\right)$. The exponential tails of the strength function $F_k(E)$ can be reproduced by perturbation theory.

The transition to the weak coupling case at the artificially suppressed strength of the residual interaction shows how the shape of the strength function regularly changes from the Gaussian to the "normal" Breit-Wigner as λ changes from $1 \rightarrow 0$. This is accompanied by the reduction of the spreading width and the smooth transition from the linear interaction dependence characteristic for the strong coupling limit to the ordinary quadratic dependence predicted by the golden rule. This transition is seen for the first time in realistic calculations. The detailed behavior of the spreading width as a function of the interaction strength depends on the explicit dependence of the level density and the coupling matrix elements on energy of the background states. Just as we can artificially suppress the interaction to retrieve the standard golden rule, we can enhance the interaction. By setting $\lambda = 1.2$ we see the continuation of the linear trend. We also see that the Gaussian level density determines the shape of the strength function distribution, even for the wings which were formerly described by an exponential curve (Fig. 3.18).

6.2 Spectroscopic Factors

As with the fragmentation of shell-model basis states, and later with Gamow-Teller strength distributions, there is a distribution of strength for spectroscopic factors. Its spreading width turns out to be smaller than that for basis states. The simplicity of the raising operator $a^{\dagger}_{j,t}$ precludes it from changing the initial eigenstate wavefunction $|i\rangle$ to the extent that $\langle f|a^{\dagger}|i\rangle \equiv \langle f|k'\rangle$ is not spread as much as $\langle f|k\rangle$ (recall that $|k\rangle$ are the original shell-model basis states).

The small change in the width of the three average strength distributions ($1-100$, $101-200$, $201-325$) is consistent with a conclusion that the transition strengths depend on the energy spacing between the initial and final state energy levels ($E^{\star}_{fi}$), but not on the level from which the nucleon transfer occurs.

We also achieve a more accurate Full Width at Half-Maximum, $\Gamma_{a\dagger} = 8.55(34)$, by making a low-energy cut on the distribution of the spectroscopic factor. The width for the middle set of spectroscopic amplitudes (Fig. 4.5) is $\Gamma_{a\dagger} = 8.73(76)$ without the low-energy cut.

The decrease in the width of the spectroscopic factor strength distribution confirms our assessment that final-state wavefunctions are closer to initial-state wavefunctions that have been acted on by a simple operator, than they are to basis states.

Both the Gaussian shape and the decrease in width relative to basis-state strength functions, $\Gamma_{basis} = 20$ MeV to $\Gamma_{a\dagger} = 8.7$ MeV, are to be expected. The Gaussian character of the distribution follows directly from the fact that we are again in the region of strong mixing.

6.3 Gamow-Teller Strengths

Gamow-Teller strength distributions for the states in the mid-energy, high-density region have a Gaussian fit to the central part of the distribution. We see the high energy tail reminiscent of the basis state and single-nucleon transfer distributions of chapter 4 and the width of the distribution is $\Gamma_{GT} = 9.5(6)$ MeV.

The greatest contribution to both the amplitude and the asymmetry of the distribution for the first 100 states is the $d_{5/2} \longrightarrow d_{3/2}$ transition. The relative size and position within the spectrum of this restricted transition is not unexpected when one considers (1) the occupation of the $d_{5/2}$ orbital at low excitation energy, and (2) the larger amount of energy needed to excite a particle into the $d_{3/2}$ orbital.

Clearly our calculations show the well established reduction in the total strength for transitions from low-lying states. In the model, this reduction arises from two-body interactions, dominance of orbital symmetry in the low end of the spectrum, and the mixing of shell-model eigenstates. The calculations also show enhancement for highly-excited states. The spatially symmetric $p-n$ pairs give a negative contribution to total Gamow-Teller strength while the spatially anti-symmetric pairs contribute positively. The result for a many-pair state yields a $B(GT)$ that ranges from $B(GT) = 0$ to $B(GT) = 24$.

The entire picture of the GT strength is determined by the main features of the residual interaction related to the spatial and spin-isospin symmetry. This picture is seen clearly against the background of the incoherent collision-like interactions. The coexistence of regular nuclear motion with chaotic single-particle dynamics was discussed in a different context in [55]. Exotic $N \approx Z$ nuclei can supply additional information concerning the role of symmetry in nuclear stability [54].

We have also garnered information by restricting the allowed transitions. We have

seen the behavior of the five non-zero single-particle transitions; the level behavior of the three transitions that involve one orbital and the mirror-like behavior of the two that involve two different initial and final orbitals. This reflects an average population of $d_{5/2}$ and $d_{3/2}$ orbitals according their single-particle energy levels in the *sd*-shell with spin-orbital coupling. The sum is close to the single-particle estimate and the energy behavior is noticeably flatter than that of the original, unrestricted strength. This is a direct result of the omission of interference.

6.4 Notes

Clearly, more work remains to be done in this area, but I take these open questions to be promising hints of what this train of investigation can lead to. New effects will enter when the presence of real decay into continuum is taken into account. The competition of the internal mixing, external decay and interaction through common decay channels makes the whole problem more complicated. This interplay of various mechanisms will determine the physics of compound states at high excitation energy in stable nuclei and at lower excitation energy in weakly-bound nuclei.

APPENDIX

Appendix A

Matrix Elements for the $0s - 1d$ Shell Model Space

$T=1\ J=0$	$s^2_{1/2}$	$d^2_{3/2}$	$d^2_{5/2}$
$s^2_{1/2}$	-2.125	-1.084	-1.325
$d^2_{3/2}$		-2.185	-3.186
$d^2_{5/2}$			-2.820

$T=1\ J=2$	$d^2_{3/2}$	$d^2_{5/2}$	$d_{3/2}s_{1/2}$	$d_{5/2}s_{1/2}$	$d_{5/2}d_{3/2}$
$d^2_{3/2}$	-0.067	-1.622	-0.515	-0.404	-0.615
$d^2_{5/2}$		-1.002	-0.620	-0.862	-0.283
$d_{3/2}s_{1/2}$			-0.406	-1.941	-0.525
$d_{5/2}s_{1/2}$				-0.818	-0.477
$d_{5/2}d_{3/2}$					-0.325

$T=1\ J=4$	$d^2_{5/2}$	$d_{5/2}d_{3/2}$
$d^2_{5/2}$	-0.164	-1.236
$d_{5/2}d_{3/2}$		-1.450

$T=1\ J=1$	$d_{3/2}s_{1/2}$	$d_{5/2}d_{3/2}$
$d_{3/2}s_{1/2}$	+0.607	+0.187
$d_{5/2}d_{3/2}$		+1.033

$T=1\ J=3$	$d_{5/2}s_{1/2}$	$d_{5/2}d_{3/2}$
$d_{5/2}s_{1/2}$	+0.762	+0.674
$d_{5/2}d_{3/2}$		+0.589

$T=0\ J=1$	$s^2_{1/2}$	$d^2_{3/2}$	$d^2_{5/2}$	$d_{3/2}s_{1/2}$	$d_{5/2}d_{3/2}$
$s^2_{1/2}$	-3.263	+0.028	-1.176	+1.250	+2.104
$d^2_{3/2}$		-1.415	+0.722	+0.398	+0.565
$d^2_{5/2}$			-1.632	-1.103	+2.543
$d_{3/2}s_{1/2}$				-4.293	-1.710
$d_{5/2}d_{3/2}$					-6.506

$T=0\ J=3$	$d^2_{3/2}$	$d^2_{5/2}$	$d_{5/2}s_{1/2}$	$d_{5/2}d_{3/2}$
$d^2_{3/2}$	-2.884	+1.895	+0.189	+2.034
$d^2_{5/2}$		-1.501	-1.242	+2.222
$d_{5/2}s_{1/2}$			-3.860	+1.203
$d_{5/2}d_{3/2}$				-0.538

$T=0\ J=5$	$d^2_{5/2}$
$d^2_{5/2}$	-4.226

$T=0\ J=2$	$d_{3/2}s_{1/2}$	$d_{5/2}s_{1/2}$	$d_{5/2}d_{3/2}$
$d_{3/2}s_{1/2}$	-1.819	+2.066	+0.283
$d_{5/2}s_{1/2}$		-1.447	+0.097
$d_{5/2}d_{3/2}$			-3.825

$T=0\ J=4$	$d_{5/2}d_{3/2}$
$d_{5/2}d_{3/2}$	-4.506

Appendix B

Subspaces for Nucleons in the $0s - 1d$ Shell Model Space

Table B.1: Dimensions of subspaces $J^\pi T$ for 12 particles in the *sd* shell.

$T\backslash J$	0	1	2	3	4	5	6	7	8
0	839	2135	3276	3711	3793	3278	2667	1848	1205
1	1372	3985	5768	6706	6562	5755	4434	3097	1882
2	874	2319	3434	3804	3700	3059	2285	1462	844

$T\backslash J$	9	10	11	12	13	14
0	657	334	126	48	8	1
1	1023	462	178	48	9	0
2	393	160	44	9	0	0

Table B.2: Dimensions of subspaces $J^\pi T$ for 8 particles in the *sd* shell.

$2T\backslash 2J$	0	2	4	6	8	10	12	14	16	18
0	325	779	1206	1304	1311	1070	835	531	329	154
2	481	1413	1992	2268	2131	1791	1293	843	460	222
4	287	721	1068	1135	1071	826	581	330	169	62

Table B.3: Dimensions of subspaces $J^\pi T$ for 9 particles in the *sd* shell.

$2T\backslash 2J$	1	3	5	7	9	11	13	15	17	19
1	1434	2581	3281	3444	3144	2544	1839	1168	657	315
3	1273	2299	2874	2958	2643	2063	1421	857	444	188
5	482	850	1042	1029	873	631	397	207	90	28

Appendix C

Output of BASIS code for OXBASH

Output of BASIS
9-JUN-97 12:08:19

OXBASH (Feb 1992)	
The Oxford-Buenos-Aires-MSU Shell-Model Code	
OXBASH82	: A.Etchegoyen, W.D.M.Rae and N.S.Godwin
	: contributors: W.A.Richter and C.H.Zimmerman
MSU version	: B.A.Brown, W.E.Ormand, J.S.Winfield, L.Zhao
	: and E. K. Warburton

Macro versions of extended-integer subroutines are being used
Present versions limited to 256 m-states and 24 j-states
No. of m states : 24
No. of j levels : 3
No. of states/level : 8 12 4
No. of major shells : 1
No. of levels/shell : 3
Labels of j-levels
1D3/2 1D5/2 2S1/2
total number of particles : 12
no. restrictions in filling j levels
nuclear spin : JZ = 0.0
isospin : TZ = 0.0
parity (0=+VE) = 0
name of BASIS output data file : B000CW

No.,	partition,	m-dim,	j-dim		
			J	J+1	J+2
1	8 4 0	29	2	0	3
2	7 5 0	276	3	9	13
3	6 6 0	1004	15	22	44
4	5 7 0	1648	15	42	62
5	4 8 0	1342	19	31	59
6	3 9 0	536	7	18	25
7	2 10 0	104	4	3	9
8	1 11 0	8	0	1	1
9	0 12 0	1	1	0	0
10	8 3 1	48	1	2	3
11	7 4 1	656	7	20	29
12	6 5 1	3164	27	76	112
13	5 6 1	6896	53	148	219
14	4 7 1	7392	56	159	237
15	3 8 1	3956	34	96	141
16	2 9 1	1024	12	32	46
17	1 10 1	116	2	6	8
18	0 11 1	4	0	0	1
19	8 2 2	28	2	1	3
20	7 3 2	476	6	17	24
21	6 4 2	3070	35	72	122
22	5 5 2	8832	67	191	282
23	4 6 2	12490	103	243	390
24	3 7 2	8832	67	191	282
25	2 8 2	3070	35	72	122
26	1 9 2	476	6	17	24
27	0 10 2	28	2	1	3
28	8 1 3	4	0	0	1
29	7 2 3	116	2	6	8
30	6 3 3	1024	12	32	46
31	5 4 3	3956	34	96	141
32	4 5 3	7392	56	159	237
33	3 6 3	6896	53	148	219
34	2 7 3	3164	27	76	112
35	1 8 3	656	7	20	29
36	0 9 3	48	1	2	3
37	8 0 4	1	1	0	0
38	7 1 4	8	0	1	1
39	6 2 4	104	4	3	9
40	5 3 4	536	7	18	25
41	4 4 4	1342	19	31	59
42	3 5 4	1648	15	42	62
43	2 6 4	1004	15	22	44
44	1 7 4	276	3	9	13
45	0 8 4	29	2	0	3

NO. OF TRIAL PATTERNS	:	1449979
M-SCHEME BASIS DIMENSION	:	93710
NO. OF BASIS PARTITIONS STORED	:	45
NO. LOOPS FOR TABLE LOOKUP	:	88374

NO. OF STATES WITH

2*J	:	0	2	4	6	8	10	12	14	16	18
2*T =	0 :	839	2135	3276	3711	3793	3278	2667	1848	1205	657
2*T =	2 :	1372	3985	5768	6706	6562	5755	4434	3097	1882	1023
2*T =	4 :	874	2319	3434	3804	3700	3059	2285	1462	844	393

Appendix D

Derivation of the Standard Model of the Spreading Width

The derivation of the standard model for the Breit-Wigner spreading width is outlined in [4]. Here, we fill in the details of that derivation. From equation 3.19, our assumption of the coupling intensities $V_{k\nu}^2$ weakly fluctuating around some mean value v^2, and with $\bar{E}_\nu = \nu\, D$, we can manipulate the energy difference $E_\alpha - \bar{E}_k$ into a certain form.

Making the substitutions (1) $V_{k\nu}^2 \approx v^2$ and (2) $E_\nu = \nu\, D$, equation D.1

$$E_\alpha - \bar{E}_k = \sum_\nu \frac{V_{k\nu}^2}{E_\alpha - E_\nu} \tag{D.1}$$

becomes,

$$\begin{aligned} E_\alpha - \bar{E}_k &= v^2 \Sigma_\nu \tfrac{1}{E_\alpha - E_\nu} \\ &= v^2 \Sigma_\nu \tfrac{1}{E_\alpha - \nu\, D} \\ &= \tfrac{\pi v^2}{D} \Sigma_\nu \tfrac{1}{\frac{\pi E_\alpha}{D} - \pi\nu} \qquad \text{(D.2)} \\ E_\alpha - \bar{E}_k &= \tfrac{\pi v^2}{D} cot\left(\tfrac{\pi\, E_\alpha}{D}\right) \end{aligned}$$

Giving,

$$cot\left(\frac{\pi E_\alpha}{D}\right) = \frac{D}{\pi v^2}(E_\alpha - \bar{E}_k). \tag{D.3}$$

Now we can incorporate the weight, $(C_k^\alpha)^2$ into our next step.

$$\begin{aligned}
(C_k^\alpha)^2 &= \left[1 + \Sigma_\nu \frac{V_{k\nu}^2}{(E_\alpha - E_\nu)^2}\right]^{-1} \\
&= \left[1 + v^2 \Sigma_\nu \frac{1}{(E_\alpha - \nu D)^2}\right]^{-1} \\
&= \left[1 + (\tfrac{\pi v}{D})^2 \Sigma_\nu \frac{1}{(\frac{\pi E_\alpha}{D} - \pi\nu)^2}\right]^{-1} \\
&= \left[1 + (\tfrac{\pi v}{D})^2 csc^2(\tfrac{\pi E_\alpha}{D})\right]^{-1} \\
&= \left[1 + (\tfrac{\pi v}{D})^2 \left(1 + cot^2(\tfrac{\pi E_\alpha}{D})\right)\right]^{-1}
\end{aligned} \tag{D.4}$$

Making the substitution from D.3 and taking into account that $(\langle v^2 \rangle / D^2 \gg 1)$, $(C_k^\alpha)^2$ can be written as

$$\begin{aligned}
(C_k^\alpha)^2 &= \left[1 + (\tfrac{\pi v}{D})^2 \left(1 + \left[\tfrac{D}{\pi v^2}(E_\alpha - \bar{E}_k)\right]^2\right)\right]^{-1} \\
&\simeq \left[(\tfrac{\pi v}{D})^2 \left(1 + \left[\tfrac{D}{\pi v^2}(E_\alpha - \bar{E}_k)\right]^2\right)\right]^{-1}
\end{aligned} \tag{D.5}$$

So,

$$(C_k^\alpha)^2 = \left[(\frac{\pi\, v}{D})^2 + \frac{(E_\alpha - \bar{E}_k)^2}{v^2}\right]^{-1}. \tag{D.6}$$

The strength function then, expressed in terms of mean weight (from D.6) and level density,

$$F_k(E) = \rho(E)\langle(C_k^\alpha)^2\rangle_{E_\alpha=E} \tag{D.7}$$

can be written as

$$\begin{aligned} F_k(E) &= \rho(E)\left[(\tfrac{\pi\, v}{D})^2 + \left(\tfrac{E_\alpha-\bar{E}_k}{v}\right)^2\right]^{-1} \\ &= \frac{1}{D\left[(\frac{\pi\, v}{D})^2+(\frac{E_\alpha-\bar{E}_k}{v})^2\right]} \end{aligned} \tag{D.8}$$

Next we set $\Gamma_s = 2\pi\frac{v^2}{D}$ and multiply by unity $\frac{\Gamma_s}{\Gamma_s}$.

$$\begin{aligned} &= \frac{\Gamma_s}{\left[\Gamma_s D(\frac{\pi\, v}{D})^2+\Gamma_s D\frac{(E_\alpha-\bar{E}_k)^2}{v^2}\right]} \\ F_k(E) &= \frac{\Gamma_s}{(2\pi(\frac{\Gamma_s}{2})^2+2\pi(E_\alpha-\bar{E}_k)^2} \end{aligned} \tag{D.9}$$

And finally, we have the strength function of Breit-Wigner shape predicted in the standard model of the spreading width,

$$F_k(E) = \frac{1}{2\pi}\,\frac{\Gamma_s}{(\frac{\Gamma_s}{2})^2 + (E_\alpha - \bar{E}_k)^2}, \tag{D.10}$$

for

$$\Gamma_s = 2\pi\frac{v^2}{D}. \tag{D.11}$$

Appendix E

Young Diagrams

The eigenfunctions $|\alpha\rangle$ of H can be classified according to the irreducible representations of the group of permutations under which they transform among themselves. The various symmetries (symmetric, antisymmetric, or mixed) may be characterized by Young Diagrams or tableaux.

Young Diagrams are composed of k rows of squares of length f_i. The restrictions are as follows:

$$f_1 \leq f_2 \leq f_3 \leq \ldots f_k \quad \sum_{i=1}^{k} f_i = n = number\ of\ particles \tag{E.1}$$

with a notation of $[f_1 f_2 f_3 \ldots f_k]$ or $[f]$. An example of a Young diagram is shown in figure E.1. Each square is associated with a nucleon. For any $|\alpha\rangle$, the symmetry is obtained by symmetrizing with respect to the nucleons numbers in the same row. The resulting function is then antisymmetrizing with respect to the nucleons whose numbers appear in the same column.

Fully symmetric states are characterized by $f_1 = n$ and $f_2 = f_3 = \ldots = f_k = 0$, or one row of length n, denoted by $[n]$. Fully antisymmetric states are characterized by $f_1 = f_2 = f_3 = \ldots = f_n = 1$ and $f_{n+1} = \ldots = f_k = 0$, or n rows of length 1, denoted by $[111\ldots1]$.

The number of "standard" arrangements is determined by the number of independent functions of a symmetry type for a given Young diagram. A "standard" arrangement has its nucleon numbers increasing from left to right in each row and from top to bottom in each column (see fig. E.2). Each "standard" arrangement of a Young diagram has a "standard" arrangement of the dual diagram when rows and columns are switched.

Spin and isospin wavefunctions are multiplied by spatial wavefunctions to form states which are fully antisymmetric. In other words, the spin-isospin functions determine the symmetry of the spatial function. Spin and isospin states of a single nucleon can be characterized by (m_t, m_s) which provides four possible states for each

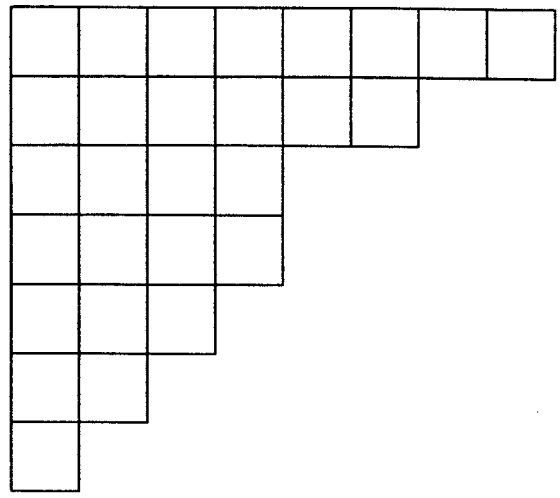

Figure E.1: A Young diagram.

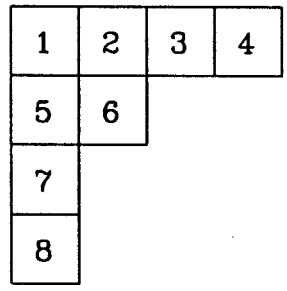

Figure E.2: A Young diagram for $A_v = 8$.

nucleon. Since the Young diagrams characterize the symmetry, they cannot have columns which contain more than 4 squares. Some of the diagrams yield zero when the spin-isospin functions are antisymmetrized. The allowed diagrams have four rows which have the restrictions

$$f_1 \geq f_2 \geq f_3 \geq \cdots f_4 \quad \sum_{i=1}^{4} f_i = n \tag{E.2}$$

where n is equal to A_v.

The group transformations $U(4)$ have irreducible representations associated with this set of Young diagrams.$SU(4)$ is a subgroup of $U(4)$ whose matricies have determinants equal to unity. The $SU(4)$ generators

$$\begin{array}{lll} \langle m_t m_s| & \sigma_i & |m_t m_s'\rangle \\ \langle m_t m_s| & \tau_i & |m_t' m_s\rangle \\ \langle m_t m_s| & \tau_i\,\sigma_j & |m_t' m_s'\rangle \end{array} \tag{E.3}$$

lead to the quantum numbers P, P', and P" of chapter 5. These three numbers uniquely determine the irreducible representations of $SU(4)$.

Bibliography

[1] B.A.Brown and B.H.Wildenthal, Ann. Rev. Nucl. Part. Sci. **38**, 29 (1988).

[2] B.A.Brown *et al.*, *OXBASH code*, MSUNSCL Report **524** (1988).

[3] E. Wigner, Phys. Rev. **51**, 106, 947 (1937).

[4] A.Bohr and B.Mottelson, *Nuclear Structure*. Vol. 1 (Benjamin, New York, 1969).

[5] B. A. Brown, Nucl. Phys. **A577**, 13c (1994).

[6] C. E. Rolfs and W. S. Rodney, *Cauldrons in the Cosmos* (The University of Chicago Press, 1988).

[7] D. J. Dean, S. E. Koonin, K. Langanke, and Y. Alhassid, Phys. Rev. Lett. **74**, 2909 (1995).

[8] G.F.Bertsch, P.F.Bortignon and R.A.Broglia, Rev. Mod. Phys. **55**, 287 (1985).

[9] G.Kilgus *et al.*, Z. Phys. **A326**, 41 (1987)

[10] E.P.Wigner, Ann. Math. **62**, 548 (1955).

[11] M.Feingold, A.Gioletta, F.M.Izrailev and L.Molinari, Phys. Rev. Lett. **70**, 2939 (1993).

[12] C.A.Bertulani and V.G.Zelevinsky, Phys. Rev. Lett. **71**, 967 (1993); Nucl. Phys. **A568**, 931 (1994).

[13] C.H.Lewenkopf and V.G.Zelevinsky, Nucl. Phys. **A569**, 183 (1994).

[14] S.Mordechai *et al.*, Phys. Rev. **C41**, 202 (1990); J.Ritman *et al.*, Phys. Rev. Lett. **70**, 533 (1993); R.Schmidt *et al.*, Phys. Rev. Lett. **70**, 1767 (1993); T.Aumann *et al.*, Phys. Rev. **C47**, 1728 (1993).

[15] C.H.Lewenkopf and V.G.Zelevinsky, Nucl. Phys. **A569**, 183 (1994).

[16] B.Lauritzen, P.F.Bortignon, R.A.Broglia and V.Zelevinsky, Phys. Rev. Lett. **74**, 5190 (1995).

[17] S.S.M.Wong, *Introductory Nuclear Physics* (Prentice-Hall,Inc., 1990).

[18] I.S.Towner, Phys. Reports, **155**, 5 (1987).

[19] B.A.Brown and G.Bertsch, Phys. Lett. **148B**, 5 (1984).

[20] S.Åberg, Prog. Part. Nucl. Phys. **28**, 11 (1992).

[21] V. Zelevinsky, B. A. Brown, N. Frazier and M Horoi, Phys. Reports, **276**, 85 (1996).

[22] B.A.Brown, W.A.Richter, R.E. Julies, and B.H.Wildenthal, Annals of Physics, **182**, 191-236 (1988).

[23] T.A.Brody, J.Flores, J.B.French, P.A.Mello, A.Pandey and S.S.M.Wong, Rev. Mod. Phys. **53**, 385 (1981).

[24] V.V.Flambaum, G.F.Gribakin and F.M.Izrailev, Phys. Rev. **E53**, 5729 (1996).

[25] V.G.Zelevinsky, P.F.Bortignon and R.A.Broglia, Preprint NBI-93-45.

[26] O.P.Sushkov and V.V.Flambaum, Pis'ma Zh. Exptl. Teor. Fiz. **32**, 377 (1980) [JETP Lett. **32**, 353 (1980)]; Usp. Fiz. Nauk **136**, 3 (1982) [Sov. Phys. Usp. **25**, 1 (1982)].

[27] V.G.Zelevinsky, Nucl. Phys. **A553**, 125c (1993); **A570**, 411c (1994).

[28] A.Bracco *et al.*, Phys. Rev. Lett. **62**, 2080 (1989); G.Enders *et al.*, Phys. Rev. Lett. **69**, 249 (1992); J.J.Gaardhøje, Ann. Rev. Nucl. Part. Sci. **42**, 483 (1992).

[29] A.Bracco *et al.*, Phys. Rev. Lett. **74**, 3748 (1995).

[30] H.L.Harney, A.Richter and H.A.Weidenmüller, Rev. Mod. Phys. **58**, 607 (1986).

[31] V.G.Zelevinsky and P. von Brentano, Nucl. Phys. **A529**, 141 (1991).

[32] J.Zakrzewski and D.Delande, Phys. Rev. **E47**, 1650 (1993).

[33] K.K.Mon and J.B.French, Ann. Phys. **95**, 90 (1975).

[34] I.C.Percival, J. Phys. **B6**, L229 (1973).

[35] M. Horoi, V. Zelevinsky and B. A. Brown, Phys. Rev. Lett. **74**, 5194 (1995).

[36] V.V.Flambaum, A.A.Gribakina, G.F.Gribakin and M.G.Kozlov, Phys. Rev. **A50**, 267 (1994).

[37] F.M.Izrailev, Phys. Rep. **196**, 299 (1990).

[38] I.M.Lifshits, S.A.Gredescul and L.A.Pastur, *Introduction to the Theory of Disordered Systems*, John Wiley and Sons, Inc., 1988.

[39] P.M.Endt, Atomic Data and Nuclear Data Tables, **19**, 23-61, (1977).

[40] B.A.Brown, A.Csótó, and R.Sherr, Nucl. Phys. **A597**, 66 (1996).

[41] N. Frazier, B. A. Brown and V. Zelevinsky, Phys. Rev. **C54**, 1665 (1996).

[42] J. B. French and K. F. Ratcliff, Phys. Rev. **C3**, 94 (1971).

[43] V. Zelevinsky, Ann. Rev. Nucl. Part. Sci., **46**, 237 (1996).

[44] K. T. Hecht and S. C. Pang, J. Math. Phys. **10**, 1571 (1969).

[45] I. Talmi, *Simple Models of Complex Nuclei: The Shell Model and Interacting Boson Model*, (Harwood Academic publishers, USA 1993).

[46] J.Reiter and H.L.Harney, Z.Phys. **A337**, 121 (1990).

[47] V.Zelevinsky, M.Horoi and B.A.Brown, Phys. Lett. **B350**, 141 (1995).

[48] O.Bohigas and H.A.Weidenmüller, Ann. Rev. Nucl. Part. Sci. **38**, 421 (1988).

[49] P.M.Gopych *et al.*, Sov. J. Part. Nuclei **19**, 338 (1988).

[50] W.E.Ormand and R.A.Broglia, Phys. Rev. **C46**, 1710 (1992).

[51] F.Haake, *Quantum Signatures of Chaos* (Springer, New York, 1991).

[52] S.Drożdż, S.Nishizaki, J.Speth and J.Wambach, Phys. Rev. **C49**, 867 (1994).

[53] V.G.Zelevinsky, Nucl. Phys. **A555**, 109 (1993).

[54] B. A. Brown and K. Rykaczewski, Phys. Rev. **C50**, R2270 (1994).

[55] W. Bauer, D. McGrew, V. Zelevinsky and P. Schuck, Phys. Rev. Lett. **72**, 3771 (1994); Nucl. Phys. **A583**, 93 (1995).

[56] J.J.M.Verbaarschot and P.J.Brussard, Phys. Lett. **87B**, 155 (1979).

[57] F.S.Chang and J.B.French, Phys. Lett. **44B**, 131 (1973).

[58] J.P.Draayer, J.B.French and S.S.M.Wong, Ann. Phys. **106**, 472, 503 (1977).

[59] V. Zelevinsky, private communication.

[60] J.D.Millener, private communication.